

# **Phase Kinetics and Mechanical Characteristics of Sn Anodes in Li-ion Batteries**

**Chun-Hao Chen**

Master of Science, Brown University, 2014

Bachelor of Science, National Tsing Hua University, 2010

A dissertation submitted to the School of Engineering in partial fulfillment of  
the requirements for the degree of Doctor of Philosophy

Brown University  
Providence, Rhode Island

May 2018

© Copyright 2018 by Chun-Hao Chen

This dissertation by Chun-Hao Chen is accepted in its present form  
by the School of Engineering as satisfying  
the dissertation requirement for the degree of Doctor of Philosophy

Date \_\_\_\_\_

\_\_\_\_\_  
Professor Eric Chason,  
Advisor

Recommended to the Graduate Council

Date \_\_\_\_\_

\_\_\_\_\_  
Professor Pradeep R. Guduru,  
Reader

Date \_\_\_\_\_

\_\_\_\_\_  
Professor Allan F. Bower,  
Reader

Approved by the Graduate Council

Date \_\_\_\_\_

\_\_\_\_\_  
Professor Andrew G. Campbell,  
Dean of Graduate School

# Curriculum Vitae

Chun-Hao Chen received his Bachelor of Science degree in Materials Science Engineering at National Tsing Hua University in Taiwan in June 2010. In September 2011, he started pursuing his graduate study in Materials Science at the School of Engineering at Brown University. He served as a teaching assistant of the undergraduate course Introduction of Materials Science in the fall semesters of 2013 and 2014. In May 2014, he received his Master of Science degree in Engineering, and continued his graduate study as a Ph.D. candidate in Materials Science at the School of Engineering. His research was focused on the kinetics of phase transformation and the correlated mechanical characteristics of Sn electrodes as the anode material in Li-ion batteries.

# Acknowledgments

It is said that talents are everywhere, however seldom can they be recognized. I am deeply grateful to have the opportunity to work with Professor Eric Chason and Professor Pradeep R. Guduru. I sincerely appreciate their guidance, support, and mentorship throughout my graduate studies. This experience has sharpened my thinking and strengthen me mentally. I am also thankful to Professor Allan F. Bower for his assistance and inspiring discussion that helped me in bridging the experimental observations with theories.

I would like to acknowledge Professor Siva Nadimpalli, Professor Vijay Sethuraman, Dr. Michael Chon, Dr. Nitin Jadhav, and Dr. Fei Pei who assisted me at many levels at the early stages of my research. Without their help, my research would not been smooth and fruitful.

I want to thank all my friends and colleagues at Brown University and in Providence. Many thanks to Steven Ahn, Alison Engwall, Jonathan Estrada, Daniel Gerbig, Nupur Jain, Benjamin Johnson, Ravi Kumar, Leah Nation, Jay Sheth, Zhaoxia Rao, Shaghayegh Rezazadeh, Vineeth Venugopal, Kaushik Vijaykumar, Insun Yoon and other friends in Professor Chason's lab and Professor Guduru's lab for their company and help. They made this journey very unique and colorful, and made me feel that Providence is my second home.

Last but not least, I would like to thank my family for their love and encouragement that helped me overcome many difficulties during my graduate studies and for supporting me along the way.

# Table of Contents

<b>Chapter 1</b>	<b>Introduction</b>	<b>1</b>
1.1	A brief review of Sn Anodes in Li-ion batteries.....	2
1.1.1	Electrochemical characteristics.....	2
1.1.2	Mechanical degradation.....	4
1.1.3	Experimental and theoretical characterization.....	4
1.2	Overview of the thesis.....	6
	References.....	7
<b>Chapter 2</b>	<b>Experimental</b>	<b>10</b>
2.1	Sn thin film sample preparation.....	10
2.1.1	Physical vapor deposition of Ti and Cu layers.....	11
2.1.2	Electrodeposition of Sn layer.....	11
2.2	Electrochemical and <i>in situ</i> stress measurements.....	13
2.2.1	Configuration of electrochemical cell.....	14
2.2.2	Multi-beam optical stress sensor.....	15
2.3	X-ray diffraction.....	17
	References.....	19
<b>Chapter 3</b>	<b>Phase and Stress Evolution during Initial Lithiation</b>	<b>20</b>
3.1	Experimental condition.....	21
3.1.1	Sample description.....	21
3.1.2	Electrochemical experiment.....	21
3.1.3	<i>In situ</i> stress measurement.....	24
3.1.4	Focused-ion beam and X-ray diffraction analysis.....	25
3.2	Results and discussion.....	27
3.2.1	Observation in electrochemical and stress and measurements.....	27
3.2.2	Determination of stress in the solid electrolyte interphase, Sn, and $\text{Li}_2\text{Sn}_5$ layers.....	30
3.2.3	Linear kinetic model – the steady-state phase transformation.....	34
3.3	Conclusions.....	41
	References.....	42

**Chapter 4 Numerical solution of a Single Moving Boundary and Diffusion-induced Stress** 44

---

4.1	Kinetic model of the nucleation stage.....	46
4.1.1	Characteristic in the current density during nucleation.....	46
4.1.2	Demonstration of nucleation period.....	46
4.1.3	Analytical solution of Li concentration during nucleation.....	48
4.2	Kinetic model of a single moving phase boundary.....	51
4.2.1	Governing equations.....	52
4.2.2	Boundary conditions.....	53
4.3	Finite-difference analysis.....	56
4.3.1	General finite-difference formulae.....	56
4.3.2	Lagrangian interpolation.....	58
4.3.3	Calculation procedure.....	61
4.3.4	Validation of the finite-difference modeling.....	66
4.3.5	Calibration with experiments.....	69
4.4	Mechanisms of diffusion-induced stress.....	75
4.4.1	Rate-dependent plasticity.....	75
4.4.2	Elastic unloading.....	80
4.4.3	Correlation between Li concentration evolution and diffusion-induced stress ...	81
4.4.4	Calculation of stress evolution observed in experiments.....	82
4.5	Conclusions.....	86
	References.....	87

**Chapter 5 Measurement and Numerical Solution of Two Moving Boundaries** 88

---

5.1	Experimental condition.....	89
5.1.1	Sample description.....	89
5.1.2	Electrochemical experiment.....	89
5.1.3	<i>In situ</i> stress measurement.....	92
5.1.4	Focused-ion beam and X-ray diffraction analysis.....	93
5.2	Observation in electrochemical and stress measurements.....	95
5.2.1	Experiment [i]: the growth of $\text{Li}_2\text{Sn}_5$ and LiSn phases with a pre-grown $\text{Li}_2\text{Sn}_5$ layer.....	95
5.2.2	Experiment [ii]: the simultaneous growth of $\text{Li}_2\text{Sn}_5$ and LiSn phases.....	96
5.2.3	Experiment [iii]: the estimation of surface Li concentration in LiSn phase.....	97

5.3	Kinetic Model of Two Moving Boundaries.....	98
5.3.1	Initial condition.....	98
5.3.2	Modeling configuration: governing equations and boundary conditions.....	103
5.3.3	Finite-difference analysis.....	108
5.3.4	Demonstration of the two phase boundaries progression.....	117
5.4	Calibration with experiments of two moving boundaries.....	121
5.4.1	Experiment [i]: the growth of $\text{Li}_2\text{Sn}_5$ and $\text{LiSn}$ phases with a pre-grown $\text{Li}_2\text{Sn}_5$ layer.....	123
5.4.2	Experiment [ii]: the simultaneous growth of $\text{Li}_2\text{Sn}_5$ and $\text{LiSn}$ phases.....	133
5.5	Conclusions.....	139
	References.....	140
<b>Chapter 6 Elastic Modulus Measurement of Li-Sn Phases</b>		<b>141</b>
6.1	Experimental condition.....	141
6.1.1	Sample description.....	141
6.1.2	Electrochemical experiment.....	143
6.1.3	<i>In situ</i> stress measurement.....	145
6.1.4	Biaxial modulus calculation.....	148
6.1.5	X-ray diffraction of Li-Sn phases.....	150
6.2	Results and discussion.....	152
6.2.1	X-ray diffraction of Li-Sn phases.....	152
6.2.2	Stress during phase transformations.....	154
6.2.3	Biaxial modulus measurement.....	156
6.2.4	Yield stress of Sn film anodes.....	159
6.3	Conclusions.....	160
	References.....	160
<b>Chapter 7 Summary</b>		<b>162</b>
7.1	Conclusions.....	162
7.2	Future works.....	164
	References.....	165

# List of Tables

<b>Table 1.1.</b>	Material properties of the Li-Sn phases	3
<b>Table 2.1.</b>	Recipe for preparing one liter of Solderon SC Tin electroplating solution	12
<b>Table 3.1.</b>	Experimental condition of Experiment [i]: the growth of $\text{Li}_2\text{Sn}_5$ phase	21
<b>Table 3.2.</b>	Experiment condition of Experiment [iii]: the estimation of surface Li concentration in $\text{Li}_2\text{Sn}_5$ phase	23
<b>Table 3.3.</b>	Coupled parameters obtained from fitting Eq. (3.8) to the experimental data	39
<b>Table 3.4.</b>	Evaluation of kinetic parameters by using $C_s$ value in Fig. 3.7	40
<b>Table 4.1.</b>	Parameters used in the demonstration in Fig. 4.9	68
<b>Table 4.2.</b>	Parameters used in the calculation for comparison with experiments	70
<b>Table 4.3.</b>	Material parameters obtained by the current density fitting in Fig. 4.1a	71
<b>Table 4.4.</b>	Parameters used in the stress calculation	83
<b>Table 4.5.</b>	Material parameters obtained by the stress-thickness fitting in Fig. 4.1b	85
<b>Table 5.1.</b>	Experimental condition of Experiment [i]: the growth of $\text{Li}_2\text{Sn}_5$ and LiSn phases with a pre-grown $\text{Li}_2\text{Sn}_5$ layer	90
<b>Table 5.2.</b>	Experimental condition of Experiment [ii]: the simultaneous growth of $\text{Li}_2\text{Sn}_5$ and LiSn phases	91
<b>Table 5.3.</b>	Experimental condition of Experiment [iii]: the estimation of surface Li concentration in LiSn phase	92
<b>Table 5.4.</b>	Parameters used in the demonstration in Figs. 5.10 and 5.11	119
<b>Table 5.5.</b>	Parameters used in the calculation for comparison with experiments	122
<b>Table 5.6.</b>	Parameters used in the calculation in Figs. 5.12 and 5.13: the lithiation at 0.65 V in Experiment [i]	123

<b>Table 5.7.</b>	Material parameters obtained by numerical analysis of Experiment [i]	124
<b>Table 5.8.</b>	Parameters used in the calculation in Fig. 5.14: the lithiation at 0.5 V in Experiment [i]	128
<b>Table 5.9.</b>	Parameters used in the calculation with Eqs. (5.40) and (5.41) for the Experiment [i]	133
<b>Table 5.10.</b>	Parameters used in the calculation of Experiment [ii] in Figs. 5.18 and 5.19	134
<b>Table 5.11.</b>	Material parameters obtained by numerical analysis of Experiment [ii]	134
<b>Table 5.12.</b>	Parameters used in the calculation with Eqs. (5.40) and (5.41) for Experiment [ii]	139
<b>Table 6.1.</b>	Experimental condition of the elastic modulus measurement	144
<b>Table 6.2.</b>	List of samples in the elastic modulus measurement	144
<b>Table 6.3.</b>	Material parameters of the Li-Sn phases	148

# List of Figures

<b>Figure 1.1.</b>	Typical potential profile observed during the galvanostatic cycling of Sn anodes. The potential plateaus correspond to the Li-Sn phase transformations.	3
<b>Figure 2.1.</b>	Configuration of Sn thin film samples.	10
<b>Figure 2.2.</b>	Cross-section image of an as-prepared 1.85 $\mu\text{m}$ polycrystalline Sn sample. The dash line indicates the film surface.	13
<b>Figure 2.3.</b>	Electrochemical half cell and the Multi-Beam Optical Stress Sensor (MOSS) setup.	14
<b>Figure 2.4.</b>	XRD results of: (a) as-prepared 1.85 $\mu\text{m}$ Sn sample, (b) as-prepared 1.85 $\mu\text{m}$ Sn sample covered by the 0.0254 mm thick Kapton film.	17
<b>Figure 2.5.</b>	Customized coin cell casing for the XRD measurement with air-sensitive materials; from left to right: a stainless steel top case with the 0.0254 mm thick Kapton window, a rubber gasket, a stainless steel spacer, a stainless steel spring, and a stainless steel bottom case.	18
<b>Figure 2.6.</b>	XRD results of: (a) as-prepared 500 nm Sn sample, (b) empty customized coin cell casing with the 0.0254 mm thick Kapton window, (c) as-prepared 500 nm Sn sample assembled in the customized coin cell casing.	19
<b>Figure 3.1.</b>	Cross section images of: (a) as-prepared Sn film sample (surface indicated by dashed line), (b) sample lithiated at 0.665 V, showing the Sn/ $\text{Li}_2\text{Sn}_5$ phase boundary (dotted line).	26
<b>Figure 3.2.</b>	XRD results of: (a) as-prepared Sn sample, (b) lithiated Sn sample after potentiostatic lithiation at 0.665 V for 120 hours, showing presence of both Sn and $\text{Li}_2\text{Sn}_5$ phases Both samples were covered by the 0.0254 mm thick Kapton film.	26
<b>Figure 3.3.</b>	Time evolution of: (a) current density and (b) stress-thickness during growth of SEI at 0.8 V for 20 hours followed by potentiostatic lithiation at 0.665 V for 120 hours. The inset in (a) corresponds to the period after the start of lithiation. The dashed line in (b) is the result of fitting to the steady-state model described in text.	28
<b>Figure 3.4.</b>	Value of saturated stress-thickness for samples with different initial Sn thickness during the 20-hour growth of SEI at 0.8 V.	30

<b>Figure 3.5.</b>	Measured stress-thickness vs. $\text{Li}_2\text{Sn}_5$ thickness for lithiation at 0.665 V. Dashed line is used to estimate the slope in the steady-state regime.	32
<b>Figure 3.6.</b>	Schematic plot of the steady-state model for the kinetics of interface motion.	34
<b>Figure 3.7.</b>	Inverse current density ( $1/j$ ) vs. $\text{Li}_2\text{Sn}_5$ thickness for potentiostatic lithiation at 0.665 V, 0.65 V and 0.64 V.	38
<b>Figure 3.8.</b>	Surface Li concentration $C_S$ in the $\text{Li}_2\text{Sn}_5$ phase at different applied potentials.	40
<b>Figure 4.1.</b>	Measurements and calculation (dashed lines) during the potentiostatic lithiation experiments at 0.65 V. (a) current-density and inset showing the nucleation time; (b) stress-thickness and inset showing the transient high stress state.	44
<b>Figure 4.2.</b>	Experimental results underlying estimate of nucleation time of Sn- $\text{Li}_2\text{Sn}_5$ phase transformation.	47
<b>Figure 4.3.</b>	Schematic plot for initial nucleation stage of the numerical solutions.	49
<b>Figure 4.4.</b>	Calculated Li concentration for the initial profile of numerical simulations.	51
<b>Figure 4.5.</b>	Schematic plot of the kinetic model of a single moving boundary.	52
<b>Figure 4.6.</b>	Stencil plot of finite-difference method utilized in the calculation.	57
<b>Figure 4.7.</b>	Schematic plot of the Lagrangian interpolation method near the phase boundary.	59
<b>Figure 4.8.</b>	Schematic plot of the finite-difference framework with a single moving boundary.	61
<b>Figure 4.9.</b>	Comparison of the analytical solution for the semi-infinite diffusion-controlled case and numerical solution for a 9.25 $\mu\text{m}$ film with different values of normalized reaction rate coefficient $\kappa$ .	68
<b>Figure 4.10.</b>	The calculated evolution of the Li concentration profile during the potentiostatic lithiation at 0.65 V.	71
<b>Figure 4.11.</b>	The calculated evolution of Li concentration profile near the Sn/ $\text{Li}_2\text{Sn}_5$ phase boundary: (a) in the $\text{Li}_2\text{Sn}_5$ phase, (b) in the Sn phase.	72

- Figure 4.12.** Comparison of the calculated thickness  $\text{Li}_2\text{Sn}_5$  phase and the estimation from the charge data. The arrow indicates the starting thickness of  $\text{Li}_2\text{Sn}_5$  in finite-difference calculation. 73
- Figure 4.13.** Demonstration of the correlation between rate-dependent stress and the material parameters. (a) normalized rate of concentration change  $\frac{\dot{c}}{\dot{c}_{max}}$ ; (b) and (c): trends of the normalized rate-dependent stress  $\frac{\sigma}{\sigma_0}$  with parameters  $m$  and  $\frac{\eta}{\varepsilon_0} \omega \dot{c}_{max}$ , respectively. 78
- Figure 4.14.** Schematic plots of: (a) Li concentration profiles at time  $t$  and  $t-1$  showing the flux-reversal boundary induced by the phase boundary propagation; (b) the stress distribution at time  $t$  corresponding to the evolution in (a) and the preceding stress distribution at time  $t-1$ . 81
- Figure 4.15.** The calculated evolution of stress distribution in the Sn anode during the potentiostatic lithiation at 0.65 V. 84
- Figure 5.1.** Cross-section images of lithiated samples in: (a) Experiment [i] showing a two layer structure with the  $\text{Li}_2\text{Sn}_5/\text{LiSn}$  phase boundary, (b) Experiment [ii] showing a three layer structure with the Sn/ $\text{Li}_2\text{Sn}_5$  and  $\text{Li}_2\text{Sn}_5/\text{LiSn}$  phase boundaries. The surface is indicated by a dash line and the phase boundaries are by dotted lines. 94
- Figure 5.2.** XRD results of lithiated samples in: (a) Experiment [i] identifying the existence of  $\text{Li}_2\text{Sn}_5$  and LiSn phases, (b) Experiment [ii] identifying the existence of Sn,  $\text{Li}_2\text{Sn}_5$  and LiSn phases. 94
- Figure 5.3.** Measurements and calculation (dash lines) of the Experiment [i], in which the potential held at 0.8 V, 0.65 V and 0.5 V sequentially: (a) current density and two insets showing the nucleation of  $\text{Li}_2\text{Sn}_5$  and LiSn phases respectively, (b) stress-thickness. 96
- Figure 5.4.** Measurements and calculation (dash lines) of the Experiment [ii], in which the potential held at 0.8 V and 0.5 V: (a) current density and inset showing the nucleation of  $\text{Li}_2\text{Sn}_5$  and LiSn phases, (b) the corresponding stress-thickness showing a transient high stress. 97
- Figure 5.5.** Surface Li concentration  $C_S$  in the LiSn phase at different applied potentials. 98
- Figure 5.6.** Schematic plot of initial concentration profile for Experiment [ii], in which both  $\text{Li}_2\text{Sn}_5$  and LiSn phases simultaneously grow from the anode surface. 99

<b>Figure 5.7.</b>	Schematic plots of concentration profile for the Experiment [i]: (a) the initial condition of lithiation at 0.65 V, (b) the resulting concentration at the end of lithiation at 0.65 V, (c) the initial condition of the subsequent lithiation at 0.5 V. The dash lines indicate the redefinition of interfaces induced by the nucleation of the $\gamma$ phase at the surface.	101
<b>Figure 5.8.</b>	Schematic plot of the kinetic model of two moving boundaries.	103
<b>Figure 5.9.</b>	Schematic plot of the finite-difference framework with two moving boundaries.	108
<b>Figure 5.10.</b>	Comparison of the phase propagation in the film consisting of a pre-grown $\beta$ layer with different values of normalized reaction rate coefficients $\kappa_1$ and $\kappa_2$ .	119
<b>Figure 5.11.</b>	Comparison of the phase propagation that both $\beta$ and $\gamma$ phases initiate from the film surface with different values of normalized reaction rate coefficients $\kappa_1$ and $\kappa_2$ .	120
<b>Figure 5.12.</b>	The calculated evolution of the Li concentration profile during the potentiostatic lithiation at 0.65 V in the Experiment [i].	124
<b>Figure 5.13.</b>	The calculated evolution of stress distribution in the anode during the potentiostatic lithiation at 0.65 V in the Experiment [i].	126
<b>Figure 5.14.</b>	The calculated evolution of the Li concentration profile during the potentiostatic lithiation at 0.5 V in the Experiment [i].	128
<b>Figure 5.15.</b>	The propagation of phase boundaries during the potential hold at 0.65 V and 0.5 V in the Experiment [i] obtained by the numerical analysis. The electrolyte/anode interface is located at $x = 0$ .	130
<b>Figure 5.16.</b>	The propagation of phase boundaries at 0.65 V and 0.5 V in Experiment [i] obtained by the numerical analysis. The anode/substrate interface is located at $x = 0$ .	131
<b>Figure 5.17.</b>	The propagation of phase boundaries during lithiation at 0.65 V and 0.5 V in Experiment [i] obtained from the balance of the measured stress-thickness and coulombic charge. The anode/substrate interface is located at $x = 0$ .	132
<b>Figure 5.18.</b>	The calculated evolution of the Li concentration profile during the potentiostatic lithiation at 0.5 V in Experiment [ii].	135

- Figure 5.19.** The propagation of phase boundaries during lithiation at 0.5 V in the Experiment [ii] obtained by numerical analysis. The electrolyte/anode interface is located at  $x = 0$ . 135
- Figure 5.20.** The calculated evolution of stress distribution in the anode during the potentiostatic lithiation at 0.5 V in Experiment [ii]. 137
- Figure 5.21.** The propagation of phase boundaries during the potential hold at 0.5 V in Experiment [ii] obtained by the numerical analysis. The anode/substrate interface is at  $x = 0$ . 138
- Figure 5.22.** The propagation of phase boundaries during lithiation at 0.5 V in the Experiment [ii] obtained from the balance of the measured stress-thickness and coulombic charge. The anode/substrate interface is located at  $x = 0$ . 138
- Figure 6.1.** SEM image of as prepared 500 nm thick Sn film sample showing the grain size distribution between 500 nm and 1.5  $\mu\text{m}$ . 142
- Figure 6.2.** Thickness evolution by using the theoretical densities of Li-Sn phases. The triangular points are the observed thickness in cross-section images in Fig. 6.3. The thicknesses are normalized with respect to the original Sn thickness  $h_f^0 = 500$  nm. 146
- Figure 6.3.** The cross-section images of the 500 nm Sn and lithiated Sn samples at different states of charge. The thickness values are also present in Fig. 6.2. The surface is marked by a dash line. 146
- Figure 6.4.** XRD results of Sn and lithiated Sn samples in Table 6.2: (a) As-prepared 500 nm Sn, (b) Sample 1 ( $\text{Li}_{0.5}\text{Sn}$ ), (c) Sample 2 ( $\text{Li}_{1.1}\text{Sn}$ ), (d) Sample 3 ( $\text{Li}_{2.4}\text{Sn}$ ), (e) Sample 4 ( $\text{Li}_{3.4}\text{Sn}$ ), (f) Sample 5 ( $\text{Li}_{3.7}\text{Sn}$ ). The influences of Kapton and stainless steel casing are also observed. 151
- Figure 6.5.** Experimental data of sample 2 lithiated at 0.5 V during stage (i) of the experiment: phase transformations of Li-Sn phases: (a) potential, (b) current density, (c) capacity, (d) stress-thickness, (e) thickness-averaged stress. 154
- Figure 6.6.** Experimental data of sample 2 during the stage (ii) of experiment: small scale delithiation/lithiation. (a) current density, (b) stress measurement showing the elastic response of the lithiated sample. 156
- Figure 6.7.** The biaxial modulus of lithiated Sn samples at different states of charge. 157

**Figure 6.8.** The comparison of the bulk moduli obtained in this work and the values reported in the literature using DFT calculations. 158

**Figure 6.9.** The stress in the lithiated samples at different states of charge obtained at the end of state (i) of electrochemical experiment 159

# Chapter 1.

## Introduction

---

With an increasing demand of energy storage solutions for portable electronic devices and electrical vehicles, rechargeable Li-ion batteries have become a preferred choice. Li-ion batteries offer higher energy density, lower self-discharge, flexible design, and comparable cost per cycle life than other rechargeable battery technologies.<sup>1-3</sup> Li is the most electropositive element and the lightest metal; therefore, the energy density of Li-ion batteries is high, typically twice more than nickel-based (e.g., nickel-cadmium and nickel-metal-hydride) batteries and four times that of lead-acid batteries.<sup>1, 2</sup> The self-discharge of Li-ion batteries is significantly less than other types of batteries, making it suitable for modern fuel usages.<sup>2</sup> Thin-film technology is usually employed in the commercial manufacture of Li-ion batteries as it offers design flexibility in shape and size for versatile applications.<sup>1</sup> It can also benefit from scaling up of the manufacture, although the initial cost of Li-ion batteries is higher, the total lifecycle cost is comparable to the lead-acid batteries.<sup>3</sup>

To date, a general commercial Li-ion battery has lithium transition metal oxides (e.g.,  $\text{LiCoO}_2$ ) as the positive electrode (i.e., cathode) and graphite as the negative electrode (i.e., anode). The fully lithiated graphite anode ( $\text{LiC}_6$ ) provides a theoretical specific capacity of 372 mAh/g. As a result of numerous improvements, the reversible capacities of graphite anodes have already reached around 350 mAh/g.<sup>1</sup> Therefore, to increase the

energy density, researchers have been looking for alternative anode materials with higher specific capacities in the hope of providing more proficient Li-ion batteries. One of the material is Sn as it offers a large theoretical specific capacity of 994 mAh/g,<sup>4</sup> which makes Sn a promising anode material for Li-ion batteries.

## **1.1. A Brief review of Sn anodes in Li-ion batteries**

### *1.1.1 Electrochemical characteristics*

During electrochemical cycling, Sn reacts with Li and forms multiple lithiated phases -  $\text{Li}_2\text{Sn}_5$ ,  $\text{LiSn}$ ,  $\text{Li}_7\text{Sn}_3$ ,  $\text{Li}_5\text{Sn}_2$ ,  $\text{Li}_{13}\text{Sn}_5$ ,  $\text{Li}_7\text{Sn}_2$ , and  $\text{Li}_{22}\text{Sn}_5$  - at different values of the applied potential, which makes the Li-Sn reactions more complex than other candidates for anode material (e.g., Si, Ge etc.). Fig. 1.1 shows the typical potential profile during galvanostatic cycling of Sn anodes. The potential plateaus in lithiation relate to the formation of the lithiated phases. Whereas, the plateaus in delithiation correspond to the decomposition of the lithiated phases. According to the Li-Sn binary phase diagram,<sup>5, 6</sup> these lithiated phases are intermetallic line compounds and have well-defined compositions. The theoretical densities<sup>4</sup>, specific capacities and the volumetric strain of the lithiated phases are presented in Table 1.1.

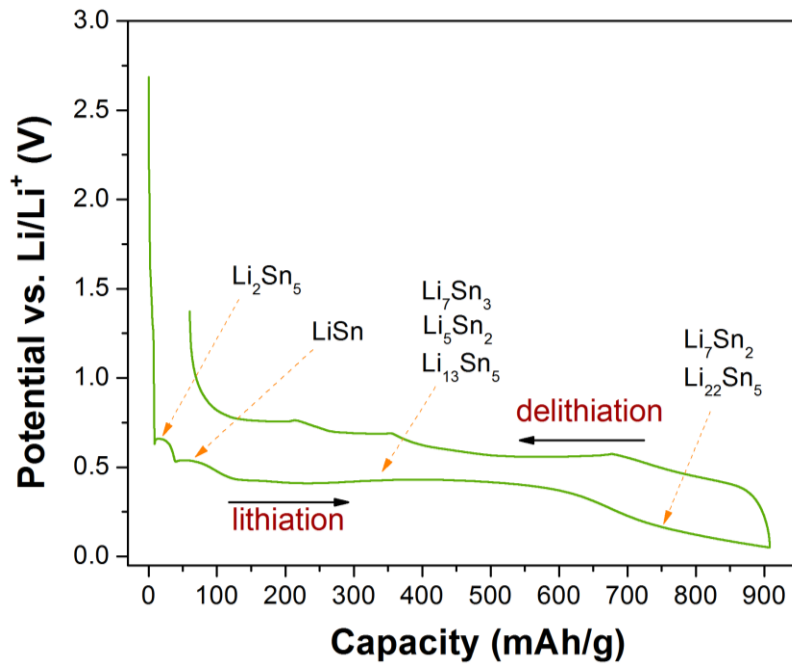


**Figure 1.1.** Typical potential profile observed during the galvanostatic cycling of Sn anodes. The potential plateaus correspond to the Li-Sn phase transformations.

**Table 1.1.** Material properties of the Li-Sn phases

Phase	Density (g/cm <sup>3</sup> )	Theoretical Specific Capacity (mAh/g)*	Volumetric strain with respect to Sn (%)*
Sn	7.29	-	-
Li <sub>2</sub> Sn <sub>5</sub>	6.11	90.3	22.1
LiSn	5.10	225.8	51.3
Li <sub>7</sub> Sn <sub>3</sub>	3.67	526.8	125.7
Li <sub>5</sub> Sn <sub>2</sub>	3.54	564.4	136.0
Li <sub>13</sub> Sn <sub>5</sub>	3.46	586.8	142.7
Li <sub>7</sub> Sn <sub>2</sub>	2.96	790.2	196.7
Li <sub>22</sub> Sn <sub>5</sub>	2.56	993.4	258.0

\*values are calculated with the theoretical densities reported in Ref. 4

### *1.1.2 Mechanical degradation*

Since Sn is a metal with a very dense structure, the reactions with Li lead to large volumetric strain of  $\sim 260\%$  at the maximum capacity as shown in Table 1.1. Such large expansion induces mechanical degradations such as pulverization of the anode and disintegration of the electronic connection between the active materials and the current collector, resulting in dramatic capacity decay and poor cyclability of Sn anodes.<sup>7-11</sup> In order to improve the reliability, many researchers have adopted new fabrication methods, and found that by reducing the dimension of anode (i.e., size of particles or thickness of films), the cyclability of Sn anodes can be slightly improved.<sup>8, 12-17</sup> However, it is also known that smaller particles have more active surface area that may enhance the surface side reactions (e.g., solid electrolyte interphase (SEI) formation) and lead to capacity decrease.<sup>18</sup>

Other investigations have focused on modifying the design of the electrodes to accommodate the volumetric change during electrochemical cycling,<sup>19-22</sup> and reported that reliability of Sn anodes can be improved by different architectural designs. Nevertheless, these findings suggest that a fundamental understanding of the Li-Sn phase transformations is essential for comprehensive application of Sn anodes.

### *1.1.3 Experimental and theoretical characterizations*

Various *in situ* experimental techniques have been employed to study the phase transformations and evolution of micro structure of Sn anodes. The structural changes of Sn anodes during galvanostatic cycling have been investigated by using X-ray diffraction,<sup>23, 24</sup> X-ray transmission microscopy,<sup>25</sup> and 3-D synchrotron X-ray tomography.<sup>26</sup> Transmission electron microscopy has been performed on single-crystal

Sn nano-needles to observe the evolution of polycrystalline Li-Sn phases during phase transformations.<sup>27</sup> The change in morphology of patterned Sn films has been analyzed by Atomic force microscopy.<sup>28</sup> These results indicate that the large volume expansion occurs as the Li-Sn phase transformations take place. Furthermore, multiple phase transformations can happen simultaneously during galvanostatic cycling.

In addition, thermodynamic properties (such as activity and enthalpy) of Sn anodes at high temperatures (350-750 °C) have been studied experimentally by electromotive force measurements<sup>29</sup> and Knudsen Effusion Mass Spectrometry.<sup>30</sup> Neutron depth profiling spectroscopy has been used to characterize Li distribution in Sn anodes during lithiation.<sup>31, 32</sup> Galvanostatic intermittent titration technique has been performed to obtain Li diffusivity in Sn anodes.<sup>33, 34</sup> These measurements provide essential information for the theoretical studies of Sn anodes.

Regarding the mechanical properties of Sn anodes, *in situ* wafer curvature measurements have been used to measure the overall stress evolution during galvanostatic cycling<sup>35</sup> and cyclic voltammetry.<sup>36</sup> These measurements indicate that when the large volumetric expansion occurs during lithiation, it also leads to a large compressive stress. When delithiation takes place, the compressive stress suddenly relaxes and leads to a tensile stress in the Sn anode. Such compressive and tensile stress behavior results in the mechanical failure, causing the fading in capacity. Furthermore, theoretical studies on the elastic moduli of Sn anodes have been studied by density functional theory calculations, which predicted significant softening of Sn anodes as the Li concentration increases.<sup>37-39</sup>

## 1.2. Overview of the thesis

The objective of this thesis is to characterize the kinetics of Li-Sn phase transformations and its correlation with the evolution of stress and mechanical properties via experiments and modeling analysis.

To investigate specific phase transformations and the properties of the corresponding phases, potentiostatic lithiation is utilized to select the desired phase transformations. Simultaneously, the *in situ* curvature measurement is employed to acquire the stress evolution in the Sn thin film anodes. Kinetic and mechanical modeling are performed to analyze the measurements. The general experimental procedure including sample preparation, electrochemical and stress measurements, and ex-situ sample examinations are described in chapter 2.

Chapter 3 discusses the very first phase transformation in Li-Sn system, in which Sn is transformed into  $\text{Li}_2\text{Sn}_5$  phase. The results show that the phase transformation occurs relatively homogeneously from the anode surface during the potentiostatic lithiation. The stress in the surface SEI, Sn, and  $\text{Li}_2\text{Sn}_5$  layers are determined. A steady-state linear kinetic model is used to analyze the kinetic parameters of Li diffusion and phase transformation. In addition, a transient high stress is observed at the beginning of the phase transformation, which is discussed in chapter 4.

In chapter 4, a kinetic model consisting of a single moving boundary is developed to understand the transient stress behavior in chapter 3. The finite-difference calculation is employed to investigate the correlation between the evolution of Li concentration and the observed transient stress. The findings indicate that the behavior is caused by the rate-dependent stress in the Sn layer, while the stress in the forming  $\text{Li}_2\text{Sn}_5$  layer can be approximated at its low strain rate yield stress.

In chapter 5, the electrochemical experiments coupled with *in situ* stress measurements of  $\text{Li}_2\text{Sn}_5$  and  $\text{LiSn}$  phase transformations are discussed. The finite-difference analysis is extended into the case of two moving boundaries, and is utilized to calculate the electrochemical current density and stress evolution in the anodes. The kinetic and mechanical parameters are acquired by comparing the simulations and the experiments. The kinetic modeling demonstrated in chapters 4 and 5 provide an example for a study of multiple phase transformations and it can be adapted to investigate other material systems.

In chapter 6, the evolution of elastic modulus of thin film Li-Sn phases is determined experimentally by characterizing elastic behavior of Sn film samples via delithiation at different Li concentrations.<sup>40</sup> The X-ray diffractions are used to identify the resulting Li-Sn phases in the samples. The findings are consistent with the literature and showing a significant decrease in elastic modulus as the Sn phase transforms into Li-rich phases. The results provide useful information for future theoretical analysis on Sn anodes.

## **References**

1. J.-M. Tarascon and M. Armand, *Nature*, **414** (2001).
2. I. Buchmann, *Batteries in a Portable World: A Handbook on Rechargeable Batteries for Non-Engineers*, Cadex Electronics Inc (2001).
3. J. P. O'Connor, *Off Grid Solar: A handbook for Photovoltaics with Lead-Acid or Lithium-Ion batteries*, CreateSpace Independent Publishing Platform (2016).
4. M. Winter and J. O. Besenhard, *Electrochimica Acta*, **45** 31-50 (1999).
5. W. G. Moffatt, *The Handbook of Binary Phase Diagrams*, Schenectady, N.Y. (1978).
6. F. Yin, X. Su, Z. Li, and J. Wang, *Journal of Alloys and Compounds*, **393** 105-108 (2005).
7. J. P. Maranchi, A. F. Hepp, A. G. Evans, N. T. Nuhfer, and P. N. Kumta, *J. Electrochem. Soc.*, **153** (6), A1246-A1253 (2006).
8. K. Ui, S. Kikuchi, Y. Kadoma, N. Kumagai, and S. Ito, *Journal of Power Sources*, **189** 224-229 (2009).
9. J. Park, S. Rajendran, and H. Kwon, *Journal of Alloys and Compounds*, **159** 1409-1415 (2006).

10. S. D. Beattie, T. Hatchard, A. Bonakdarpour, K. C. Hewitt, and J. R. Dahn, *Journal of The Electrochemical Society*, **150** A701-A705 (2003).
11. H. F. Nara, Yoshiki; Takai, Azusa; Komastu, Masaki; Mukaibo, Hitomi; Yamauchi, Yusuke; Momma, Toshiyuki; Kuroda, Kazuyuki; Osaka, Tetsuya, *Chemistry Letters*, **37** (2), 142-143 (2008).
12. R. Ochs, D. V. Szabo, S. Schlabach, S. Becker, and S. Indris, *Physica Status Solidi A*, **208** (2), 471-473 (2011).
13. N. Li, C. R. Martin, and B. Scrosati, *Journal of Power Sources*, **97-98** 240-243 (2001).
14. W. Choi, J. Y. Lee, B. H. Jung, and H. S. Lim, *Journal of Power Sources*, (136), 154-159 (2004).
15. N. Pereira, L. C. Klein, and G. G. Amatucci, *Solid State Ionics*, (167), 29-40 (2004).
16. N. Li and C. R. Martin, *J. Electrochem. Soc.*, **148** (2), A164-A170 (2001).
17. S. Xun, X. Song, V. Battaglia, and G. Liu, *Journal of The Electrochemical Society*, **160** (6), A849-A855 (2013).
18. P. Verma, P. Maire, and P. Nova'k, *Electrochim Acta*, **55** 6332-6341 (2010).
19. D. H. Nam, R. H. Kim, D. W. Han, and H. Kwon, *Electrochimica Acta*, **66** 126-132 (2012).
20. D. Jiang, H. Tian, C. Qiu, X. Ma, and Y. Fu, *Journal of Solid State Electrochemistry*, **15** 2639-2644 (2011).
21. B. D. Polat, B. Bilici, and O. Keles, *ECS Transaction*, **66** (9), 267-275 (2015).
22. R. Hu, M. Zhu, H. Wang, J. Liu, O. Liuzhang, and J. Zou, *Acta Materialia*, **60** 4695-4703 (2012).
23. K. Rhodes, R. Meisner, M. Kirkham, N. Dudney, and C. Daniel, *Journal of The Electrochemical Society*, **159** (3), A294-A299 (2012).
24. N. Oehl, G. Schmuelling, M. Knipper, R. Kloepsch, T. Placke, J. Kolny-Olesiak, T. Plaggenborg, M. Winter, and J. Paris, *Royal Society of Chemistry*, (2015).
25. S.-C. Chao, Y.-C. Yen, Y.-F. Song, Y.-M. Chen, H.-C. Wu, and N.-L. Wu, *Electrochemistry Communications*, **12** 234-237 (2010).
26. J. Wang, Y.-c. K. Chen-Wiegart, and J. Wang, *Angewandte Chemie*, **53** 4460-4464 (2014).
27. M. T. Janish, D. T. Mackay, Y. Liu, K. L. Jungjoham, C. B. Carter, and M. G. Norton, *J. Mater. Sci.* (2015).
28. L. Y. Beaulieu, S. D. Beattie, T. D. Hatchard, and J. R. Dahn, *Journal of The Electrochemical Society*, **150** (4), A419-A424 (2003).
29. C. J. Wen and R. A. Huggins, *J. Electrochem. Soc.*, **128** (6), 1181-1187 (1981).
30. D. Henriques, V. Motalov, L. Bencze, S. Furtauer, and T. Markus, *Journal of Alloys and Compounds*, **585** 299-306 (2014).
31. D. X. Liu, J. Wang, K. Pan, J. Qiu, M. Canova, L. R. Cao, and A. C. Co, *Angewandte Chemie International Edition*, **53** 9498-9502 (2014).
32. J. Wang, D. X. Liu, M. Canova, R. G. Downing, L. R. Cao, and A. C. Co, *Journal of Radioanalytical and Nuclear Chemistry*, **301** 277-284 (2014).
33. J. Xie, N. Imanishi, A. Hirano, Y. Takeda, O. Yamamoto, X. B. Zhao, and G. S. Cao, *Solid State Ionics*, **181** 1611-1615 (2010).

34. K. I. Pridatko, *Russian Journal of Electrochemistry*, **42** (1), 63-70 (2005).
35. A. Mukhopadhyay, R. Kali, S. Badjate, A. Tokranov, and B. W. Sheldon, *Scripta Materialia*, **92** 47-50 (2014).
36. H. Tavassol, M. W. Cason, R. G. Nuzzo, and A. A. Gewirth, *Advanced Energy Materials*, **5** 1400317 (2015).
37. M. Stournara, P. R. Guduru, and V. Shenoy, *Journal of Power Sources*, **208** 165-169 (2012).
38. J. Moon, K. Cho, and M. Cho, *International Journal of Precision Engineering and Manufacturing*, **13** (7), 1191-1197 (2012).
39. K. Li, H. Xie, J. Liu, Z. Ma, Y. Zhou, and D. Xue, *Phys. Chem. Chem. Phys.*, **15** 17658 (2013).
40. V.A. Sethuraman, M. J. Chon, M. Shimshak, N. Van Winkle, and P. R. Guduru, *Electrochemistry Communications*, **12** 1614-1617 (2010).

# Chapter 2.

## Experimental

---

In this chapter, general experimental methods are described in the order of Sn thin film sample fabrication, electrochemistry and *in situ* stress measurements, and ex-situ examinations. Detailed sample description and experimental method for specific experiments are addressed in the experimental condition section of each chapter.

### 2.1 Sn thin film sample preparation

Sn electrode was fabricated in the form of thin films on wafer substrates. The sample have a multi-layer structure as shown in Fig. 2.1. Ti and Cu layers were deposited on the substrates via physical vapor deposition (PVD). The Ti layer was used to enhance adhesion of Cu film to the substrate. The Cu film served as the conductive layer for subsequent electrodeposition of Sn film.

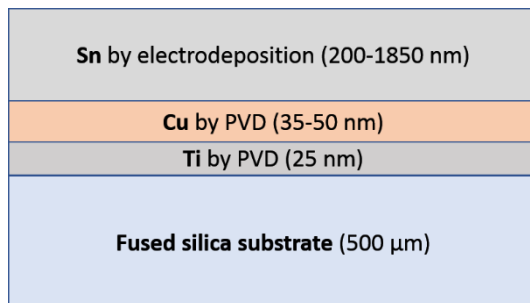


**Figure 2.1.** Configuration of Sn thin film samples.

### *2.1.1 Physical vapor deposition of Ti and Cu layers*

Fused silica quartz wafers (50.8 mm in diameter,  $\sim 500\ \mu\text{m}$  thick, double-side polished) were used as elastic substrates for the electroplated Sn thin films. Prior to deposition, the wafers were cleaned with acetone, methanol, isopropanol and de-ionized (DI) water for 5 minutes each in sequence, followed by drying with compressed nitrogen gas.

The cleaned substrates were mounted on a sample holder and transferred into the Lesker PVD system (Kurt J. Lesker) in the clean room. After the process chamber reached an adequate working pressure (below  $2 \times 10^{-6}$  Torr), the deposition of Ti and Cu layers was performed. A 25 nm Ti layer was then deposited on one side of the substrate, followed by a 35–50 nm Cu layer. The deposition rate was around  $0.5\ \text{\AA}/\text{s}$ . The sample holder was steadily rotated during the deposition to assure uniformity of deposition.

### *2.1.2 Electrodeposition of Sn layer*

A Sn layer then deposited by electrodeposition on the Cu layer of the sample. A commercial Sn electroplating solution (Solderon SC, Dow Chemical) was used. The recipe for the solution is presented in Table 2.1. The solution was prepared by adding the chemicals into a beaker with 400 ml DI water following the order presented in Table 2.1. Moderate stirring was performed during the mixing. Subsequently, the solution was diluted with DI water to one liter in volume.

**Table 2.1.** Recipe for preparing one liter of Solderon SC Tin electroplating solution

Chemical	Quantity (ml)
DI water	400
Solderon Tin HS-300 Concentrate	150
Solderon Acid HC	110
Solderon SC Primary	100
Solderon SC Secondary	5
Solderon RD Concentrate	10

Before electroplating, the sample was etched with 98% sulfuric acid for 10 s to remove the native copper oxide on the surface. The thickness of the Sn layer ranges from 200 nm to 1.85  $\mu\text{m}$ . According supporting documents, the Sn solution is suitable for current density between 5 to 15  $\text{mA}/\text{cm}^2$  with galvanostatic treatment. In this thesis, the deposition rate was chosen according to the target thickness of the Sn layer, in order to fabricate uniform Sn layers. For thickness of Sn layer below 1  $\mu\text{m}$ , the current density 5  $\text{mA}/\text{cm}^2$  ( $\sim 4.2 \text{ \AA}/\text{s}$ ) was used, whereas for thickness above 1  $\mu\text{m}$ , the current density 10  $\text{mA}/\text{cm}^2$  ( $\sim 8.4 \text{ \AA}/\text{s}$ ) was used. Weight measurements were performed before and after electrodeposition to acquire the average thickness of the Sn films. Following Sn electrodeposition, the samples were sequentially cleaned with acetone and DI water for 5 minutes each and dried with compressed nitrogen gas. Note that this cleaning procedure is essential to remove the residue of electrodeposition solution from the surface. After fabrication, the samples were stored in an Ar-filled glove box with moisture and oxygen controlled below 0.1 ppm to minimize the formation of tin oxide. During the storage, Sn and Cu form an intermetallic compound (IMC)  $\text{Cu}_6\text{Sn}_5$  at the Cu/Sn interface at room temperature.<sup>1,2</sup> The formation of IMC improves the adhesion of Sn layer, so the Sn film can remain bonded to the substrate during electrochemical experiments, and the stress

measurements. Since the Cu thickness was only 35-50 nm, most of it is expected to be consumed in forming the IMC. The samples were allowed to sit for a few days to complete the reaction at the Cu/Sn interface. Fig. 2.2 shows a cross-section image an-prepared 1.85  $\mu\text{m}$  Sn sample milled by focused-ion beam (FIB). The dash line indicates the film surface, and the contrast difference indicated multiple orientation of grains in the Sn film. The IMC is also observed at film/substrate interface as marked in Fig. 2.2. After the experiments, the resulting phase composition in the samples were also examined by FIB.

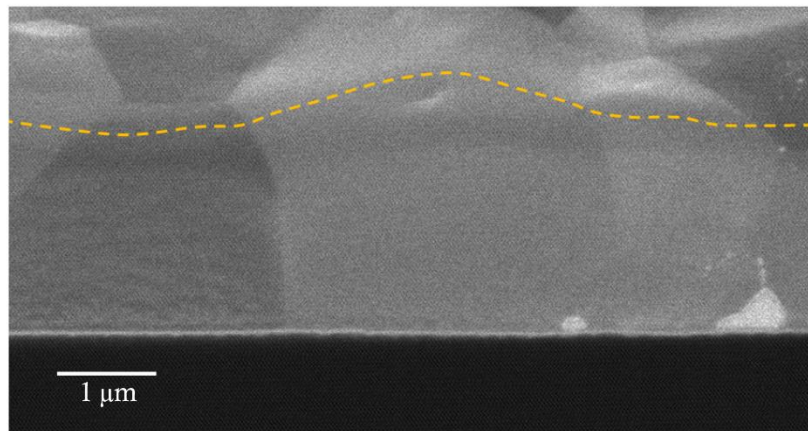


**Figure 2.2.** Cross-section image of an as-prepared 1.85  $\mu\text{m}$  polycrystalline Sn sample. The dash line indicates the film surface.

## 2.2 Electrochemical and *in situ* stress measurement

The fabricated Sn samples were used as anodes in Li-ion batteries in electrochemical experiments. Fig. 2.3 shows the configuration of an experimental setup with a customized electrochemical half cell and the Multi-Beam Optical Stress Sensor (MOSS) technique (k-Space Associates). The cells were assembled and operated in the Ar-filled glove box. The electrochemical measurements were performed using a Multistat 1470 (Solartron Analytical, AMETEK).

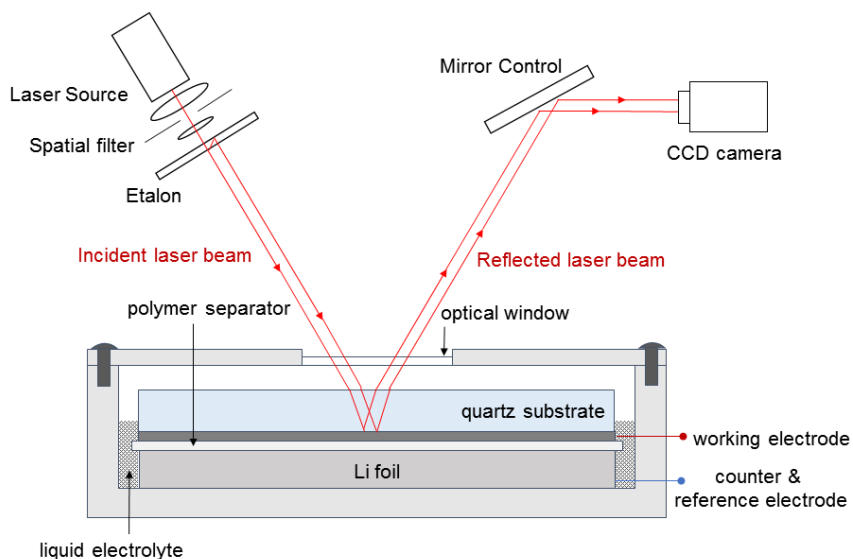


**Figure 2.3.** Electrochemical half cell and the Multi-Beam Optical Stress Sensor (MOSS) setup.

### 2.2.1 Configuration of electrochemical cell

The customized electrochemical cell includes a Teflon beaker, and a stainless steel cap with an optical window (Edmund Optic). In the electrochemical half cell, a 1.5 mm-thick (50.8 mm in diameter) Li metal foil (99.9%, Alfa Aesar) was used as the reference and counter electrode. The Sn film sample served as the working electrode. A stainless steel ring was used to weight down the Li foil. A trilayer polypropylene-polyethylene-polypropylene membrane (25  $\mu\text{m}$  thick, 52 mm diameter, C480, Celgard) sit between the two electrodes as the separator. The type of electrolyte consisted of  $\text{LiPF}_6$  solute with ethylene carbonate (EC) and diethyl carbonate (DEC) solvent (BASF), and its composition is addressed in the experimental section in each chapter. The cell was filled to the level of the substrate while keeping its top surface dry. This ensured that the Sn layer on the bottom surface of the quartz wafer remained submerged in the electrolyte during the

experiment. At the end of the experiment, the cell was opened and the electrolyte level was monitored to ensure the separator and Sn film were soaked in the electrolyte. The samples were cleaned with dimethyl carbonate for 15 minutes to remove any residue of electrolyte on the surface, and stored in the Ar-filled glove box.

### 2.2.2 Multi-beam Optical Stress Sensor

During electrochemical experiment, the stress evolution in Sn films was determined by monitoring the wafer curvature with the MOSS technique.<sup>3</sup> The setup (Fig. 2.3) monitored an array of laser beams that were reflected from the back-side of the substrate into a charge-coupled device (CCD) camera. By Stoney's equation,<sup>4</sup> the curvature of the substrate  $\frac{1}{R}$  is related to the product of stress  $\langle\sigma\rangle$  and thickness  $h_f$  of the film (referred to as stress-thickness)

$$\langle\sigma\rangle h_f = \frac{M_s h_s^2}{6} \frac{1}{R} \quad \{2.1\}$$

where  $h_f$  and  $h_s$  are the thicknesses of the film and the substrate respectively;  $M_s$  is the biaxial modulus of the substrate. For a film consisting of multiple layers, the measured stress-thickness is attributed to the stress and thickness of each layer as

$$\langle\sigma\rangle h_f = \sum_{i=1}^n \langle\sigma_i\rangle h_i \quad \{2.2\}$$

During the experiment, the change in curvature  $\Delta \frac{1}{R}$  was determined by measuring the change in spacing between the reflected beams  $\frac{d-d_o}{d_o}$  as

$$\Delta \frac{1}{R} = \frac{d - d_o}{d_o} \left( \frac{1}{A_m} \right) \quad \{2.3\}$$

where  $d$  is the spacing between laser beams;  $d_o$  is the original spacing of the beams measured before electrochemical experiments, and  $A_m$  is the mirror constant. Here,  $d_o$  is related to the original curvature of the as-prepared Sn film, in which the residual stress from depositions and IMC formation may exist. In this work, the original curvature of the as-prepared Sn sample was taken as the reference. Thus, the measured stress-thickness is the change from the reference state. The mirror constant  $A_m$  is related to the experimental configuration and can be acquired with a flat reference mirror and a mirror of a known curvature (e.g.,  $0.1 \text{ m}^{-1}$ ). Note that the mirror constant was updated accordingly when there was any configurational adjustment to the MOSS system. Prior to the electrochemical treatments, the assembled electrochemical cell was allowed to stabilize for 12 hours after being transported to the MOSS setup.

### 2.3 X-ray diffraction

$\theta$ - $2\theta$  X-ray diffraction (XRD) scans were performed to identify the phases in the samples before and after the electrochemical experiments. The measurements were carried out with a Bruker D8 Discover diffractometer employing a Cu  $K_{\alpha}$  source ( $\lambda = 1.5406 \text{ \AA}$ ) in ambient environment. Note that the lithiated samples may degrade by moisture and air; so, the samples were sealed by Kapton films or customized coin cell casings in advance inside the glove box. The influence of the protections on the XRD results is demonstrated as follow. Fig. 2.4a shows the XRD result of the as-prepared  $1.85 \mu\text{m}$  Sn sample, in which peaks corresponding to Sn are predominant with two small peaks of IMC at  $44^{\circ}$  and  $54^{\circ}$ . The XRD result of the exact Sn sample covered by a  $0.0254 \text{ mm}$  thick Kapton film is shown in Fig. 2.4b; in which two broad peaks at  $22^{\circ}$  and  $27^{\circ}$  induced the Kapton film are presence.

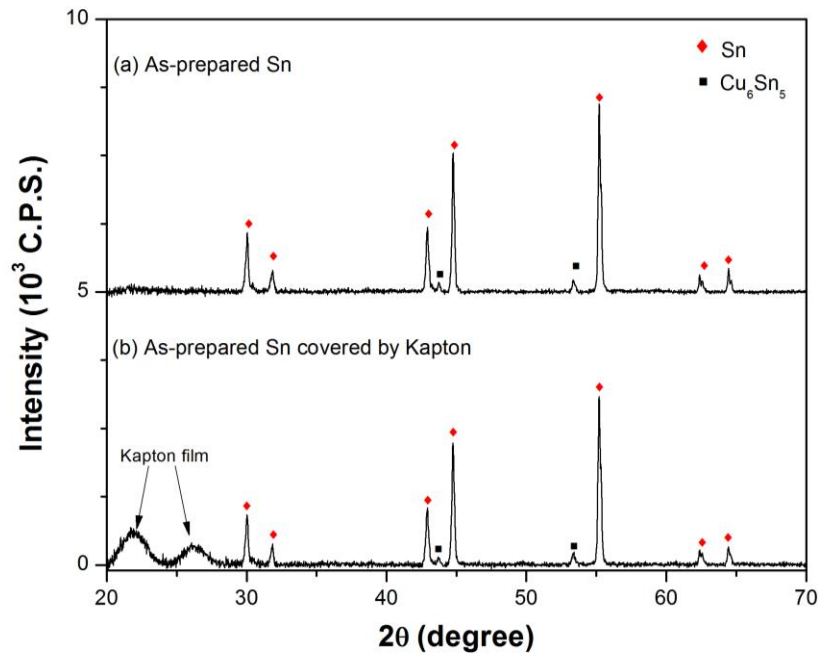


**Figure 2.4.** XRD results of: (a) as-prepared  $1.85 \mu\text{m}$  Sn sample, (b) as-prepared  $1.85 \mu\text{m}$  Sn sample covered by the  $0.0254 \text{ mm}$  thick Kapton film.

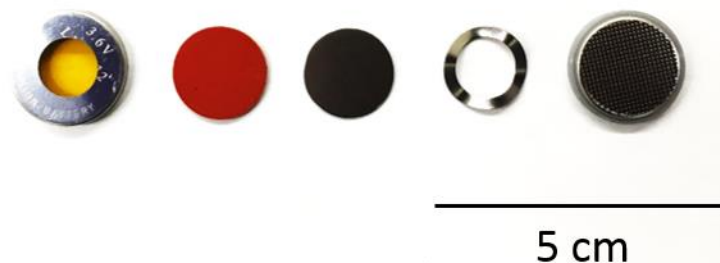


**Figure 2.5.** Customized coin cell casing for XRD the measurement with air-sensitive materials; from left to right: a stainless steel top case with the 0.0254 mm thick Kapton window, a rubber gasket, a stainless steel spacer, a stainless steel spring, and a stainless steel bottom case.

The components of the customized coin cell casing used for isolation of lithiated samples are shown in Fig. 2.5. Similar approaches have been used for *in situ* measurements in literature.<sup>5, 6</sup> The casing consists of a stainless steel top case with a window (0.8 mm in diameter) sealed with Kapton film (0.0254 mm thick), a rubber gasket (1 mm thick), and three stainless steel parts including a spacer, a spring, and a bottom case. The samples were assembled into the casing in the Ar-filled glove box before XRD measurements. Since the entirety of coin cell was exposed to X-ray during the measurements, additional peaks from the cell casing and Kapton were observed in the XRD results as shown in Fig. 2.6. The XRD pattern of a 500 nm thick as-prepared Sn sample is shown in Fig. 2.6a, and the result for an empty casing is shown in Fig. 2.6b, in which the peaks corresponding to Kapton and stainless steel are seen. The XRD result of the 500 nm Sn sample assembled in the casing is presented in Fig. 2.6.c. These protection are applied to the lithiated Sn samples discussed in this thesis.

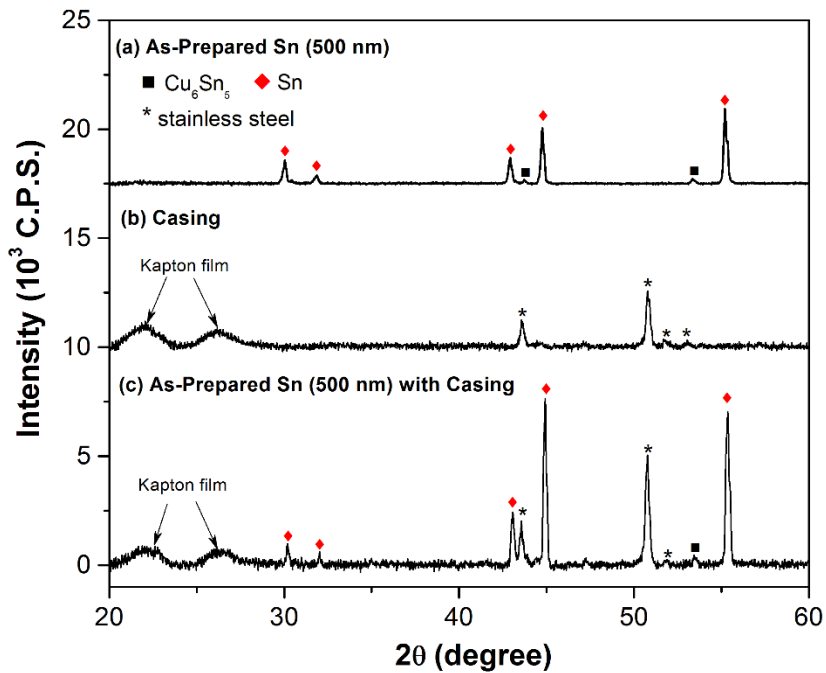


**Figure 2.6.** XRD results of: (a) as-prepared 500 nm Sn sample, (b) empty customized coin cell casing with the 0.0254 mm thick Kapton window, (c) as-prepared 500 nm Sn sample assembled in the customized coin cell casing.

## References

1. N. Jadhav, E. J. Buchovecky, L. Reinbold, S. Kumar, A. F. Bower, and E. Chason, *IEEE Transactions on Electronics Packaging Manufacturing*, **33** (3), 183-192 (2010).
2. F. Pei and E. Chason, *Journal of Electronic Materials*, **43** (1), 80 (2014).
3. E. Chason, *Thin Solid Films*, **526** 1-14 (2012).
4. L. B. Freund and S. Suresh, *Thin Film Materials: Stress, Defect Formation and Surface Evolution*, Cambridge University Press (2009).
5. K. Rhodes, R. Meisner, M. Kirkham, N. Dudney, and C. Daniel, *Journal of The Electrochemical Society*, **159** (3), A294-A299 (2012).
6. D. X. Liu, J. Wang, K. Pan, J. Qiu, M. Canova, L. R. Cao, and A. C. Co, *Angewandte Chemie International Edition*, **53** 9498-9502 (2014).

# Chapter 3.

## Phase and Stress Evolution during Initial Lithiation

---

During electrochemical lithiation, Li atoms diffuse into the Sn anode from the surface. The Sn atoms react with Li atoms and form multiple lithiated Sn phases at different potentials. Most researchers have investigated Sn electrodes via galvanostatic cycling and reported that multiple phase transformations happen simultaneously during the processes.<sup>1-5</sup> Such series of phase transformation make the analysis of Sn electrode more challenging than other electrodes. Therefore, to investigate the kinetics and mechanics associated with the evolution of the individual lithiated phases, we performed potentiostatic experiments with select potentials to control the phase transformations.

In this chapter, the initial phase transformation from Sn phase to  $\text{Li}_2\text{Sn}_5$  phase is studied. By measuring the wafer curvature during lithiation, the stress in Sn,  $\text{Li}_2\text{Sn}_5$  and the solid electrolyte interphase (SEI) layer were determined. A 1-D kinetic model was used to analyze the kinetic coefficients (Li diffusivity and reaction rate coefficient) that control the phase transition.

### 3.1 Experimental condition

#### 3.1.1 Sample description

The multilayer Sn thin film samples described in section 2.1 were used in this study; the configuration includes a 200 nm - 1.85  $\mu\text{m}$  Sn, 50 nm Cu and 25 nm Ti layers on fused-silica wafers (50.8 mm in diameter,  $\sim 500 \mu\text{m}$  thick, double-side polished).

#### 3.1.2 Electrochemical experiment

The Sn thin film sample served as the working electrode and was assembled into the customized electrochemical half cell (Fig. 2.3). Li metal foil was used as the counter and reference electrode. The electrolyte composition was 1.2 M  $\text{LiPF}_6$  in EC/DEC (1:2 wt%). Three kinds of experiments were performed to study the evolution of stress in each layer (SEI,  $\text{Li}_2\text{Sn}_5$  and Sn) and the associated phase transformation kinetics.

The first kind of experiment (referred to as Experiment [i]) was aimed at understanding the stress evolution in Sn layer, and was performed on the 1.85  $\mu\text{m}$  thick Sn samples. The experimental procedure is presented in Table 3.1.

**Table 3.1.** Experimental condition of Experiment [i]: the growth of  $\text{Li}_2\text{Sn}_5$  phase

#	Step	Description
1	galvanostatic lithiation	-25 $\mu\text{A}/\text{cm}^2$ from OCP to 0.8 V
2	SEI formation	Potential held at 0.8 V for 20 hours
3	Sn- $\text{Li}_2\text{Sn}_5$ phase transformation	Potential held at selective value (0.64-0.665 V) for 120 hours

The initial open circuit potential (OCP) was approximately 2.7 V, which is the potential difference between the as-prepared Sn and the Li foil. Lucas et al.<sup>6</sup> reports that the major side reactions of EC-based electrolyte with Sn anodes happen above 1.0 V. Hence, the potential of electrode was held at 0.8 V for 20 hours, after the initial galvanostatic lithiation. The potential hold at 0.8 V was to separate the charge consumption in SEI formation (and other side reactions) as much as possible. Although the SEI can continue to form below 0.8 V, in this work, it is assumed that the contribution of the SEI formation reactions (and other side reactions) to the current density is negligible compared to that due to lithiation of Sn.

Following SEI growth, potentiostatic lithiation was performed at selected potentials below the equilibrium potential corresponding to  $\text{Li}_2\text{Sn}_5$  ( $\sim 0.76$  V)<sup>7</sup> to activate the Sn- $\text{Li}_2\text{Sn}_5$  phase transformation. The potential was held high enough not to activate formations of other lithiated phases at higher Li concentration. Note that the current density varies during the potential hold; thus, the actual potential of the electrode surface would not be truly constant. Here, it is considered to be approximately constant, as reported by others in the literature.<sup>3</sup>

The second type of experiment (referred to as Experiment [ii]) is to investigate the stress evolution during the SEI growth at 0.8 V. Several thicknesses (500 nm-1.85  $\mu\text{m}$ ) of Sn samples were used. The condition of electrochemical experiment is similar to the one presented in Table 3.1. However, the experiments only proceed to step 2 in Table 3.1, which is the SEI layer formation. The details regarding the stress analysis of the SEI layer is discussed in section 3.2.2.

The third kind of experiment (referred to as Experiment [iii]) is to acquire the surface Li concentration at different potential values required in the kinetic analysis. This

experiment was carried on a 200 nm Sn film. After a 20 hour SEI formation at 0.8 V, the potential was held at 0.665 V until the current density decreased below  $-0.04 \mu\text{A}/\text{cm}^2$  ( $\sim C/6500$ ) to fully transform the Sn layer into a  $\text{Li}_2\text{Sn}_5$  layer. Subsequently, the experiment was switched to open circuit to let the Li concentration in the film reach equilibrium as the potential relaxed to around 0.76 V. Following the open circuit, a potentiostatic intermittent titration technique (PITT) experiment was performed; the potential was decreased in 20 mV steps over a range from 0.7 V to 0.64 V. The sample was held at each potential hold until current density decreased below  $-0.025 \mu\text{A}/\text{cm}^2$  ( $\sim C/10000$ ), at which the sample was considered to have reach a new state of charge in equilibrium with the applied potential. The surface Li concentration at each potential hold was assumed to be the same as the averaged Li concentration at that potential. The experimental procedure is shown in Table. 3.2.

**Table 3.2.** Experimental condition of Experiment [iii] : the estimation of surface Li concentration in  $\text{Li}_2\text{Sn}_5$  phase

#	Step	Description
1	galvanostatic lithiation	$-25 \mu\text{A}/\text{cm}^2$ from OCP to 0.8 V
2	SEI formation	Potential held at 0.8 V for 20 hours
3	Sn- $\text{Li}_2\text{Sn}_5$ phase transformation	Potential held at 0.665 V for until the current density below $-0.04 \mu\text{A}/\text{cm}^2$
4	open circuit	10 hours
5	PITT	20 mV step from 0.7 V to 0.64 V with cut-off current density of $-0.025 \mu\text{A}/\text{cm}^2$

### 3.1.3 In situ stress measurement

The MOSS system (section 2.1) was used to measure the real time curvature change  $\frac{1}{R}$  during the electrochemical experiments. During lithiation, Li atoms diffuse into the Sn layer from the surface, where the Sn-Li<sub>2</sub>Sn<sub>5</sub> transformation initiates. In addition, a layer of SEI induced by electrolyte decomposition is located at the anode surface. For such system consisting with multiple layers, the measured curvature is related to the change in stress and thickness of the layers that involves Li incorporation by the Stoney equation.<sup>8</sup> For the current experiments, it can be represented as

$$\frac{M_s h_s^2}{6} \frac{1}{R} = \langle \sigma \rangle h_f = \langle \sigma_{SEI} \rangle h_{SEI} + \langle \sigma_{Sn} \rangle h_{Sn} + \langle \sigma_{Li_2Sn_5} \rangle h_{Li_2Sn_5} \quad \{3.1\}$$

where the subscripts indicate the average stress and thickness in the SEI, Sn, and Li<sub>2</sub>Sn<sub>5</sub> layers respectively.  $M_s$  and  $h_s$  are the biaxial modulus and thickness of the substrate, respectively. This analysis assumes that the layers can be treated as uniform in thickness and stress. Note that the above equation does not include contributions from Ti and intermetallic compound Cu<sub>6</sub>Sn<sub>5</sub>. Based on the Li-Ti phase diagram,<sup>9</sup> we consider the Ti layer to be inert to Li, hence it is not expected to contribute to change of curvature during lithiation. The intermetallic compound Cu<sub>6</sub>Sn<sub>5</sub> has been studied as an anode material for Li-ion batteries, and its lithiation potential is reported to be 0.4 V and lower.<sup>10</sup> Since the potential range of the experiments in this work was between 2.7 and 0.64 V, Cu<sub>6</sub>Sn<sub>5</sub> is not expected to lithiate and contribute to curvature change.

### 3.1.4 Focused-ion beam and X-ray diffraction analysis

Focused-ion beam (FIB) cross-section and  $\theta$ - $2\theta$  X-ray diffraction (XRD) were performed before and after the electrochemical experiments to examine the film thickness and identify the phases in the Sn samples. Cross-sections of the as-prepared sample and the lithiated sample after potentiostatic lithiation at 0.665 V for 120 hours are shown in Fig. 3.1. The Sn/Li<sub>2</sub>Sn<sub>5</sub> phase boundary is marked with a dotted line in Fig. 3.1b. The corresponding XRD results of the as-prepared and lithiated sample are shown in Fig. 3.2. Since the lithiated Sn samples can be degraded by moisture and air, the lithiated Sn samples were sealed by a Kapton film (0.0254 mm) in the Ar-filled glovebox, before performing the XRD measurements in ambient environment as discussed in section 2.3. For consistency, in Fig. 3.2a the as-prepared Sn sample was covered by the Kapton film during XRD measurement; two broad peaks at 22° and 27° induced by the Kapton film are noticed. The XRD result of the sample lithiated at 0.665 V (also covered by the Kapton film) is presented in Fig. 3.2b. The findings confirm the presence of only Sn and Li<sub>2</sub>Sn<sub>5</sub> phases in the anode, as expected from the processing conditions.

The FIB cross-section and XRD of the as-prepared sample (Fig. 3.1a and Fig. 3.2a) did not show evidence of a significant Sn oxide layer at the surface of the sample, so we neglect the effect of Sn oxide in our analysis of the electrochemical experiments and curvature measurements.

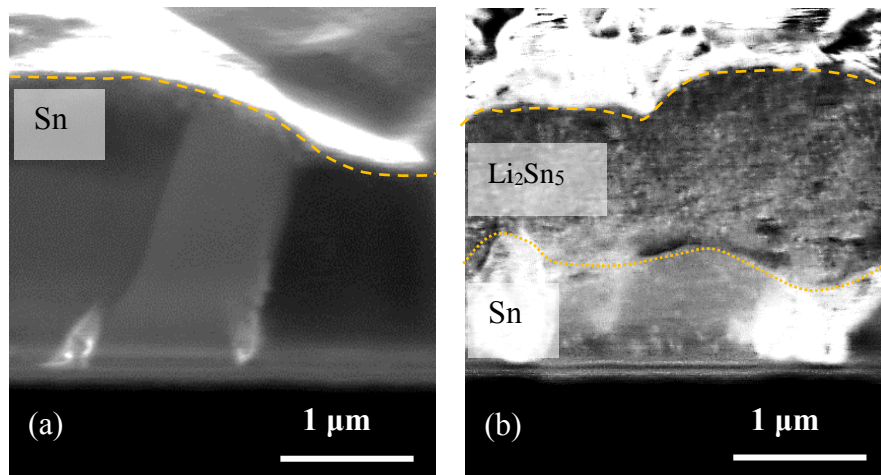


**Figure 3.1.** Cross section images of: (a) as-prepared Sn film sample (surface indicated by dashed line), (b) sample lithiated at 0.665 V, showing the Sn/ $\text{Li}_2\text{Sn}_5$  phase boundary (dotted line).

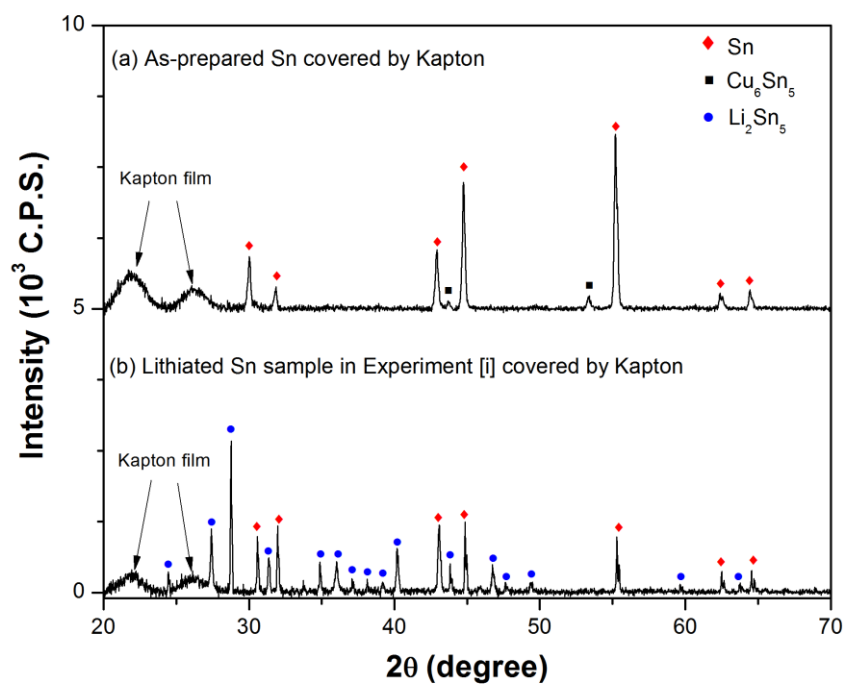


**Figure 3.2.** XRD results of: (a) as-prepared Sn sample, (b) lithiated Sn sample after potentiostatic lithiation at 0.665 V for 120 hours, showing presence of both Sn and  $\text{Li}_2\text{Sn}_5$  phases. Both samples were covered by the 0.0254 mm thick Kapton film.

## 3.2 Results and discussion

### 3.2.1 Observation in electrochemical and stress measurements

Fig. 3.3 shows a data set of Experiment [i] carried on a 1.85  $\mu\text{m}$  Sn layer. The top part of the figure (Fig. 3.3a) shows the measured current density. The corresponding stress-thickness measurement performed simultaneously is shown in Fig. 3.3b. In the measurement, the sample was first held at 0.8 V for 20 hours to grow a SEI layer. After the SEI formation stage, the potential was lowered to 0.665 V for 120 hours to grow the  $\text{Li}_2\text{Sn}_5$  phase.

During the potential hold at 0.8 V, the current density during this period decays to a small value of ( $\sim -0.1 \mu\text{A}/\text{cm}^2$ ), indicating that the SEI formation is saturated at that potential. The corresponding stress-thickness rapidly reaches a fairly constant negative value. The negative sign indicates that the average stress is compressive. Since there is no phase transformation in the Sn at this potential, the measured stress-thickness is the result of stress from SEI formation or in the Sn film. Experiments to determine how much stress is in each of these layers are described in the next section (3.2.2).

Following the SEI growth, the potential was held at 0.665 V to initiate Sn- $\text{Li}_2\text{Sn}_5$  phase transformation. When the potential is lowered to 0.665 V, the initial transient current density variation is complex. As shown in the inset of Fig. 3.3a, the current density jumps to a large negative value (more than  $-5 \mu\text{A}/\text{cm}^2$ ) when the potential is changed. The magnitude of the negative current then decreases rapidly to  $\sim -1 \mu\text{A}/\text{cm}^2$  within 40 s, followed by a slower increase to  $\sim -2.5 \mu\text{A}/\text{cm}^2$  over the subsequent 800 s. This is followed by a monotonic and continuous decrease for the remaining duration of the experiment.

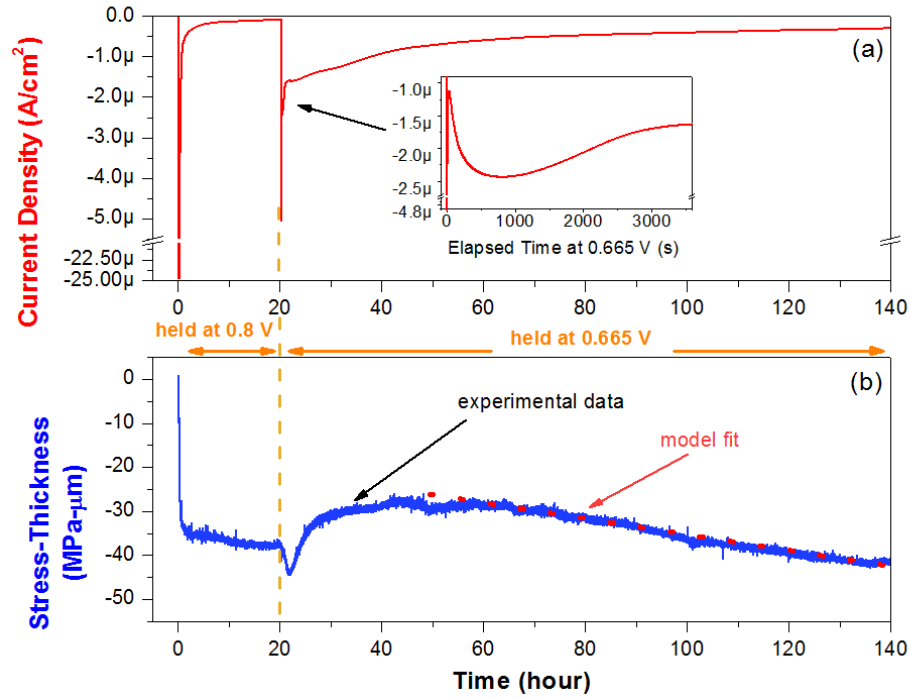


**Figure 3.3.** Time evolution of: (a) current density and (b) stress-thickness during growth of SEI at 0.8 V for 20 hours followed by potentiostatic lithiation at 0.665 V for 120 hours. The inset in (a) corresponds to the period after the start of lithiation. The dashed line in (b) is the result of fitting to the steady-state model described in text.

The curvature measurement shown in Fig. 3.3b also exhibits a complex transient behavior over the same initial period. The stress-thickness rapidly becomes more negative immediately after the potential is changed to 0.665 V, reaching a maximum negative value of  $\sim -45$  MPa- $\mu\text{m}$  at approximately 2 hours after the potential change. For longer times, the stress-thickness becomes less compressive until it reaches  $\sim -30$  MPa- $\mu\text{m}$  (in  $\sim 22$  hours after the potential change). Subsequently, the magnitude of stress-thickness increases steadily, evolving at an approximately constant rate, as seen in Fig. 3.3b beyond 55 hours. We attribute the complex transient behavior when the potential is lowered to 0.665 V to the interaction of multiple processes in the early stages of Sn-Li<sub>2</sub>Sn<sub>5</sub> phase transformation. Levi et al.<sup>11</sup> observed similar transient behavior in current measurements

at the beginning of potentiostatic lithiation of graphite electrodes. They suggested that the initial rapid decrease in the current density may be related to double layer charging at the surface, Li insertion into the anode and nucleation barrier for phase transformation. As nuclei of the new phase start to grow, the phase boundary area grows, resulting in increase in Li flux and thus the current density (re-increases to  $\sim -2.5 \mu\text{A}/\text{cm}^2$  at 800 s).

The stress-thickness evolution is influenced by the fact that the new phase does not nucleate immediately when the potential is changed from 0.8 to 0.665 V. During the nucleation period, additional Li can diffuse into the Sn layer above the equilibrium concentration, resulting in volume expansion, plastic strains and compressive yield stress that depends on plastic strain rate. Such rate-dependent yield stress, i.e., viscoplasticity, was reported for Pb-Sn alloy.<sup>12</sup> Because it results from a combination of nucleation kinetics and rate-dependent plasticity, the transient behavior observed in the current density and stress-thickness in the early stage of lithiation requires a sophisticated analysis and is discussed in chapter 4. However, in the later stage of  $\text{Li}_2\text{Sn}_5$  growth the current density and stress-thickness kinetics approach a more uniform steady-state behavior. FIB cross-section of the layer structure shows that the interface between the  $\text{Li}_2\text{Sn}_5$  and Sn layers moves forward with a relatively homogeneous phase front (Fig. 3.1b). Therefore, in section 3.2.3, we approximate the interface evolution with a 1-D model that enables us to extract kinetic parameters that control phase growth in this steady-state regime so as the determination of the corresponding stress in the  $\text{Li}_2\text{Sn}_5$  and Sn layer.

### 3.2.2 Determination of stress in the solid electrolyte interphase, Sn, and $\text{Li}_2\text{Sn}_5$ layers

During the potential hold at 0.8 V, we assume that all the charge is consumed by either the growth of the SEI layer or Li incorporation into the Sn layer as a solid solution since the potential is above the threshold for new phase formation. A single measurement in Fig. 3.3 cannot determine the relative contribution of the SEI and the Sn film to the measured stress-thickness change. However, this question can be addressed by measuring the stress-thickness evolution under the same experimental procedure with different Sn layer thicknesses. Since the SEI formation happens at the surface of the Sn layer, we expect that its growth rate and stress state are not affected by the thickness of the Sn layer beneath it. Hence, in Eq. (3.1),  $\langle\sigma_{SEI}\rangle h_{SEI}$  is expected to be independent of Sn layer thickness  $h_{Sn}$ , whereas the contribution from lithiation of Sn layer  $\langle\sigma_{Sn}\rangle h_{Sn}$  is expected to scale linearly with  $h_{Sn}$ .

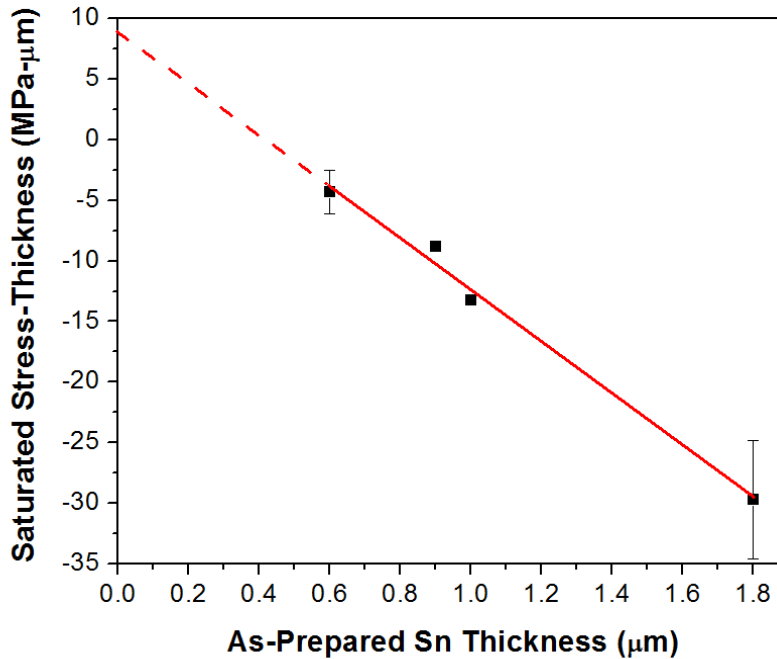


**Figure 3.4.** Value of saturated stress-thickness for samples with different initial Sn thickness during the 20-hour growth of SEI at 0.8 V.

Measurements of the curvature for different Sn layer thicknesses after holding for 20 hours at 0.8 V are shown in Fig. 3.4. The measured stress-thickness values depend linearly on the thickness of the Sn layer. The slope of a linear fit to the data (solid line in Fig. 3.4) indicates that the average stress in the Sn layer has a value of -16.4 MPa at this potential. This value is close to the yield stress of electroplated Sn film of similar thickness<sup>13</sup> which suggests that lithiation of Sn at 0.8 V may be sufficient to take the Sn film to a state of yield.

The stress in the SEI layer can be determined by extrapolating the data points in Fig. 3.4 to zero Sn thickness (i.e., the intercept of the dashed line in Fig. 3.4 with the ordinate), which reveals  $\langle\sigma_{SEI}\rangle h_{SEI}$  to be approximately 8.8 MPa- $\mu\text{m}$ ; thus the SEI layer is in tension. Tensile stress in the SEI layer has been reported for Si<sup>14</sup> and Au<sup>15</sup> as well. Taking the thickness of the SEI layer on Sn to be approximately 100 nm (from Ref. 6), the stress in SEI layer can be estimated to be  $\sim 88$  MPa. The origin and mechanism of stress generation in SEI is unknown as present.

As shown in Fig. 3.3b, the stress-thickness evolution at the early stages of  $\text{Li}_2\text{Sn}_5$  growth is complicated by the supersaturation and viscoplastic response of the Sn layer. However, in the steady-state regime, the supersaturation in Sn decays and  $\text{Li}_2\text{Sn}_5$  layer grows into the Sn layer at a relatively uniform rate. Hence, we focus on the stress-thickness evolution during the steady-state regime. We interpret the measurement by considering the film to consist of two uniform layers ( $\text{Li}_2\text{Sn}_5$  and supersaturated Sn) with different average stress and thickness.

In the steady-state, the stress-thickness has contributions from multiple layers (described in Eq. 3.1): the SEI at the surface, the growing  $\text{Li}_2\text{Sn}_5$  layer and the remaining supersaturated Sn layer. As assumed in the preceding session, the SEI is considered to

reach saturation during the 0.8 V potential hold for 20 hours, and that the value of  $\langle\sigma\rangle_{SEI}h_{SEI}$  would not change appreciably during the subsequent lithiation. This is clearly an assumption to facilitate data analysis since SEI may continue to evolve when the potential is lowered. Therefore, the change in stress-thickness after the potential is lowered to activate the Sn- $\text{Li}_2\text{Sn}_5$  phase transformation is attributed to changes in the Sn layer and  $\text{Li}_2\text{Sn}_5$  layer.

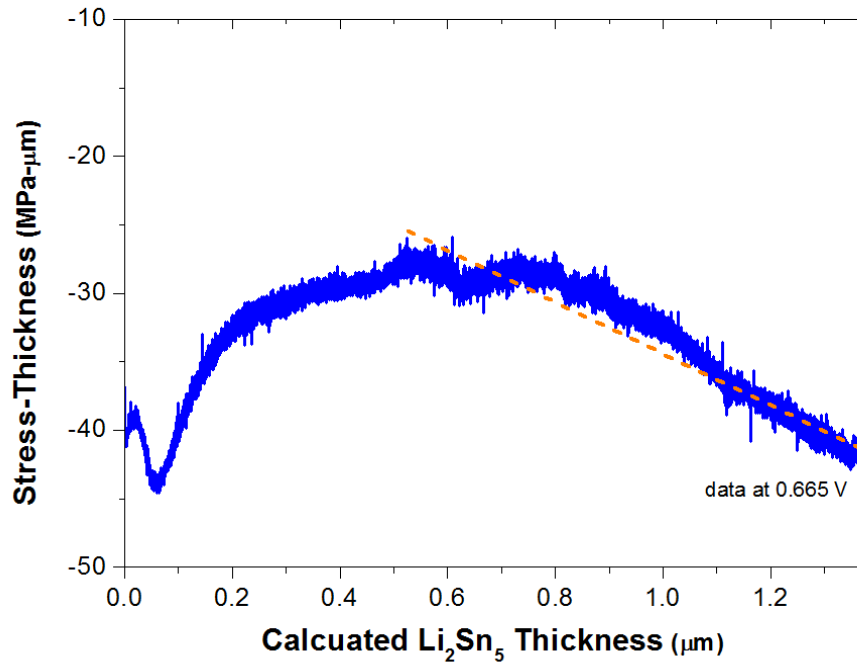


**Figure 3.5.** Measured stress-thickness vs.  $\text{Li}_2\text{Sn}_5$  thickness for lithiation at 0.665 V. Dashed line is used to estimate the slope in the steady-state regime.

As discussed above in this section, the supersaturated Sn layer is expected to be in a state of yield at the corresponding yield stress of -16.4 MPa. Similarly, the stress in the  $\text{Li}_2\text{Sn}_5$  layer is also assumed to be uniform at its yield stress since the 22% volumetric strain from Sn is too large to be accommodated by elastic strain.<sup>4, 16</sup> Therefore, the steady-

state stress-thickness dependence of the measured curvature on the  $\text{Li}_2\text{Sn}_5$  (shown in Fig. 3.5) can be described by

$$\frac{\partial \langle \sigma \rangle h_f}{\partial h_{\text{Li}_2\text{Sn}_5}} = \langle \sigma_{\text{Sn}} \rangle \frac{\partial h_{\text{Sn}}}{\partial h_{\text{Li}_2\text{Sn}_5}} + \langle \sigma_{\text{Li}_2\text{Sn}_5} \rangle \quad \{3.2\}$$

where  $\partial h_{\text{Sn}}/\partial h_{\text{Li}_2\text{Sn}_5}$  describes the change in Sn thickness as the  $\text{Li}_2\text{Sn}_5$  thickness increases, and its value can be determined to be -0.82 which is the inverse of the volume expansion ratio across the phase boundary. From the measured slope of the stress-thickness vs. thickness in Fig. 3.5, we obtain the steady-state yield stress of  $\text{Li}_2\text{Sn}_5$  ( $\langle \sigma_{\text{Li}_2\text{Sn}_5} \rangle$ ) to be around -29.2 MPa.

This result is very different from the value of approximately -1 GPa reported by Mukhopadhyay et al.,<sup>4</sup> who carried out curvature measurement on evaporated Sn film during electrochemical cycling. The reasons for the difference are unknown at present. One difference between the Sn films in the two studies is the grain size; it is 1-2  $\mu\text{m}$  (columnar grains) in our study in contrast to 150 nm in Ref. 5. Tavassol et al.<sup>5</sup> reported curvature measurements during electrochemical cycling of isolated Sn particles supported on elastic substrates. Although the measured curvature changes in their work are comparable in magnitude to those in the present study, a more quantitative comparison cannot be performed due to the difference in the Sn morphology (electroplated films in our study vs. dispersed particles) and the large variation of the Sn particle sizes in their study.

### 3.2.3 Linear kinetic model – the steady-state phase transformation

In Fig. 3.1b, the FIB cross section shows that the  $\text{Li}_2\text{Sn}_5$  phase front progresses relatively uniformly across the Sn layer in the later stage of lithiation in Fig. 3.3 (steady-state regime). Therefore, in this section we use a 1-D model to interpret the steady-state current density electrochemical measurements and determine the kinetic parameters that control the phase transformation.

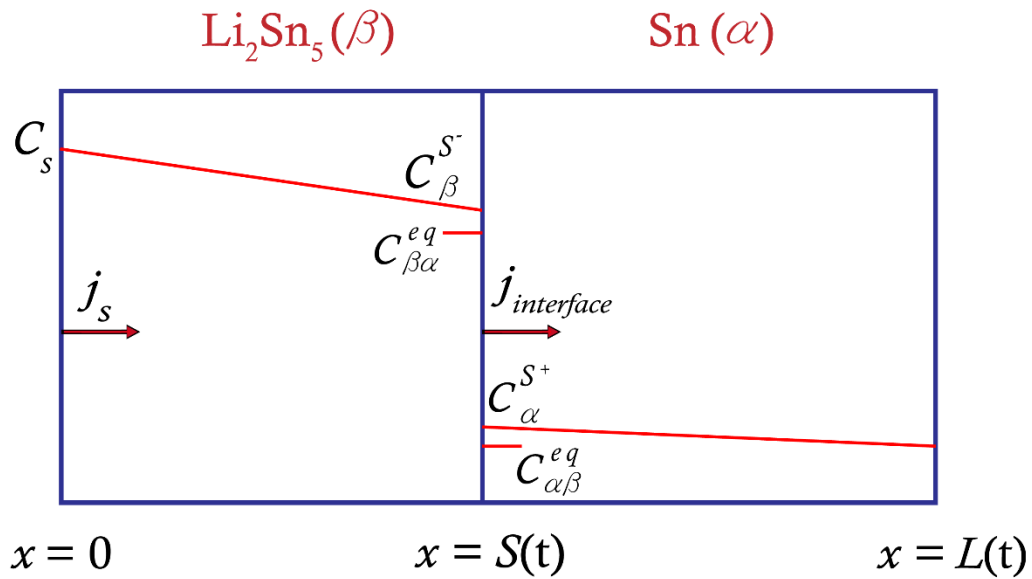


**Figure 3.6.** Schematic plot of the steady-state model for the kinetics of interface motion.

The model considers that the velocity of the interface is controlled by both the supersaturation at the interface (i.e., Sn/ $\text{Li}_2\text{Sn}_5$  phase boundary) and the rate of Li diffusion across the lithiated phase. A schematic of the geometry that indicates the relevant parameters is shown in Fig. 3.6. Here, the entire anode,  $0 < x < L(t)$ , is subdivided into regions of Sn phase and  $\text{Li}_2\text{Sn}_5$  phase by a phase boundary  $S(t)$ .  $L(t)$  is a function of time since the Sn-  $\text{Li}_2\text{Sn}_5$  phase transformation involves a volume expansion.

The Sn phase is referred to as  $\alpha$  phase, and the  $\text{Li}_2\text{Sn}_5$  phase is  $\beta$  phase.  $C_s$  denotes the Li concentration at anode surface in contact with electrolyte.  $C_{\alpha\beta}^{eq}$  is the equilibrium Li concentration at the interface in  $\alpha$  phase, which is considered to be the Li solubility in Sn phase.  $C_{\beta\alpha}^{eq}$  is the equilibrium Li concentration at the interface in  $\beta$  phase, which is assumed to be the stoichiometric Li concentration of  $\text{Li}_2\text{Sn}_5$  phase (i.e., 0.4 Li atom per Sn atom). While the phase boundary progresses, the Li concentrations at the interface are expected to deviate from the equilibrium values; here, they are denoted as  $C_\beta^{S-}$  and  $C_\alpha^{S+}$  as shown in Fig. 3.6. The assumption of steady-state is that the Li concentration has a linear profile (which has also been seen in neutron depth profiling spectroscopy by Liu et al.<sup>3</sup>) In other words, the interface motion is slow enough so that the concentration profile can achieve a near steady-state profile as the thickness evolves. This simple model has previously been used by Deal and Grove<sup>17</sup> for modeling the oxidation of Si under mixed control of diffusion and interface kinetics. The role of SEI layer is ignored in this simple kinetic model.

The interface velocity is assumed to be controlled by two fluxes within the Sn electrode. The first one,  $j_s$ , is the flux of Li from the surface diffusing across the newly forming layer. We assumed it can be described by the Fick's first law as

$$j_s = -D_\beta \frac{\partial C}{\partial x} = D_\beta \frac{C_s - C_\beta^{S-}}{s} \quad \{3.3\}$$

where  $D_\beta$  is Li diffusivity in  $\text{Li}_2\text{Sn}_5$  phase (assumed to be independent of concentration);  $C_s$  is the Li concentration in  $\text{Li}_2\text{Sn}_5$  at the anode surface;  $C_\beta^{S-}$  is the Li concentration in

$\text{Li}_2\text{Sn}_5$  at the interface, and  $S$  is the thickness of the  $\text{Li}_2\text{Sn}_5$  layer. The mechanism of Li diffusion in the anode may be more complicated than the simple concentration-independent diffusivity that we are employing here. However, without further information, we use this approximation in order to see if this classic Deal and Grove model can capture the measured steady-state reaction.

The second flux,  $j_{interface}$ , is the flux across the interface that is related to the interface velocity,  $v_{interface}$  through mass balance across the interface.

$$j_{interface} = v_{interface} \Delta C^S \quad \{3.4\}$$

where  $\Delta C^S$  is the jump in concentration across the interface, and is given by the difference between the equilibrium Li concentration in  $\text{Li}_2\text{Sn}_5$  ( $C_{\beta\alpha}^{eq}$ ) and Sn ( $C_{\alpha\beta}^{eq}$ ) and the difference between the excess Li concentration in each phase ( $\delta C_{\beta}^{S-}$  and  $\delta C_{\alpha}^{S+}$ ).

$$\Delta C^S = C_{\beta}^{S-} - C_{\alpha}^{S+} = (C_{\beta\alpha}^{eq} + \delta C_{\beta}^{S-}) - (C_{\alpha\beta}^{eq} + \delta C_{\alpha}^{S+}) = \Delta C^{S,eq} + \delta C^{S,ex} \quad \{3.5\}$$

where  $\Delta C^{S,eq} = C_{\beta\alpha}^{eq} - C_{\alpha\beta}^{eq}$  and  $C^{S,ex} = \delta C_{\beta}^{S-} - \delta C_{\alpha}^{S+}$ . In addition, since the phase boundary motion is driven by the excess concentration on the  $\text{Li}_2\text{Sn}_5$  side, the phase boundary velocity may be represented as

$$v_{interface} = K_{\alpha\beta} (C_{\beta}^{S-} - C_{\beta\alpha}^{eq}) \quad \{3.6\}.$$

where  $K_{\alpha\beta}$  is a reaction rate coefficient that relates the interface velocity to the local supersaturation at the interface.

Substituting the terms in Eq. (3.4) with Eqs. (3.5) and (3.6), we can write  $j_{interface}$  in the following form:

$$j_{interface} = K_{\alpha\beta}(C_{\beta}^{S^-} - C_{\beta\alpha}^{eq})(\Delta C^{S,eq} + \delta C^{S,ex}) \cong K_{\alpha\beta}(C_{\beta}^{S^-} - C_{\beta\alpha}^{eq})\Delta C^{S,eq} \quad \{3.7\}$$

Note that the  $\delta C^{S,ex}$  term is neglected in Eq. (3.7) by assuming it to be small compared to  $\Delta C^{S,eq}$ .

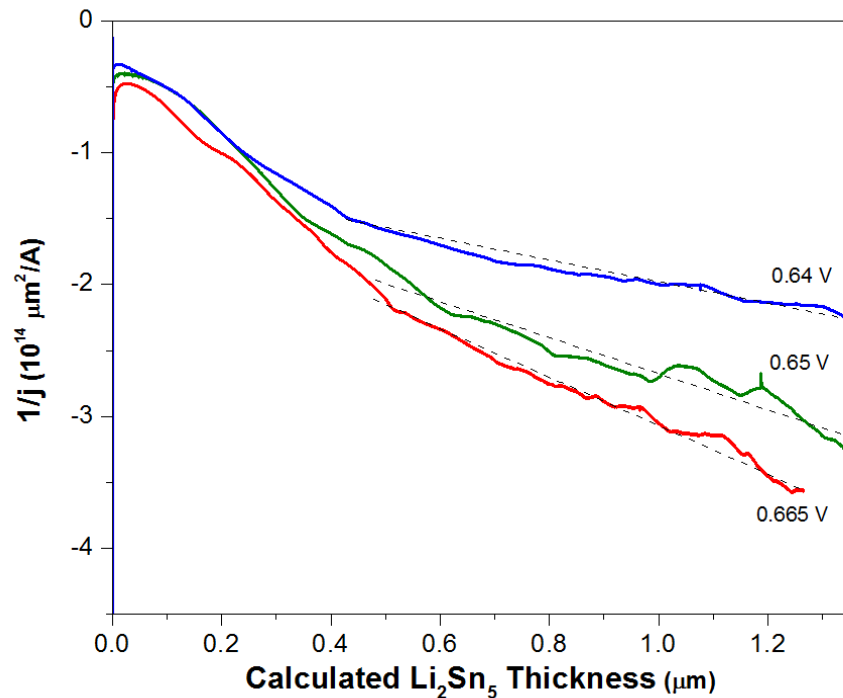
We assume that in the steady-state, the fluxes in Eqs. (3.3) and (3.7) are equal, i.e.,  $j_s = j_{interface}$ , which implies that all the Li inserted into the electrode diffuses across the  $\text{Li}_2\text{Sn}_5$  layer and is consumed at the interface by the formation of new lithiated phase. This determines the value of the concentration at the interface  $C_{\beta}^{S^-}$  which leads to a linear relationship between the reciprocal of flux  $1/j$  and the  $\text{Li}_2\text{Sn}_5$  thickness  $S$ .

$$\frac{1}{j} = \frac{1}{D_{\beta}(C_s - C_{\beta\alpha}^{eq})} S + \frac{1}{K_{\alpha\beta}(C_s - C_{\beta\alpha}^{eq})\Delta C^{S,eq}} \quad \{3.8\}$$

Eq. (3.8) indicates that the inverse current density ( $1/j$ ) should vary linearly with the thickness of the lithiated phase  $S$  if the assumptions behind the model are reasonable.

To compare this model with the data, we plot the inverse current density vs. the thickness of the lithiated phase for different values of the potential (0.665, 0.65 and 0.64 V) in Fig. 3.7. The thickness was calculated from the coulombic charge inserted into the

electrode after the potential is decreased from the 0.8 V hold. It is further assumed that the charge inserted below 0.8 V goes entirely toward the formation of  $\text{Li}_2\text{Sn}_5$  (i.e., the contribution of additional SEI formation is neglected). This assumption was validated by FIB cross-section after lithiation. For instance, the calculated thicknesses of  $\text{Li}_2\text{Sn}_5$  and Sn from the measured charge at the end of the lithiation are  $1.2 \mu\text{m}$  and  $0.9 \mu\text{m}$  respectively (after accounting for volume expansion during phase transformation). These values are consistent with cross-section images showing in Fig. 3.1b. Both Sn and  $\text{Li}_2\text{Sn}_5$  were identified in XRD scanning (Fig. 3.2b) showing that the Sn layer at the bottom of the electrode remains polycrystalline as the top part of the electrode is transformed into  $\text{Li}_2\text{Sn}_5$  phase.



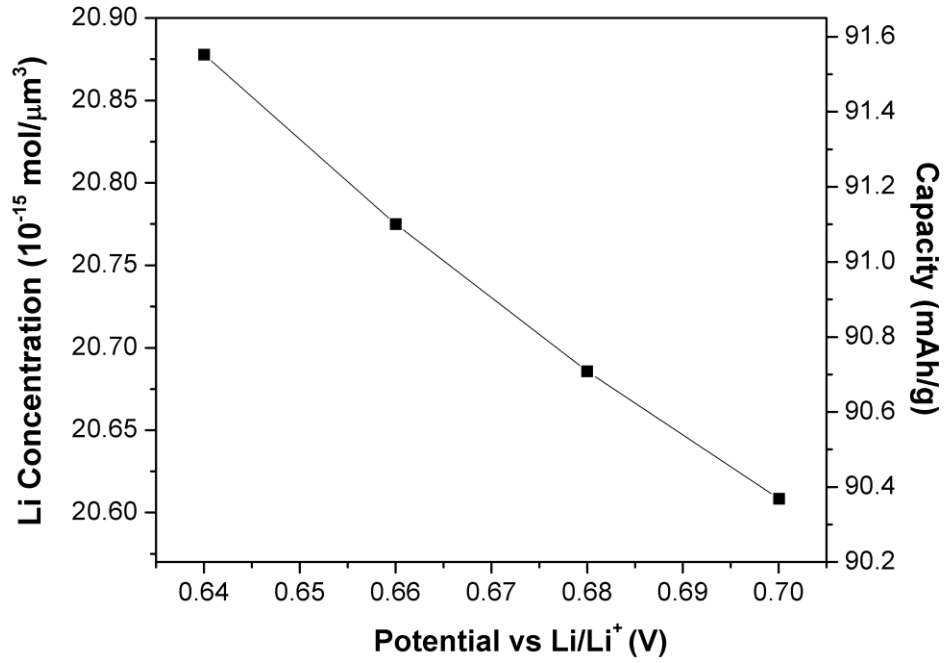
**Figure 3.7.** Inverse current density ( $1/j$ ) vs.  $\text{Li}_2\text{Sn}_5$  thickness for lithiation at 0.665 V, 0.65 V and 0.64 V.

Fig. 3.7 shows the relation between the inverse current density and the calculated thickness of  $\text{Li}_2\text{Sn}_5$ . From the stress-thickness in Fig. 3.3b, the phase boundary appears to propagate in steady-state after 55 hours which corresponding to  $\text{Li}_2\text{Sn}_5$  thickness of 0.45  $\mu\text{m}$ . Hence, we choose to fit to Eq. (3.8) to the data in Fig. 3.7 for thickness greater than 0.45  $\mu\text{m}$ . The observation that the inverse current density becomes linear sooner at 0.64 V may be attributed to the higher driving force for nucleation at lower potentials, which shortens the time before steady-state growth sets in. Values of the parameters obtained from a weighted least-squares fit of the data to the model in Eq. (3.8) are shown in Table 3.3. The fitting was performed to obtain estimates of the parameters that are consistent with the behavior predicted by the model. In obtaining these values, we assume the equilibrium Li concentration in Sn,  $C_{\alpha\beta}^{eq}$  to be negligible; thus  $\Delta C^{S,eq} \cong C_{\beta\alpha}^{eq}$  is taken to be  $2.059 \times 10^{-15} \text{ mol}/\mu\text{m}^3$  as suggested by the stoichiometric composition. Note that the fitting parameters are equal to the product of  $D_\beta$  and  $K_{\alpha\beta}$  with the supersaturation ( $C_s - C_{\beta\alpha}^{eq}$ ).

**Table 3.3.** Coupled parameters obtained from fitting Eq. (3.8) to the experimental data

Applied Potential (V vs. Li/Li <sup>+</sup> )	$D_\beta (C_s - C_{\beta\alpha}^{eq})$ ( $\times 10^{-16} \text{ mol cm}^{-1}\text{s}^{-1}$ )	$K_{\alpha\beta} (C_s - C_{\beta\alpha}^{eq})$ ( $\times 10^{-10} \text{ cm s}^{-1}$ )
0.665	4.9	5.1
0.650	7.6	3.9
0.640	11.5	4.6

To obtain the values of these kinetic parameters, the result of the surface Li concentration  $C_S$  at different applied potential acquired (Fig. 3.8) from Experiment [iii] is used. The figure also shows the corresponding Li capacity. Combining this data with the results shown in Table 3.3, we can determine the parameters  $D_\beta$  and  $K_{\alpha\beta}$  (Table 3.4) at the potentials (0.665, 0.65 and 0.64 V).



**Figure 3.8.** Surface Li concentration  $C_S$  in the  $\text{Li}_2\text{Sn}_5$  phase at different applied potentials.

**Table 3.4.** Evaluation of kinetics parameters by using the  $C_S$  value in Fig. 3.7

Applied Potential (V vs. Li/Li <sup>+</sup> )	$D_\beta$ ( $\times 10^{-12} \text{ cm}^2\text{s}^{-1}$ )	$K_{\alpha\beta}$ ( $\times 10^{-6} \text{ cm}^4 \text{ mol}^{-1} \text{ s}^{-1}$ )
0.665	3.1	3.1
0.650	3.2	1.6
0.640	3.9	1.6

The results in Table 3.4 show that the diffusivity  $D_\beta$  obtained from the measurement doesn't vary appreciably at different potentials, in reasonable agreement with the *a priori* assumption. The values of  $K_{\alpha\beta}$  extracted from the experiments are quite closed to each other at the two lower potentials, and differs by a factor of two at 0.665 V, which is a reasonable in view of typical larger variation in measurements of kinetic parameters in solid state reaction. The range of diffusivity values in Table 3.4 is comparable with the values reported of Sn film by Xie et al.<sup>18</sup> through the galvanostatic intermittent titration technique (GITT) measurements, and Pridatko<sup>19</sup> through galvanostatic cycling. However, it is 3 to 4 orders of magnitude smaller than the diffusivity values reported for other Li-Sn phases by Huggins et al.<sup>20</sup> and Liu et al.<sup>3</sup> This diffusivity difference between thin film and bulk materials is also seen in Li-Bi system,<sup>21</sup> Li-Mg system,<sup>22</sup> and Li-TiS<sub>2</sub> system.<sup>23</sup>

### 3.3 Conclusions

In this chapter, we used potentiostatic lithiation at selected potentials to study phase transformation from Sn to the first lithiated phase Li<sub>2</sub>Sn<sub>5</sub> in the Li-Sn system. By applying a 1-D diffusion model, kinetic parameters were determined. With simultaneous curvature measurements during electrochemical experiments, we obtained stress in the SEI, Sn and Li<sub>2</sub>Sn<sub>5</sub> layers. The main conclusions of this chapter are:

- During SEI growth at 0.8 V prior to Sn-Li<sub>2</sub>Sn<sub>5</sub> phase transformation, Sn layer reaches a state of yield (around -16 MPa), and SEI develops tensile stress (around 9 MPa).
- By employing a steady-state model, the kinetic parameters were obtained. Li diffusivity in Li<sub>2</sub>Sn<sub>5</sub> is around 10<sup>-12</sup> cm<sup>2</sup>/s and the reaction rate coefficient of Sn-Li<sub>2</sub>Sn<sub>5</sub> phase transformation is around 10<sup>-16</sup> cm<sup>4</sup>/mol s (Table 3.4).

- The yield stress of  $\text{Li}_2\text{Sn}_5$  is determined to be around -29 MPa by interpreting the stress-thickness evolution in the steady-state regime.
- A complex transient behavior was observed in both electrochemistry and curvature measurement at the beginning of Sn- $\text{Li}_2\text{Sn}_5$  phase transformation, and it is analyzed numerically in chapter 4.

## References

1. K. Rhodes, R. Meisner, M. Kirkham, N. Dudney, and C. Daniel, *Journal of The Electrochemical Society*, **159** (3), A294-A299 (2012).
2. I. A. Courtney and J. R. Dahn, *Journal of The Electrochemical Society*, **144** (6), 2045-2053 (1997).
3. D. X. Liu, J. Wang, K. Pan, J. Qiu, M. Canova, L. R. Cao, and A. C. Co, *Angewandte Chemie International Edition*, **53** 9498-9502 (2014).
4. A. Mukhopadhyay, R. Kali, S. Badjate, A. Tokranov, and B. W. Sheldon, *Scripta Materialia*, **92** 47-50 (2014).
5. H. Tavassol, M. W. Cason, R. G. Nuzzo, and A. A. Gewirth, *Advanced Energy Materials*, **5** 1400317 (2015).
6. I. T. Lucas, E. Pollak, and R. Kostecki, *Electrochemistry Communications*, **11** 2157-2160 (2009).
7. M. Winter and J. O. Besenhard, *Electrochimica Acta*, **45** 31-50 (1999).
8. L. B. Freund and S. Suresh, *Thin Film Materials: Stress, Defect Formation and Surface Evolution*, Cambridge University Press (2009).
9. W. G. Moffatt, *The Handbook of Binary Phase Diagrams*, Schenectady, N.Y. (1978).
10. D. Larcher, L. Y. Beaulieu, D. D. MacNeil, and J. R. Dahn, *Journal of The Electrochemical Society*, **47** (5), 1658-1662 (2000).
11. M. D. Levi, E. Markevich, C. Wang, and D. Aurbach, *Journal of Electroanalytical Chemistry*, **600** (1), 13-22 (2007).
12. B. L. Boyce, L. N. Brewer, M. K. Neilsen, and M. J. Perricone, *Journal of Electronic Packaging*, **133** (3), 031009 (2011).
13. F. Pei and E. Chason, *Journal of Electronic Materials*, **43** (1), 80 (2014).
14. A. Tokranov, B. W. Sheldon, C. Li, S. Minne, and X. Xiao, *Applied Materials & Interfaces*, **6** (9), 6672-6686 (2014).
15. H. Tavassol, M. K. Y. Chan, M. G. Catarello, J. Greeley, D. G. Cahill, and A. A. Gewirth, *Journal of The Electrochemical Society*, **160** (6), A888-A896 (2013).
16. R. Hu, M. Zhu, H. Wang, J. Liu, O. Liuzhang, and J. Zou, *Acta Materialia*, **60** 4695-4703 (2012).

17. B. E. Deal and A. S. Grove, *Journal of Applied Physics*, **36** (12), 3770-3778 (1965).
18. J. Xie, N. Imanishi, A. Hirano, Y. Takeda, O. Yamamoto, X. B. Zhao, and G. S. Cao, *Solid State Ionics*, **181** 1611-1615 (2010).
19. K. I. Pridatko, *Russian Journal of Electrochemistry*, **42** (1), 63-70 (2005).
20. R. A. Huggins, *Journal of Power Sources*, **81-82** 13-19 (1999).
21. W. Xianming, T. Nishina, and I. Uchida, *Journal of Power Sources*, **104** (1), 90-96 (2002).
22. M. M. Nicholson, *Journal of The Electrochemical Society*, **121** (6), 734-738 (1974).
23. A. A. v. Zomeren, J.-H. Koegler, J. Schoonman, and P. J. v. d. Put, *Solid State Ionics*, **53-56** 333-338 (1992).

# Chapter 4.

## Numerical Solution of a Single Moving Boundary and Diffusion-induced Stress

As discussed in chapter 3, a transient high stress was observed at the beginning of the Sn-Li<sub>2</sub>Sn<sub>5</sub> phase transformation, which then rapidly decreased followed by the steady-state behavior (Fig. 4.1). Understanding the origin of this transient behavior and its implication for rate-dependent plastic deformation is the focus of this chapter.

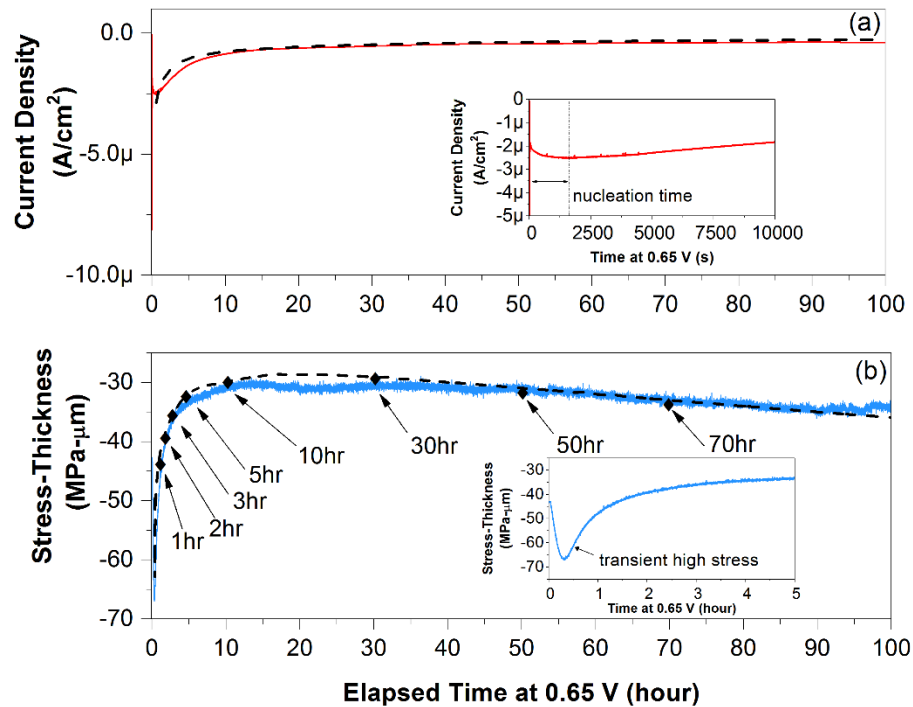


**Figure 4.1.** Measurements and calculation (dashed lines) during the potentiostatic lithiation experiments at 0.65 V. (a) current-density and inset showing the nucleation time; (b) stress-thickness and inset showing the transient high stress state.

Diffusion-induced stress has been studied previously in Li-ion battery research to understand mechanical failures of electrodes. Bower and Guduru<sup>1</sup> performed a finite element model of diffusion and plasticity in amorphous Si electrodes. Zhang et al.<sup>2</sup> studied graphite anodes with a layered structure. Christensen<sup>3</sup> presented a mathematical model of the particles in porous lithium manganese oxide cathodes and graphite-based anodes. These works primarily focused on the stress distribution in a single phase region with a concentration gradient. In contrast, the transient behavior in the experiments that are the subject of this work was observed at the beginning of the phase transformation where the phase boundary propagated along with diffusion in both the Sn and  $\text{Li}_2\text{Sn}_5$  layers. The resulting concentration profile and interface motion must be analyzed in terms of a moving boundary problem, a classical problem in solid state diffusion. A class of literature has been published on solving the moving boundary of the heat transfer problem, so called the Stefan problem.<sup>4-7</sup> In Li-ion battery research, phase transformations in crystalline-Si<sup>8</sup> electrode and cathode materials<sup>9</sup> have also been studied. For Sn electrodes, Hulikal et al.<sup>10</sup> have performed phase-field modeling on Li-Sn phase transformations.

The concentration in a moving boundary value problem does not have a simple analytical solution. Therefore, in this chapter we have performed a numerical solution to simulate the evolution of the phase boundary and Li concentration in the Sn and  $\text{Li}_2\text{Sn}_5$  layers during potentiostatic lithiation. At the same time, we use a model of diffusion-induced stress with rate-dependent plasticity and elastic unloading to analyze the corresponding curvature measurements. The simulated results are compared with the experiments to extract the relevant kinetic and mechanical parameters.

Here, we assume that during potentiostatic lithiation, the Li concentration at the surface is established by the applied potential and remains constant during the experiment.

The phase transformation is initiated by lowering the applied potential and then proceeds in two stages. In the first stage, the  $\text{Li}_2\text{Sn}_5$  phase nucleates and grows near the surface of the anode, resulting in a continuous layer. Subsequently, the  $\text{Sn}/\text{Li}_2\text{Sn}_5$  phase boundary propagates in the anode as the Sn layer is continuously transformed into the  $\text{Li}_2\text{Sn}_5$  phase. In the following sections, we discuss a continuum model for the Li concentration profile, layer stress and phase boundary propagation in the two stages.

## 4.1 Kinetic model of the nucleation stage

### 4.1.1 Characteristic in the current density during nucleation

In section 3.2.1, a feature in current density is seen at the beginning of  $\text{Sn-Li}_2\text{Sn}_5$  phase transformation; a large current density appears, then decreases quickly followed by a gradual increase. The re-increase in current density is related to the nucleation of the  $\text{Li}_2\text{Sn}_5$  phase at the surface.<sup>11</sup> Once the nuclei of  $\text{Li}_2\text{Sn}_5$  have grown to form a continuous layer, the phase boundary initiates and the current density starts to decay. The elapsed time between the moment of potential change and the starting of the exponential decay is considered as the nucleation time; it is shown in the inset of Fig. 4.1a.

### 4.1.2 Demonstration of nucleation time

A supporting experiment to show the effect of the nucleation period for the  $\text{Li}_2\text{Sn}_5$  phase is shown in Fig. 4.2. This experiment was carried on a  $1.85\ \mu\text{m}$  Sn film and the experimental condition is described as follow. First, the potential was held at 0.8 V for 20 hours to form the SEI before activating  $\text{Sn-Li}_2\text{Sn}_5$  phase transformation. Subsequently,

the potential was changed to 0.65 V for different intervals of time and then raised to 0.8 V, followed by an open circuit potential (OCP) measurement to obtain the equilibrium surface potential. The cycle (0.65 V-0.8 V-OCP) was repeated with increasing lengths of elapsed time  $\zeta$  at 0.65 V.

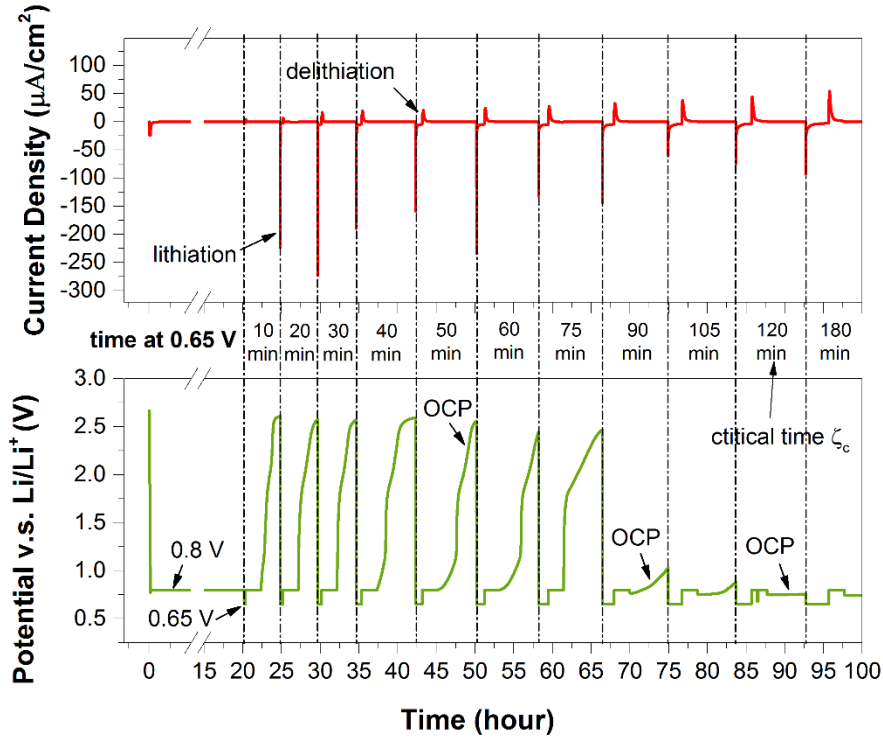


**Figure 4.2.** Experimental results underlying estimate of nucleation time of  $\text{Sn-Li}_2\text{Sn}_5$  phase transformation.

When the potential is held at 0.65 V, the sample lithiates as seen from the current density profile (Fig. 4.2). The most significant observation in this experiment, as shown in Fig. 4.2, is that for a hold time  $\zeta$  less than a critical time  $\zeta_c$ , the OCP evolves to around 2.7 V, which corresponds to the Sn phase, whereas for  $\zeta$  greater than  $\zeta_c$ , it evolves to a value below 1 V. During subsequent cycles, the OCP evolves to 0.76V, which is the equilibrium potential of  $\text{Li}_2\text{Sn}_5$  phase. Note that this transition in the open circuit

potential response takes place abruptly. We attribute this transition to the nucleation of the  $\text{Li}_2\text{Sn}_5$  phase from a supersaturated solid solution state. In this experiment, we found the critical time  $\zeta_c$  to be approximately 120 minutes. Although the critical time  $\zeta_c$  obtained from this experiment is not the same as seen in Fig. 4.1a, the difference in the experimental procedures (i.e., additional steps: delithiation and OCP in the supporting experiment) possibly disturb the nucleation kinetics and account for the discrepancy. The main conclusion from this supporting experiment is established that there is a finite nucleation time to begin formation of  $\text{Li}_2\text{Sn}_5$  phase.

#### *4.1.3 Analytical solution of Li concentration during nucleation*

As the applied potential is changed to a value below the threshold of the phase transformation, a higher Li concentration is established at the surface that activates the nucleation of the  $\text{Li}_2\text{Sn}_5$  phase ( $\beta$  phase). We assume the nucleation happens in a thin region near the surface of the anode. In the nucleation region (thickness of  $S_o$ ), the nuclei form and grow while some Li also diffuses into the Sn ( $\alpha$  phase). A schematic plot of the Li concentration is shown in Fig. 4.3.

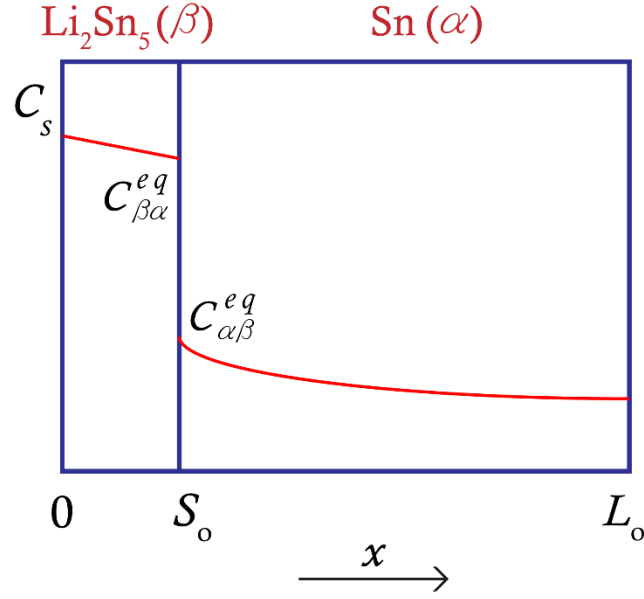


**Figure 4.3.** Schematic plot for initial nucleation stage of the numerical solutions.

The concentration of accumulated Li in the Sn phase during the nucleation period can be obtained by solving a 1-D diffusion equation. The Li concentration at the Sn/ $\text{Li}_2\text{Sn}_5$  phase boundary in the Sn phase ( $x = S_0$ ) is assumed to remain at the equilibrium concentration,  $C_{\alpha\beta}^{eq}$ , i.e., the Li solubility in Sn phase. The substrate is assumed to be impervious to Li.

The governing equation and boundary conditions for the diffusion in Sn are:

#### Governing Equation

$$\frac{\partial C_\alpha(x, t)}{\partial t} = D_\alpha \frac{\partial^2 C_\alpha(x, t)}{\partial x^2}, \text{ for Sn region, } S_0 \leq x \leq L_0 \quad \{4.1\}$$

## Boundary Conditions

$$C_\alpha(S_0, t) = C_{\alpha\beta}^{eq}; \frac{\partial C_\alpha(L_0, t)}{\partial x} = 0 \quad \{4.2\}$$

$L_0$  is the thickness of the Sn layer and  $D_\alpha$  is the Li diffusivity in Sn. Normalized forms of the position  $\xi = x/L_0$ , time  $\tau = D_\alpha t/L_0^2$ , and Li concentration  $\theta = (C_\alpha - C_{\alpha\beta}^{eq})/(C_i - C_{\alpha\beta}^{eq})$  are used in solving the equations, where  $C_i$  is the initial Li concentration in Sn. Note that  $\theta$  is defined such that it starts from a value of 1 and approaches 0 as  $C_\alpha$  reaches  $C_{\alpha\beta}^{eq}$ . The analytical solution of the concentration profile is

$$\theta(\xi, \tau) = \sum_{n=0}^{\infty} \frac{4}{(2n+1)\pi} \frac{\sin(2n+1)\pi\xi}{2} e^{-\frac{(2n+1)^2\pi^2}{4}\tau} \quad \{4.3\}$$

Eq. (4.3) provides the concentration profile of Li in Sn established during a given nucleation time  $t_0$ . The evolution of Li concentration in Sn during nucleation obtained by Eq. (4.3) is shown in Fig. 4.4.

For the profile inside the nucleation region ( $0 \leq x \leq S_0$ ), we assume that the Li diffusion is fast so the concentration at the phase boundary is at the equilibrium concentration  $C_{\beta\alpha}^{eq}$  i.e., the stoichiometric Li concentration of  $\text{Li}_2\text{Sn}_5$  phase. Therefore, a linear Li concentration profile is assumed with the surface concentration  $C_s$  and  $C_{\beta\alpha}^{eq}$  at the phase boundary. The concentration profile obtained at this stage is used as the initial Li concentration profile for the numerical solution in the second stage of modeling.

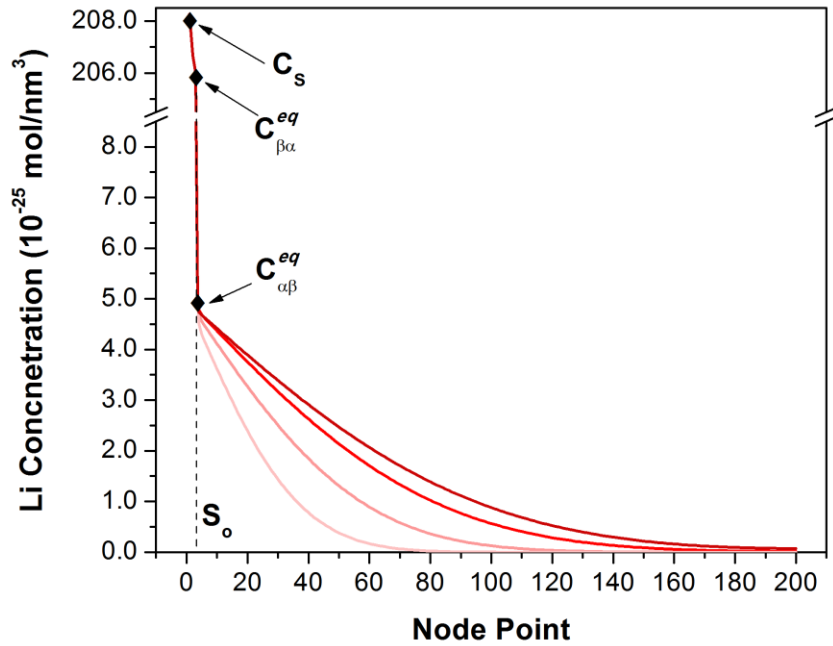


Figure 4.4. Calculated Li concentration for the initial profile of numerical simulations.

#### 4.2 Kinetic model for a single moving phase boundary

When the nucleation of the new phase is completed, the individual  $\text{Li}_2\text{Sn}_5$  nuclei coalesce to form a continuous layer at the surface of the anode. At this point, we assume there is a stable Sn/ $\text{Li}_2\text{Sn}_5$  phase boundary at  $x = S_0$ . Subsequently, many of the Li atoms that enter the electrode are consumed in advancing the phase boundary into the Sn layer by the growth of the lithiated phase. However, if the boundary does not move rapidly enough then there can be diffusion of excess Li into the Sn phase. On the other hand, if there is excess Li in the Sn layer (i.e., above the solubility limit) then it can also diffuse to the Sn/ $\text{Li}_2\text{Sn}_5$  interface and contribute to further  $\text{Li}_2\text{Sn}_5$  phase growth. Therefore, the kinetic model described here includes diffusion in both Sn and  $\text{Li}_2\text{Sn}_5$  layers and a moving phase boundary driven by fluxes of Li from both directions.

### 4.2.1 Governing equations

A schematic plot of the kinetic model is shown in Fig. 4.5. The range of  $x$  is defined as  $0 \leq x \leq L(t)$ , where  $x = 0$ , is the electrolyte/anode interface and  $x = L(t)$  is the anode/substrate interface. Note that  $L(t)$  is a function of time due to the volume expansion caused by the phase transformation. The anode is divided into two regions by the phase boundary; Sn ( $\alpha$  phase) for  $x \geq S(t)$  and  $\text{Li}_2\text{Sn}_5$  ( $\beta$  phase) for  $x \leq S(t)$ .

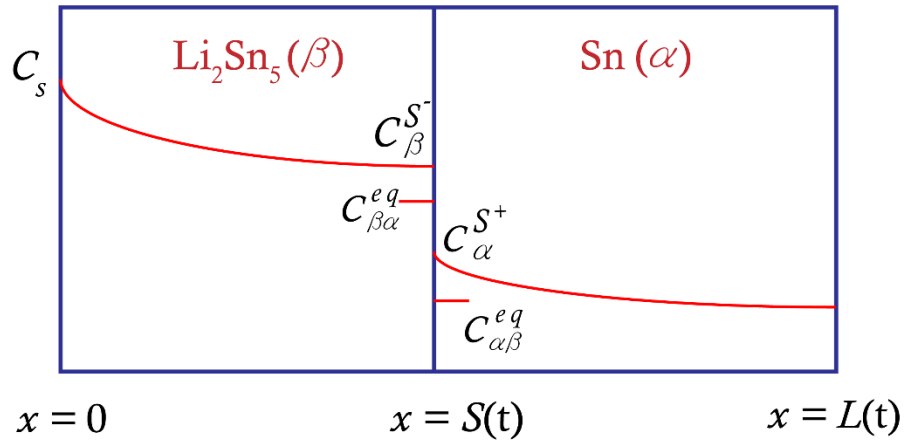


**Figure 4.5.** Schematic plot of the kinetic model of a single moving boundary.

The governing equations are presented as follow:

$$(g1) \frac{\partial c_{\beta}(x,t)}{\partial t} = D_{\beta} \frac{\partial^2 c_{\beta}(x,t)}{\partial x^2}, \text{ for } \text{Li}_2\text{Sn}_5 \text{ (}\beta \text{ phase) region, } 0 \leq x \leq S(t)$$

$$(g2) \frac{\partial c_{\alpha}(x,t)}{\partial t} = D_{\alpha} \frac{\partial^2 c_{\alpha}(x,t)}{\partial x^2}, \text{ for Sn (}\alpha \text{ phase) region, } S(t) \leq x \leq L(t)$$

$$(g3) D_{\beta} \frac{\partial c_{\beta}^{S-}}{\partial x} - D_{\alpha} \frac{\partial c_{\alpha}^{S+}}{\partial x} = (C_{\alpha}^{S+} - C_{\beta}^{S-})v_S$$

We assume that the time dependent diffusion of Li atoms in the two layers can be described by the Fick's second law as showing in governing equation (g1) and (g2).  $D_\alpha$  and  $D_\beta$  are the diffusion coefficients of Li in Sn and  $\text{Li}_2\text{Sn}_5$  respectively, and are assumed to be constants. The governing equation for the moving boundary, so called the Stephan condition, is represented in Eq. (g3).  $C_\alpha^{S+}$  and  $C_\beta^{S-}$  denote the Li concentrations at the Sn/ $\text{Li}_2\text{Sn}_5$  phase boundary in Sn phase and in  $\text{Li}_2\text{Sn}_5$  phase respectively.  $v_S$  is the velocity of the Sn/ $\text{Li}_2\text{Sn}_5$  phase boundary, and can be represented as  $v_S = \frac{dS(t)}{dt}$ . In governing equation (g3), it is seen that the Li fluxes difference at the interface is related to the movement of the phase boundary. Therefore, it is governing the mass conservation of Li at the interface.

#### 4.2.2 Boundary conditions

The boundary conditions are chose to agree with the experimental conditions. In this model, we neglect the effect of SEI on the electrochemical processes at the electrolyte/anode interface. The boundary conditions are presented as follow:

$$(b1) C_\beta(0, t) = C_s$$

$$(b2) \frac{\partial C_\alpha(L(t), t)}{\partial x} = 0$$

$$(b3) C_\alpha^{S+} = C_{\alpha\beta}^{eq} + (C_\beta^{S-} - C_{\beta\alpha}^{eq})$$

$$(b4) v_S = K_{\alpha\beta}(C_\beta^{S-} - C_{\beta\alpha}^{eq})$$

In boundary condition (b1), we assume that a constant cell potential under potentiostatic condition corresponds to a constant Li concentration  $C_S$  at  $x = 0$ . In boundary condition (b2), we assume the substrate to be impervious to Li, so the Li flux at the anode/substrate interface is set to zero. At equilibrium, the chemical potentials of Li atoms on both sides of the interface are the same, i.e.,  $\mu_{\alpha, Li}^{eq} = \mu_{\beta, Li}^{eq}$ , and the corresponding equilibrium concentrations are the Li solubility of the Sn phase  $C_{\alpha\beta}^{eq}$  and the stoichiometric concentration of the  $Li_2Sn_5$  phase  $C_{\beta\alpha}^{eq}$ .<sup>12</sup> During the phase boundary propagation, the actual chemical potentials on either side of the phase boundary are expected to deviate from the equilibrium values. In general, the chemical potential can be discontinuous across a moving phase boundary, although it is often assumed that they are equal in the literature.<sup>13</sup> Here, we allow them to be discontinuous with a drop of  $\Delta\mu$  across the interface.<sup>12</sup>

$$\Delta\mu = \mu_{\beta, Li} - \mu_{\alpha, Li} \quad \{4.4\}$$

where  $\mu_{\alpha, Li}$  and  $\mu_{\beta, Li}$  are the chemical potentials of Li on Sn and  $Li_2Sn_5$  sides of the interface respectively. The chemical potential difference can be represented as

$$\Delta\mu = \mu_{\beta, Li}^{eq} + kT \ln \varphi_{\beta} \delta C_{\beta, Li} - \mu_{\alpha, Li}^{eq} - kT \ln \varphi_{\alpha} \delta C_{\alpha, Li} \quad \{4.5\}$$

where  $\varphi_{\alpha}$  and  $\varphi_{\beta}$  are activity coefficients and the logarithmic terms include the deviations of the chemical potential from the equilibrium values ( $\delta C_{\alpha, Li} = C_{\alpha}^{S+} - C_{\alpha\beta}^{eq}$  and

$\delta C_{\beta, Li} = C_{\beta}^{S^-} - C_{\beta\alpha}^{eq}$ ). The equilibrium chemical potentials can be eliminated and by rearranging Eq. (4.5), the remaining terms lead to

$$\frac{\varphi_{\alpha}}{\varphi_{\beta}} \exp\left(\frac{\Delta\mu}{kT}\right) = \frac{\delta C_{\beta, Li}}{\delta C_{\alpha, Li}} = \frac{C_{\beta}^{S^-} - C_{\beta\alpha}^{eq}}{C_{\alpha}^{S^+} - C_{\alpha\beta}^{eq}} \quad \{4.6\}.$$

According to the Li-Sn phase diagram,<sup>14</sup> both the Sn and  $\text{Li}_2\text{Sn}_5$  phases have limited Li solubility, so we assume that the non-ideal behavior of Li in both phase are similar and the ratio of activity coefficients  $\frac{\varphi_{\alpha}}{\varphi_{\beta}}$  is close to 1. In addition, the chemical potential drop  $\Delta\mu$  at the interface is considered to be small by assuming the Li diffusion across the interface is fast and the interface is negligibly thin as used in the literature.<sup>15</sup> Therefore, we assume the product  $\frac{\varphi_{\alpha}}{\varphi_{\beta}} \exp\left(\frac{\Delta\mu}{kT}\right)$  is approximated to be 1, and Eq. (4.6) leads to the boundary condition (b3). The Li concentration in both layers are higher than the equilibrium values, which means that only the diffusion of excess Li atoms in Sn and  $\text{Li}_2\text{Sn}_5$  are considered here.

The deviation from the equilibrium state induces a supersaturation of Li at the phase boundary which is the driving force for the phase boundary movement as represented in boundary condition (b4).  $K_{\alpha\beta}$  is the reaction rate coefficient for the Sn- $\text{Li}_2\text{Sn}_5$  phase transformation, a measure of the mobility of the phase boundary. For larger values of  $K_{\alpha\beta}$ , the phase boundary propagates more rapidly for a specific value of the supersaturation. If  $K_{\alpha\beta} \rightarrow \infty$ , the phase boundary movement depends only on the diffusion in the layers, which is referred to as the diffusion-controlled case. In the limit where  $K_{\alpha\beta} \rightarrow 0$ , the phase

boundary movement is determined by the reaction rate of phase transformation at the interface, which is the interface-controlled case. In intermediate situations, the kinetics are ‘mixed.’ In the current kinetic picture, with a finite value of  $K_{\alpha\beta}$ , the phase propagation is determined by both diffusion in the phases and the reaction at the interface.

### 4.3 Finite-difference analysis

Moving boundary problems have been solved by a variety of methods in the literature.<sup>8, 16-23</sup> Here, we use the finite-difference method with a solution technique developed by Crank.<sup>17, 18</sup> This involves a front-tracking method with a fixed grid that spans the entire simulated domain. For the general nodal points, the usual finite-difference formulae can be used. For the points next to and at the phase boundary, since the moving boundary typically locates between two neighboring nodal points, the interpolation formulae of Lagrangian type is used to incorporate the unequal spacings between the moving boundary and the grid lines. In this section, we start with the original finite-difference formulae and then demonstrate the Lagrangian Interpolation presented in the book *Free and Moving Boundary Problems* by J. Crank.<sup>18</sup> Subsequently, the equations are modified for the kinetic model described in the preceding section.

#### 4.3.1 General finite-difference formulae

Here, the finite-difference method we used is based on the central difference in space and the forward Euler method in time. For a discretized concentration  $C_n^j$ , the subscript  $n$  and  $j$  denote the number of grid line and time step. The size of time step and spacing

between the grids are defined as  $\Delta t$  and  $\Delta x$  respectively. A stencil plot of this method is shown in Fig. 4.6.

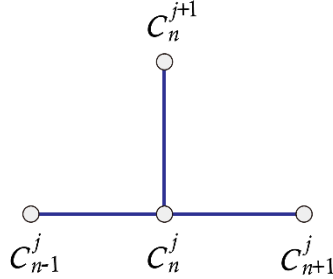


**Figure 4.6.** Stencil plot of finite-difference method utilized in the calculation.

The discretized form of the Fick's second law of diffusion is

$$\frac{C_n^{j+1} - C_n^j}{\Delta t} = D \frac{(C_{n-1}^j - 2C_n^j + C_{n+1}^j)}{\Delta x^2} \quad \{4.7\}$$

where  $D$  is the diffusion coefficient and Eq. (4.7) can be modified into

$$C_n^{j+1} = C_n^j + \frac{D\Delta t}{\Delta x^2} (C_{n-1}^j - 2C_n^j + C_{n+1}^j) \quad \{4.8\}.$$

Eq. (4.8) is the general form of the Forward-Time Central-Space method of finite-difference method. For the nodal points that have the equal spacing with the neighboring grids, it can be used to calculate the concentration of a node point at the next time step  $j+1$  with the concentrations of the neighboring nodes at time step  $j$ .

### 4.3.2 Lagrangian interpolation

For the points next to the phase boundary, the distances between the nodal points are smaller than the usual grid spacing  $\Delta x$ . Therefore, the Lagrangian interpolation is performed to account for the change of spacing. The three-point formula of Lagrangian interpolation [Crank 1957a] for a general function  $f(x)$  is given as:

$$f(x) = \sum_{n=0}^2 \ell_n(x) f(a_n) \quad \{4.9\}$$

where  $\ell_n(x) = \frac{p_2(x)}{(x-a_j)p_2'(a_j)}$  ;  $p_2(x) = (x - a_0)(x - a_1)(x - a_2)$  , and  $p_2'(x)$  is the derivative with respect to  $x$  at  $x = a_n$ .  $f(a_0), f(a_1), f(a_2)$  are the known values at the three points at  $x = a_0, a_1, a_2$  respectively. The derivative of  $f(x)$  then can be represented as

$$\frac{df}{dx} = \ell_0'(x)f(a_0) + \ell_1'(x)f(a_1) + \ell_2'(x)f(a_2) \quad \{4.10\}$$

$$\text{where } \ell_0'(x) = \frac{(x-a_1)+(x-a_2)}{(a_0-a_1)(a_0-a_2)}, \ell_1'(x) = \frac{(x-a_0)+(x-a_2)}{(a_1-a_0)(a_1-a_2)}, \ell_2'(x) = \frac{(x-a_0)+(x-a_1)}{(a_2-a_0)(a_2-a_1)}.$$

Furthermore, the second derivative of  $f(x)$  is

$$\frac{1}{2} \frac{d^2 f}{dx^2} = \frac{f(a_0)}{(a_0 - a_1)(a_0 - a_2)} + \frac{f(a_1)}{(a_1 - a_2)(a_1 - a_0)} + \frac{f(a_2)}{(a_2 - a_0)(a_2 - a_1)} \quad \{4.11\}$$

A schematic plot of a fixed grid with a moving boundary at a given time step  $j$  is showing in Fig. 4.7.  $\Delta x_\alpha$  and  $\Delta x_\beta$  are the grid spacing of  $\alpha$  and  $\beta$  phases respectively. The different in grid spacing can account for the volume expansion induced by the phase transformation. The boundary is located at a fraction distance  $P^j \Delta x_\beta$  between the two grid lines at  $i$  and  $i+1$  nodes.  $P^j$  is the progression factor indicating the position of phase boundary in the present  $i+1$  interval which has a value between 0 and 1. The discretized boundary position at time step  $j$  is

$$S^j = (i + P^j) \Delta x_\beta \quad \{4.12\}$$

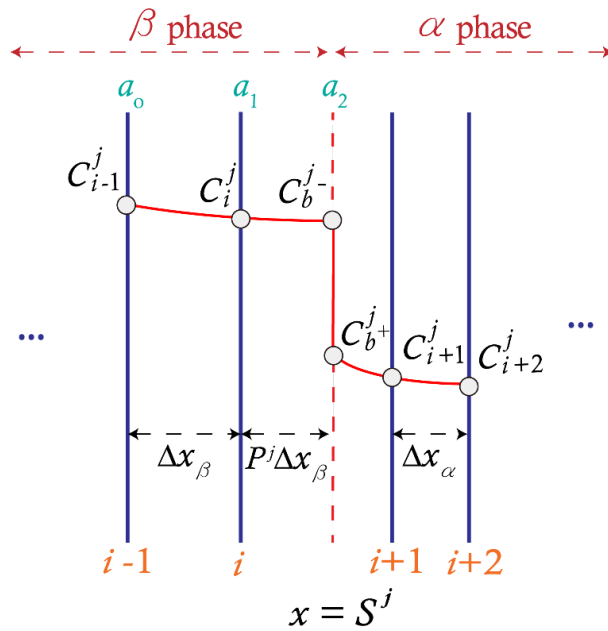


**Figure 4.7.** Schematic plot of the Lagrangian interpolation method near the phase boundary.

If we define the points  $a_0, a_1, a_2$  in the Lagrangian formulae with the grid lines located at  $(i - 1)\Delta x_\beta, i\Delta x_\beta$ , and the moving boundary  $S^j$  in the  $\beta$  phase. The values  $f(a_0), f(a_1), f(a_2)$  then correspond to  $C_{i-1}^j, C_i^j, C_{b-}^j$  respectively. Note that the concentration at the phase boundary has different values in  $\alpha$  and  $\beta$  phases, and  $C_{b-}^j$  is the one in  $\beta$  phase. By applying Eq. (4.10) and (4.11) to the  $\beta$  phase region,  $x \leq S^j$ , we have

$$\frac{\partial C}{\partial x} = \frac{1}{\Delta x_\beta} \left( \frac{P^j}{P^j+1} C_{i-1}^j - \frac{(P^j+1)}{P^j} C_i^j + \frac{(2P^j+1)}{P^j(P^j+1)} C_{b-}^j \right), \text{ for } x = S^j = (i + P^j)\Delta x_\beta \quad \{4.13\}$$

and

$$\frac{\partial^2 C}{\partial x^2} = \frac{2}{\Delta x_\beta^2} \left( \frac{C_{i-1}^j}{P^j+1} - \frac{C_i^j}{P^j} + \frac{C_{b-}^j}{P^j(P^j+1)} \right), \text{ for } x = i\Delta x_\beta \quad \{4.14\}.$$

Similarly, we can redefine the points  $a_0, a_1, a_2$  to the grid lines located at the moving boundary at  $S^j, S^j + (1 - P^j)\Delta x_\alpha, S^j + (2 - P^j)\Delta x_\alpha$ , in the  $\alpha$  phase. Then the values  $f(a_0), f(a_1), f(a_2)$  correspond to  $C_{b+}^j, C_{i+1}^j, C_{i+2}^j$ , respectively. Here,  $C_{b+}^j$  is the concentration at the phase boundary in the  $\alpha$  phase. Therefore, Eq. (4.10) and (4.11) can be used for the derivatives in the  $\alpha$  phase region,  $x \geq S(t)$ , and give

$$\frac{\partial C}{\partial x} = \frac{1}{\Delta x_\alpha} \left( \frac{2P^j-3}{(1-P^j)(2-P^j)} C_{b+}^j + \frac{(2-P^j)}{(1-P^j)} C_{i+1}^j - \frac{(1-P^j)}{(2-P^j)} C_{i+2}^j \right), \text{ for } x = S_1^j \quad \{4.15\}$$

and

$$\frac{\partial^2 C}{\partial x^2} = \frac{2}{\Delta x_\alpha^2} \left( \frac{C_b^{j+}}{(1-P^j)(2-P^j)} - \frac{C_{i+1}^j}{(1-P^j)} + \frac{C_{i+2}^j}{(2-P^j)} \right), \text{ for } x = S^j + (1 - P^j)\Delta x_\alpha \quad \{4.16\}.$$

These results (Eqs. 4.13-16) can be used to get the discretized form of diffusion equation for the nodal points near the phase boundary in  $\alpha$  and  $\beta$  phases, and the further formulation is discussed in the following section.

### 4.3.3 Calculation procedure

The entire simulated domain is subdivided into  $M$  intervals. The mesh size in the Sn region is  $\Delta x_\alpha = L_o/M$ , and the mesh size in the  $\text{Li}_2\text{Sn}_5$  phase is  $\Delta x_\beta = r\Delta x_\alpha$ , where  $r$  is the volume expansion ratio due to the phase change.  $r$  has a value of 1.22 for the Sn- $\text{Li}_2\text{Sn}_5$  phase transformation. The finite-difference grid used in the solution is shown in Fig. 4.8.

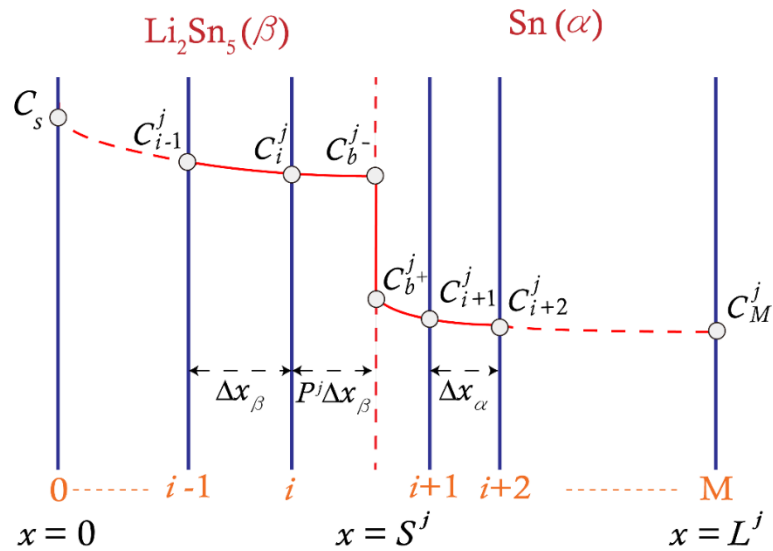


**Figure 4.8.** Schematic plot of the finite-difference framework with a single moving boundary.

The simulation of the moving boundary starts with the initial Li concentration profile (Fig. 4.4) set to be the value calculated at the end of the nucleation period. In the numerical calculation, for a given time step  $j$ , the phase boundary  $S^j$  locates within the  $i+1$  interval, which is between nodal points  $i$  and  $i+1$ . As the phase boundary propagate across the grids, the  $i$  and  $i+1$  nodes will be updated accordingly. As seen in Eq. (4.8), the discretized form of the Fick's second law of diffusion used in the governing equations (g1) and (g2) can be represented as

$$C_n^{j+1} = C_n^j + \frac{D_k \Delta t}{\Delta x_k^2} (C_{n-1}^j - 2C_n^j + C_{n+1}^j) \quad \{4.17\}$$

where  $k$  denotes the phase ( $\alpha$  or  $\beta$ ). For most of the nodal points, Eq. (4.17) can be used to calculate the Li concentration of a node at the next time step  $j+1$  with the concentrations of the nearby nodes at time step  $j$ . The exceptions are the nodes at the electrolyte/anode interface, at the anode/substrate interface and the ones next to the moving phase boundary. For these nodes, the calculations are discussed below. In addition, since the phase boundary generally not locates on a nodal point, the concentrations at the phase boundary need to be obtained separately as well.

The surface concentration is assumed to be a constant during the potentiostatic lithiation (boundary condition b1) so that  $C_S$  is a constant. The concentration of the node at anode/substrate interface is governed by boundary condition (b2). The condition is fulfilled by applying  $C_{M-1}^j = C_{M+1}^j$ , so Eq. (4.8) is modified to be

$$C_M^{j+1} = C_M^j + \frac{2D_\alpha \Delta t}{\Delta x_\alpha^2} (C_{M-1}^j - C_M^j) \quad \{4.18\}.$$

For the  $i$  node next to the phase boundary in the  $\beta$  phase ( $\text{Li}_2\text{Sn}_5$ ), the Lagrangian interpolation showing in Eq. (4.14) can be used to state the Fick's second law as

$$C_i^{j+1} = C_i^j + \frac{2D_\beta \Delta t}{\Delta x_\beta^2} \left( \frac{C_{i-1}^j}{P^j + 1} - \frac{C_i^j}{P^j} + \frac{C_{b^-}^j}{P^j(P^j + 1)} \right) \quad \{4.19\}$$

where  $C_{b^-}^j$  is the Li concentration at the phase boundary in  $\beta$  phase. Similarly, by using Eq. (4.16), the concentration at the  $i+1$  node in the  $\alpha$  phase (Sn) is

$$C_{i+1}^{j+1} = C_{i+1}^j + \frac{2D_\alpha \Delta t}{\Delta x_\alpha^2} \left( \frac{C_{b^+}^j}{(1 - P^j)(2 - P^j)} - \frac{C_{i+1}^j}{1 - P^j} + \frac{C_{i+2}^j}{2 - P^j} \right) \quad \{4.20\}$$

where  $C_{b^+}^j$  is the Li concentration at the phase boundary in  $\alpha$  phase.

Following the same approach, the discretized form of the governing equation (g3) can be obtained with the fluxes at the phase boundary showing in Eq. (4.13) and (4.15), and the representation of the phase boundary position in Eq. (4.12):

$$\begin{aligned}
& D_\beta \left[ \frac{1}{\Delta x_\beta} \left( \frac{P^j C_{i-1}^j}{P^{j+1}} - \frac{(P^{j+1}) C_i^j}{P^j} + \frac{(2P^{j+1}) C_{b-}^j}{P^j(P^{j+1})} \right) \right] \dots \\
& - D_\alpha \left[ \frac{1}{\Delta x_\alpha} \left( \frac{(2P^j-3) C_{b+}^j}{(1-P^j)(2-P^j)} + \frac{(2-P^j) C_{i+1}^j}{1-P^j} - \frac{(1-P^j) C_{i+2}^j}{2-P^j} \right) \right] = (C_{b+}^j - C_{b-}^j) v_S \quad \{4.21\}.
\end{aligned}$$

As seen in the boundary condition (b3), the concentration difference across the phase boundary  $(C_{b+}^j - C_{b-}^j)$  can be substituted with the difference in equilibrium concentration  $(C_{\alpha\beta}^{eq} - C_{\beta\alpha}^{eq})$ . The velocity of the phase boundary  $v_S$  can be substituted with  $K_{\alpha\beta} (C_{b-}^j - C_{\beta\alpha}^{eq})$  as described in the boundary condition (b4). Therefore, Eq. (4.21) can be rearranged in to a representation of  $C_{b-}^j$  as

$$\begin{aligned}
C_{b-}^j = & \\
& \frac{\frac{D_\beta \left[ \frac{P^j C_{i-1}^j}{P^{j+1}} - \frac{(P^{j+1}) C_i^j}{P^j} \right] - \frac{D_\alpha \left[ \frac{(2P^j-3)(C_{\alpha\beta}^{eq} - C_{\beta\alpha}^{eq})}{(1-P^j)(2-P^j)} + \frac{(2-P^j) C_{i+1}^j}{1-P^j} - \frac{(1-P^j) C_{i+2}^j}{2-P^j} \right]}{\Delta x_\alpha} + K_{\alpha\beta} C_{\beta\alpha}^{eq} (C_{\alpha\beta}^{eq} - C_{\beta\alpha}^{eq})}{\frac{D_\alpha \left[ \frac{(2P^j-3)}{(1-P^j)(2-P^j)} \right] - \frac{D_\beta \left[ \frac{(2P^j+1)}{P^j(P^{j+1})} \right]}{\Delta x_\beta} + K_{\alpha\beta} (C_{\alpha\beta}^{eq} - C_{\beta\alpha}^{eq})}} \quad \{4.22\}.
\end{aligned}$$

It is seen that the terms in Eq. (4.22) are all at the same time step  $j$ . It can be used to solve the concentration at the phase boundary  $C_{b-}^j$  that can fulfill boundary condition at the interface with the other determined concentrations at the nearby nodes, i.e.,  $i-1$ ,  $i$ ,  $i+1$  and  $i+2$  nodes. Thus, Eq. (4.22) can be modified for to calculate  $C_{b-}^{j+1}$  if all the concentration at the nodes near the new position of the phase boundary at the next step  $j+1$  are known.

$C_{b-}^{j+1}$  can be represented as:

$$C_{b^-}^{j+1} =$$

$$\frac{\frac{D_\beta}{\Delta x_\beta} \left[ \frac{P^{j+1} C_{i-1}^{j+1}}{P^{j+1+1}} - \frac{(P^{j+1+1}) C_i^{j+1}}{P^{j+1}} \right] - \frac{D_\alpha}{\Delta x_\alpha} \left[ \frac{(2P^{j+1}-3)(C_{\alpha\beta}^{eq} - C_{\beta\alpha}^{eq})}{(1-P^{j+1})(2-P^{j+1})} + \frac{(2-P^{j+1}) C_{i+1}^{j+1}}{1-P^{j+1}} - \frac{(1-P^{j+1}) C_{i+2}^{j+1}}{2-P^{j+1}} \right] + K_{\alpha\beta} C_{\beta\alpha}^{eq} (C_{\alpha\beta}^{eq} - C_{\beta\alpha}^{eq})}{\frac{D_\alpha}{\Delta x_\alpha} \left[ \frac{(2P^{j+1}-3)}{(1-P^{j+1})(2-P^{j+1})} \right] - \frac{D_\beta}{\Delta x_\beta} \left[ \frac{(2P^{j+1+1})}{P^{j+1}(P^{j+1+1})} \right] + K_{\alpha\beta} (C_{\alpha\beta}^{eq} - C_{\beta\alpha}^{eq})}$$

{4.23}

where the progression factor in the next time step  $j+1$  is

$$P^{j+1} = P^j + \frac{\Delta t}{\Delta x_\beta} K_{\alpha\beta} (C_{b^-}^j - C_{\beta\alpha}^{eq}) \quad \{4.24\}.$$

When  $P^{j+1} < 1$ , the new phase boundary is still located in the current interval. A complete concentration profile can be obtained by applying Eqs. (4.17), (4.18), (4.19), (4.20), (4.24) and (4.23) sequentially. On the other hand, if  $P^{j+1} > 1$ , the phase boundary will move into the next interval at the next time step  $j+1$ , and the  $i$  and  $i+1$  nodes have to be re-defined, i.e.,  $i^{j+1} = i^j + 1$ . In this case, the concentration at the regular nodes can still be calculated by Eq. (4.17). However, the Eq. (4.18) and (4.19) need to be modified to account for the migration of the phase boundary into the next grid interval. The concentration at nodes  $i$  and  $i+1$  are updated by Lagrangian interpolation (Eq. 4.9) according to

$$C_i^{j+1} = \frac{-P^{j+1}}{2 + P^{j+1}} C_{i-2}^{j+1} + \frac{2P^{j+1}}{1 + P^{j+1}} C_{i-1}^{j+1} + \frac{2}{(2 + P^{j+1})(1 + P^{j+1})} C_{b^-}^{j+1} \quad \{4.25\}$$

and

$$C_{i+1}^{j+1} = \frac{2}{(P^{j+1}-2)(P^{j+1}-3)} C_{b^+}^{j+1} + \frac{2-2P^{j+1}}{2-P^{j+1}} C_{i+2}^{j+1} + \frac{P^{j+1}-1}{3-P^{j+1}} C_{i+3}^{j+1} \quad \{4.26\}$$

which are substituted in Eq. (4.24). A new form of  $C_{b^-}^{j+1}$  can be obtained and represented as

$$C_{b^-}^{j+1} = \frac{\frac{D_\beta}{\Delta x_\beta} \left[ \frac{(P^{j+1}+1)C_{i-2}^{j+1} - (P^{j+1}+2)C_{i-1}^{j+1}}{P^{j+1}+2} - \frac{D_\alpha}{\Delta x_\alpha} \left[ \frac{(2P^{j+1}-3)(C_{\alpha\beta}^{eq} - C_{\beta\alpha}^{eq})}{(1-P^{j+1})(2-P^{j+1})} + \frac{2(C_{\alpha\beta}^{eq} - C_{\beta\alpha}^{eq})}{(1-P^{j+1})(3-P^{j+1})} \dots \right] + K_{\alpha\beta} C_{\beta\alpha}^{eq} (C_{\alpha\beta}^{eq} - C_{\beta\alpha}^{eq}) \right]}{\frac{D_\alpha}{\Delta x_\alpha} \left[ \frac{(2P^{j+1}-3)}{(1-P^{j+1})(2-P^{j+1})} + \frac{2}{(1-P^{j+1})(3-P^{j+1})} \right] - \frac{D_\beta}{\Delta x_\beta} \left[ \frac{(2P^{j+1}+1)}{P^{j+1}(P^{j+1}+1)} - \frac{2}{P^{j+1}(P^{j+1}+2)} \right] + K_{\alpha\beta} (C_{\alpha\beta}^{eq} - C_{\beta\alpha}^{eq})} \quad \{4.27\}.$$

Lastly, the progression factor is updated as  $P^{j+1'} = P^{j+1} - 1$  and then Eqs. (4.25) and (4.26) are used to get  $C_i^{j+1}$  and  $C_{i+1}^{j+1}$  and complete the concentration profile in the new time step  $j+1$ .

#### 4.3.4 Validation of the finite-difference modeling

To validate the finite-difference calculation, we compare the phase boundary evolution obtained by the numerical analysis with an analytical solution for the diffusion-controlled case of a semi-infinite film provided by R. F. Sekerka and S.-L. Wang in a chapter of the book Lectures of the Theory of Phase Transformations by H. Aaronson. The solution was developed from the typical form of error function for the infinite spatial domain. To modify the solution for semi-infinite case, the surface is treated as another interface. Therefore, in this analytical solution, there are two moving interfaces. One is

phase boundary  $\xi_1$  between  $\alpha$  and  $\beta$  phases; another is the surface  $\xi_2$ . The difference between  $\xi_1$  and  $\xi_2$  is the thickness of the  $\beta$  phase  $S^{Analyt}$  that forms:

$$S^{Analyt} = \left[ \left( \frac{Q^\beta R^{\beta 1} + R^{\beta 2}}{2} \right)^{1/2} - \frac{1}{2} \frac{1}{\sqrt{\pi}} \sqrt{\frac{D_\alpha}{D_\beta}} Q^\alpha R^\alpha \right] (4D_\beta t)^{1/2} \quad \{4.28\}$$

where  $Q$  and  $R$  are combinations of material constants as shown below:

$$R^\alpha = \frac{c_B^{\alpha\beta} - c_B^{\alpha\infty}}{c_B^{\beta\alpha} - c_B^{\alpha\beta}}, \quad R^{\beta 1} = \frac{c_B^{\beta\xi} - c_B^{\beta\alpha}}{c_B^{\beta\alpha} - c_B^{\alpha\beta}}, \quad R^{\beta 2} = \frac{\bar{V}_B^\beta (c_B^{\beta\xi} - c_B^{\beta\alpha})}{1 - \bar{V}_B^\beta c_B^{\beta\xi}}$$

$$Q^\alpha = \frac{1}{\bar{V}_A^\alpha \Delta}, \quad Q^\beta = \frac{\bar{V}_A^\beta c_A^{\alpha\beta} + \bar{V}_B^\beta c_B^{\alpha\beta}}{\bar{V}_B^\beta \Delta}, \quad \Delta = \frac{c_B^{\beta\alpha} c_A^{\alpha\beta} - c_B^{\alpha\beta} c_A^{\beta\alpha}}{c_B^{\beta\alpha} - c_B^{\alpha\beta}}$$

For the case discussed here,  $\alpha$  phase is Sn;  $\beta$  phase is  $\text{Li}_2\text{Sn}_5$  phase, and element A is Sn atom; element B is Li atom.  $\bar{V}$  terms are partial molar volumes, and the values are estimated by considering linear volume expansion between phases. The values of parameters used for the calculation in this section is presented in Table 4.1.

As mentioned above, the phase propagation in the kinetic model is controlled by both diffusion and reaction happening at the phase boundary. Simulation results for the thickness of the  $\beta$  phase for several values of  $\kappa$  and the analytical solution for diffusion-controlled growth are shown in Fig. 4.9.  $\kappa$  is the normalized reaction rate coefficient and is represented as

$$\kappa = \frac{K_{\alpha\beta}}{K_o} \quad \text{where} \quad K_o = \frac{D_\beta}{(c_{\beta\alpha}^{eq} - c_{\alpha\beta}^{eq})L_o} \quad \{4.29\}$$

**Table 4.1.** Parameters used in the demonstration in Fig. 4.9

Assigned Li diffusivity in Sn phase, $D_\alpha$	$3 \times 10^{-13}$ cm <sup>2</sup> /s
Assigned Li diffusivity in Li <sub>2</sub> Sn <sub>5</sub> phase, $D_\beta$	$4 \times 10^{-13}$ cm <sup>2</sup> /s
Li concentration at the surface in Li <sub>2</sub> Sn <sub>5</sub> phase, $C_B^{\beta\xi}$	$2.0826 \times 10^{-23}$ mol/nm <sup>3</sup>
Li concentration at the interface in Li <sub>2</sub> Sn <sub>5</sub> phase, $C_B^{\beta\alpha}$	$2.0590 \times 10^{-23}$ mol/nm <sup>3</sup> *
Li concentration at the interface in Sn phase, $C_B^{\alpha\beta}$	$5.0 \times 10^{-25}$ mol/nm <sup>3</sup>
Li concentration at infinity in Sn phase, $C_B^{\alpha\infty}$	0 mol/nm <sup>3</sup>
Sn concentration at the interface in Li <sub>2</sub> Sn <sub>5</sub> phase, $C_A^{\beta\alpha}$	$5.1475 \times 10^{-23}$ mol/nm <sup>3</sup> *
Sn concentration at the interface in Sn phase, $C_A^{\alpha\beta}$	$6.1410 \times 10^{-23}$ mol/nm <sup>3</sup> *
Partial molar volume of Sn in Sn phase, $\bar{V}_A^\alpha$	$1.63 \times 10^{22}$ nm <sup>3</sup> /mol *
Partial molar volume of Sn in Li <sub>2</sub> Sn <sub>5</sub> phase, $\bar{V}_A^\beta$	$1.67 \times 10^{22}$ nm <sup>3</sup> /mol *
Partial molar volume of Li in Li <sub>2</sub> Sn <sub>5</sub> phase, $\bar{V}_B^\beta$	$7.92 \times 10^{21}$ nm <sup>3</sup> /mol *

\*value calculated from the theoretical densities reported in Ref. 24

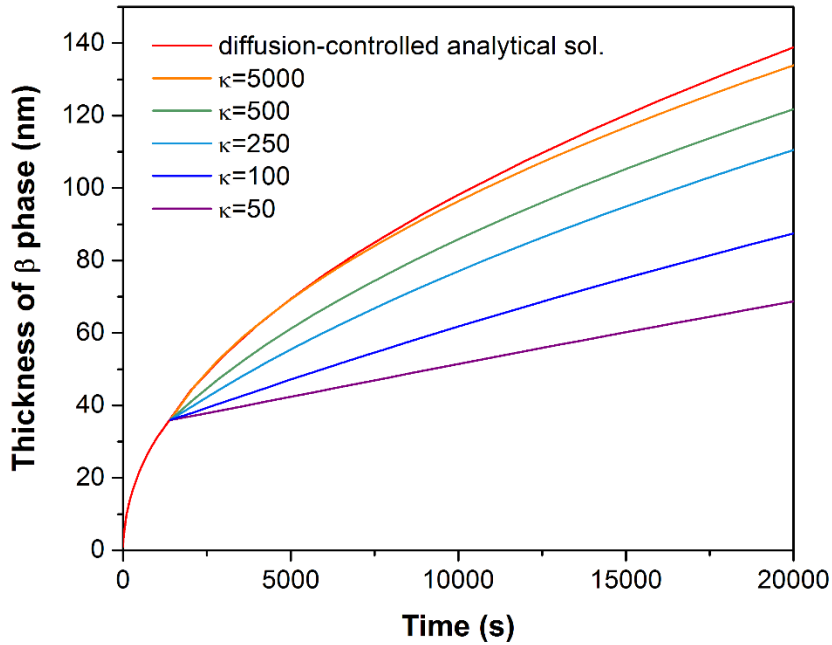


**Figure 4.9.** Comparison of the analytical solution for the semi-infinite diffusion-controlled case and numerical solution for a 9.25  $\mu\text{m}$  film with different values of normalized reaction rate coefficient  $\kappa$ .

In order to compare with the semi-infinite analytical solution, we consider a system with a large value of thickness of  $\alpha$  phase (9.25  $\mu\text{m}$ ) compared to the thickness of the  $\beta$  phase ( $< 150$  nm). Note that the numerical solution starts with a finite thickness of the  $\beta$  phase equal to 40 nm as seen in Fig. 4.9. In the simulation results, the reaction rate is controlled by the value of  $\kappa$ . Increasing  $\kappa$  changes the behavior of the phase boundary from interface-controlled to diffusion-controlled and the evolution of the  $\beta$  phase thickness changes from linear to parabolic with time. For large values of  $\kappa$  the numerical solution approaches the analytical result since the diffusion-controlled case corresponds to the limit of large reaction rate.

#### 4.3.5 Calibration with experiments

In section 4.1.1, we discussed a characteristic current density profile (inset of Fig. 4.1a) at the beginning of potentiostatic lithiation and considered the feature was due to the nucleation of the new phase. The elapsed time between the moment of potential change and the starting of the exponential decay is considered as the nucleation time, which was found to be approximately 1400 s in the experiment (Fig. 4.1a). The initial thickness of the lithiated phase  $S_0$  was estimated from the charge input during the nucleation time to be approximately 35 nm. According to the Li-Sn phase diagram, Li has very small solubility in Sn, below what can be measured reliably. However, the model requires the solubility as a parameter. The Li solubility in Sn phase  $C_{\alpha\beta}^{eq}$  is assumed to be  $5.0 \times 10^{-25}$  mol/nm<sup>3</sup> ( $\sim 0.01$  Li atom per each Sn atom). The value has been used as one of the fitting parameters to get good agreement between the model and the experiments. These values are used in Eq. (4.3) to obtain the initial Li concentration profile in Sn phase.

For the initial Li concentration in  $\text{Li}_2\text{Sn}_5$  phase, a linear profile with the surface concentration  $C_S$  and  $C_{\beta\alpha}^{eq}$  is considered. These results are utilized as the starting point of the finite-difference analysis.

The kinetic parameters ( $D_\alpha$ ,  $D_\beta$  and  $K_{\alpha\beta}$ ) are determined by using non-linear least square fitting to minimize the difference between the calculated Li flux and the measured current density. The calculation procedures of finite-difference analysis is described in section 4.3.3. The resulting fit is shown in Fig. 4.1a. The  $C_S$  value was determined experimentally by performing a potentiostatic intermittent titration technique (PITT) experiment on a fully transformed  $\text{Li}_2\text{Sn}_5$  layer (Fig. 3.8); details are provided in the section 3.2.3. The parameters used in the simulation are provided in Table 4.2, and the results of fitting parameters are presented in Table 4.3.

**Table 4.2.** Parameters used in the calculation for comparison with experiments

Initial thickness of anode, $L_0$	1850 nm
Number of node point, $M$	200
Grid spacing of Sn phase, $\Delta x_\alpha$	9.25 nm
Grid spacing of $\text{Li}_2\text{Sn}_5$ phase, $\Delta x_\beta$	11.285 nm
Volume expansion ratio of Sn- $\text{Li}_2\text{Sn}_5$ phase transformation, $r$	1.22
Size of time step in simulation, $\Delta t$	0.072 s
Nucleation time of Sn- $\text{Li}_2\text{Sn}_5$ phase transformation, $t_0$	1400 s
Thickness of nucleation region, $S_0$	35 nm
Initial Li concentration in Sn phase, $C_i$	0 mol/nm <sup>3</sup>
Stoichiometric Li concentration of $\text{Li}_2\text{Sn}_5$ phase (Equilibrium Li concentration in $\text{Li}_2\text{Sn}_5$ phase, $C_{\beta\alpha}^{eq}$ )	$2.0590 \times 10^{-23}$ mol/nm <sup>3</sup> (i.e., 0.4 Li atom per Sn atom)
Surface Li concentration in $\text{Li}_2\text{Sn}_5$ phase, $C_S$	$2.0826 \times 10^{-23}$ mol/nm <sup>3</sup>

**Table 4.3.** Material parameters obtained by current density fitting in Fig. 4.1a

Li solubility of Sn phase	$5.0 \times 10^{-25}$ mol/nm <sup>3</sup>
(Equilibrium Li concentration in Sn phase, $C_{\alpha\beta}^{eq}$ )	(i.e., ~0.01 Li atom per Sn atom)
Li diffusivity in Sn phase, $D_{\alpha}$	$2.1 \times 10^{-12}$ cm <sup>2</sup> /s
Li diffusivity in Li <sub>2</sub> Sn <sub>5</sub> phase, $D_{\beta}$	$1.4 \times 10^{-12}$ cm <sup>2</sup> /s
Reaction rate coefficient of Sn-Li <sub>2</sub> Sn <sub>5</sub> phase transformation, $K_{\alpha\beta}$	$4.0 \times 10^{-6}$ cm <sup>4</sup> /mol s

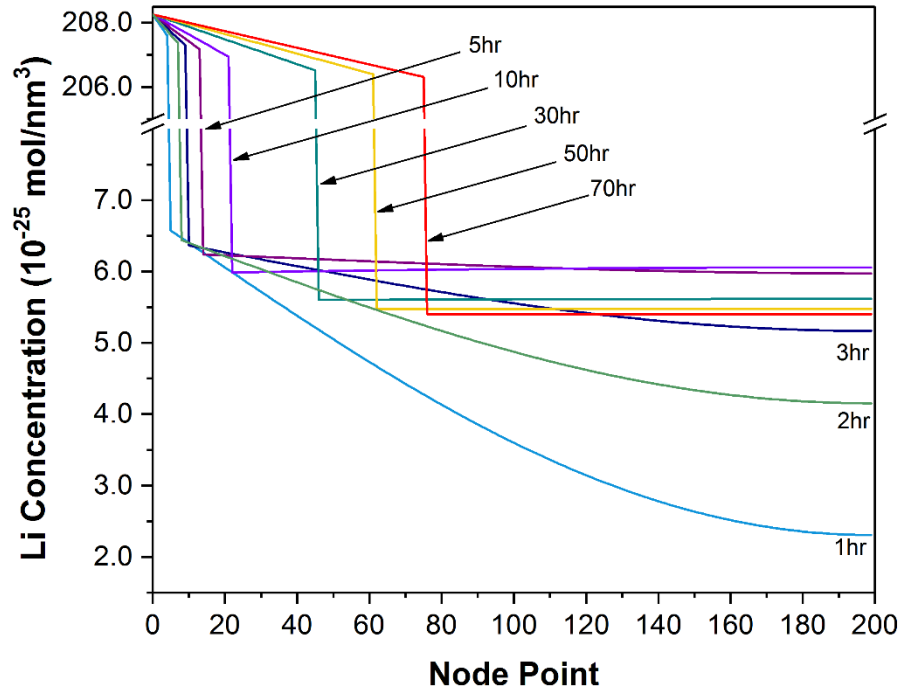


**Figure 4.10.** The calculated evolution of the Li concentration profile during the potentiostatic lithiation at 0.65 V.

Evolution of the simulated concentration profiles at different times are shown in Fig. 4.10. The sharp discontinuity in the concentration profiles indicates the evolving phase boundary position. The local Li concentration near the phase boundary in Li<sub>2</sub>Sn<sub>5</sub> and Sn

phases are shown in Fig. 4.11a and 4.11b respectively. The Li concentration in both phases are higher than the equilibrium concentrations. It is seen that the concentrations at the phase boundary approach to the equilibrium concentrations with progression of the phase boundary. Since the phase boundary velocity is determined by the supersaturation of Li at the phase boundary in  $\text{Li}_2\text{Sn}_5$  phase (boundary condition b4), the decrease of the supersaturation leads to the slowing down of the phase boundary. Fig. 4.11a shows that the progression of the phase boundary position in each 10 hour interval becomes smaller for longer times of lithiation.

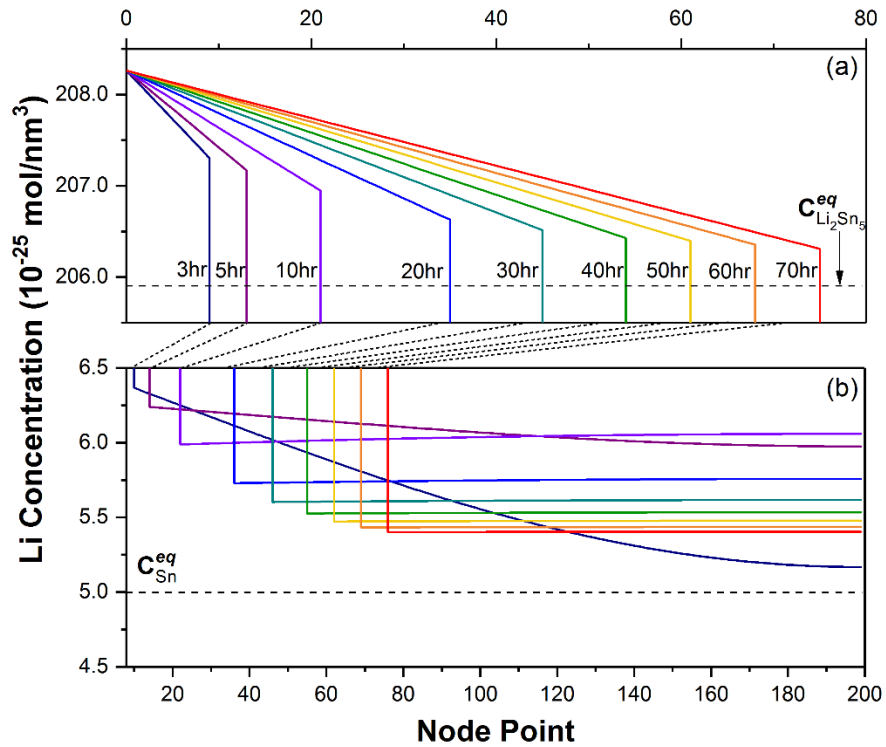


**Figure 4.11.** The calculated evolution of Li concentration profile near the phase boundary: (a) in the  $\text{Li}_2\text{Sn}_5$  phase, (b) in the Sn phase.

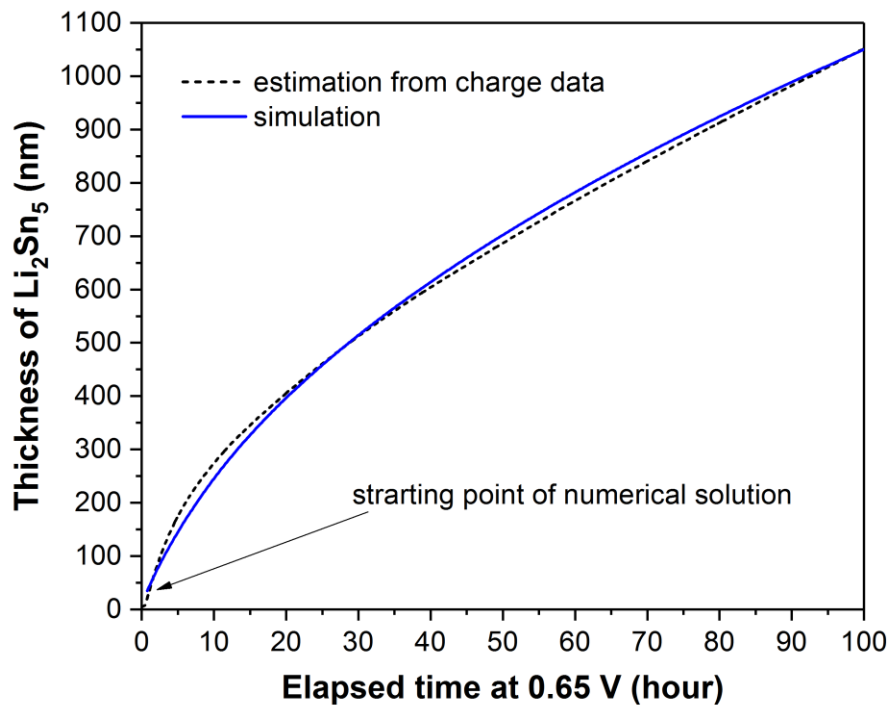


**Figure 4.12.** Comparison of the calculated thickness  $\text{Li}_2\text{Sn}_5$  phase and the estimation from the charge data. The arrow indicates the starting thickness of  $\text{Li}_2\text{Sn}_5$  in finite-difference calculation.

In addition, Fig. 4.12 shows the comparison of the simulated thickness of  $\text{Li}_2\text{Sn}_5$  and estimated values by considering the total charge accumulated at 0.65 V. An arrow in Fig. 4.12 indicates the starting point of the calculation. A good agreement is found indicating the simulation results for the phase boundary position is reasonable. It is seen that the growth of the  $\text{Li}_2\text{Sn}_5$  phase is in a mixture of diffusion-controlled and interface-controlled kinetics.

Since the two concentrations at the phase boundary are coupled as seen in boundary condition (b3), a decrease in the supersaturation at the phase boundary in the  $\text{Li}_2\text{Sn}_5$  phase leads to a decrease in the concentration on the other side of the interface as well. However,

a more complicated evolution of the Li concentration in the Sn phase is seen in Fig. 4.11b. Since the Sn phase does not reach saturation during the nucleation period (the initial profile in Sn (Fig. 4.4) is not uniform), the high Li concentration at the phase boundary keeps driving Li into the Sn phase while the boundary moves forward, as seen in the concentration profiles in the Sn layer at 3 and 5 hours. The concentration in the Sn phase reaches saturation around 10 hours after the potential is lowered to 0.65 V. Subsequently, the concentration in the Sn layer starts to decrease to relax the excess Li above the Li solubility by diffusing toward the phase boundary and contributing to the phase transformation (which we refer to as flux reversal). As discussed below, the evolution of Li in the Sn induces a stress which causes the transient behavior observed in the curvature measurement.

#### 4.4 Mechanisms of diffusion-induced stress

The numerical solution provides a model for both the phase propagation and the Li concentration profile in the layers. Here we utilize these results to understand the evolution of the Li-induced stress distribution in the anode. As seen in the Fig. 4.11a, the concentration profile in the  $\text{Li}_2\text{Sn}_5$  phase remains fairly linear during the interface propagation. Therefore, we assume the stress in the  $\text{Li}_2\text{Sn}_5$  region remains at a constant low strain-rate yield stress. For the Sn phase, in previous work, we reported that the Sn layer reaches the state of yield during the SEI formation period at 0.8 V before initiating Sn- $\text{Li}_2\text{Sn}_5$  phase transformation. As the concentration in the Sn layer evolves (Fig. 4.11b), two types of stress mechanisms are considered as described below.

##### 4.4.1. Rate-dependent plasticity

First, as Li is driven into the Sn film, the rate-dependent stress is related to the strain rate of the Sn film. Here, we consider the film as an isotropic layer bonded to a rigid substrate, so the total strain rate in the lateral direction is constrained as

$$\dot{\epsilon} = \dot{\epsilon}^c + \dot{\epsilon}^e + \dot{\epsilon}^p = 0 \quad \{4.30\}$$

where  $\dot{\epsilon}^c$  is the composition induced strain rate;  $\dot{\epsilon}^e$  is the elastic strain rate, and  $\dot{\epsilon}^p$  is the plastic strain rate.

For an isotropic continuum, the in-plane composition strain rate  $\dot{\epsilon}^c$  can be related to the volumetric strain rate  $\dot{\epsilon}_V^c$  as

$$\dot{\varepsilon}^c = \frac{1}{3} \dot{\varepsilon}_V^c = \frac{1}{3} \eta \dot{C} \quad \{4.31\}$$

where  $\eta$  is the volume expansion of Sn due to Li insertion and  $\dot{C}$  is the rate of Li concentration change.

Under the thin film configuration, the in-plane elastic strain rate can be represented as

$$\dot{\varepsilon}^e = \frac{\dot{\sigma}_{Sn}}{M_{Sn}} = \frac{1}{M_{Sn}} \frac{d\sigma_{Sn}}{dt} \quad \{4.32\}$$

where  $M_{Sn}$  is the biaxial modulus of Sn. In the stress measurement (Fig. 4.1b), the stress-thickness of the micron-level Sn film indicates the stress is in the MPa range, whereas the biaxial modulus of Sn is in the GPa range. In addition, the change of stress in the measurement happens in several hours. Therefore, we assume  $\dot{\varepsilon}^e$  is negligible in this case.

For the plastic strain rate, we assume it can be described by viscoplasticity<sup>25</sup> as

$$\dot{\varepsilon}_{ij}^p = \dot{\varepsilon}_o \left[ \left( \frac{\sigma_e}{\sigma_o} \right)^m - 1 \right] \frac{3}{2} \frac{S_{ij}}{\sigma_e} \quad \{4.33\}$$

where  $\dot{\varepsilon}_o$  is the strain rate constant;  $m$  is the strain rate exponent;  $\sigma_o$  is the nominal yield stress and it is assumed to be a constant.  $S_{ij}$  is the deviatoric stress and  $\sigma_e$  is the von

Mises stress:  $\sigma_e = \sqrt{\frac{3}{2} S_{ij} S_{ij}}$ . In the thin film case, the components of deviatoric stress are:

$S_{11} = S_{22} = \sigma_{Sn}/3$  and  $S_{33} = -2\sigma_{Sn}/3$ , and  $\sigma_e = |\sigma_{Sn}|$ . These results lead to the in-plane plastic strain rate as

$$\dot{\epsilon}^P = \dot{\epsilon}_{11}^P = \dot{\epsilon}_{22}^P = \frac{\dot{\epsilon}_o}{2} \left[ \left( \frac{|\sigma_{Sn}|}{\sigma_o} \right)^m - 1 \right] \quad \{4.34\}.$$

Since the  $\dot{\epsilon}^e$  is assumed to be negligible, by substituting  $\dot{\epsilon}^c$ ,  $\dot{\epsilon}^P$  and applying Eq. (4.30), the magnitude of the rate-dependent stress in the Sn film is represented as

$$\sigma_{Sn} = \sigma = \sigma_o \left( \frac{2\eta}{3\dot{\epsilon}_o} \dot{C} + 1 \right)^{\frac{1}{m}} \quad \{4.35\}.$$

When  $\dot{C}$  is large and positive, the associated volume expansion leads to a large strain rate and thus a large transient stress as seen in Fig. 4.1b.

To illustrate the influence of the parameters on the induced stress, a bilinear change in  $\dot{C}$  shown in Fig. 4.13a is assumed. Note that the actual  $\dot{C}$  in the experiment is determined by the experimental condition and the kinetic parameters of the system. The assumed variation of  $\dot{C}$  in Fig. 4.13a is chosen for illustration purpose only. In Fig. 4.13,  $\frac{\sigma}{\sigma_o}$  is the normalized rate-dependent stress.  $\dot{C}$  can be normalized with its maximum value  $\dot{C}_{max}$ , and the normalized rate of concentration  $\frac{\dot{C}}{\dot{C}_{max}}$  can be represented as

$$\frac{\dot{C}}{\dot{C}_{max}} = \omega \frac{t}{\lambda} \quad \{4.36\}$$

where  $\frac{t}{\lambda}$  is the normalized time, and  $\lambda$  is total length of time  $t$ ;  $\omega$  is the slope of  $\frac{\dot{c}}{\dot{c}_{max}}$  and  $\frac{t}{\lambda}$ , i.e., the second derivative with respect to time. The slope  $\omega$  depends on the experimental condition and may alter during the experiment.

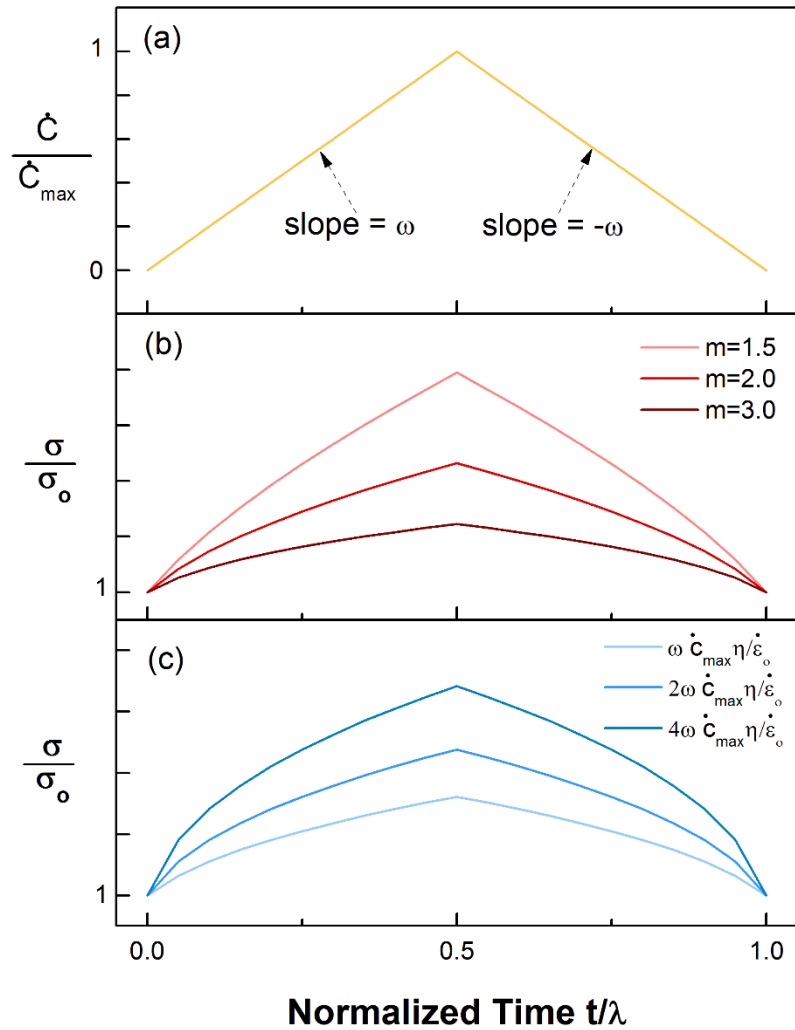


**Figure 4.13.** Demonstration of the correlation between rate-dependent stress and the material parameters. (a) normalized rate of concentration change  $\frac{\dot{c}}{\dot{c}_{max}}$ ; (b) and (c): trends of the normalized rate-dependent stress  $\frac{\sigma}{\sigma_o}$  with parameters  $m$  and  $\frac{\eta}{\epsilon_o} \omega \dot{c}_{max}$ , respectively.

Fig. 4.13a shows an example of  $\frac{\dot{c}}{\dot{c}_{max}}$  versus  $\frac{t}{\lambda}$  with a constant slope  $\omega$ , in which  $\frac{\dot{c}}{\dot{c}_{max}}$  is assumed to start increasing linearly to 1 as the normalized time  $\frac{t}{\lambda}$  reaches 0.5, and then decrease linearly (note that  $\omega = 2$  in Fig. 4.13a). Eq. (4.36) can be used to describe the first segment of  $\frac{\dot{c}}{\dot{c}_{max}}$  in Fig. 4.13a, where the slope  $\omega$  is positive, and the rate-dependent stress shown in Eq. (4.35) can be normalized as

$$\frac{\sigma}{\sigma_o} = \left( \frac{2\eta}{3\dot{\epsilon}_o} \omega \dot{c}_{max} \frac{t}{\lambda} + 1 \right)^{\frac{1}{m}} \quad \{4.37\}.$$

It is seen that the magnitude of  $\frac{\sigma}{\sigma_o}$  depends on the values of  $m$  and  $\frac{\eta}{\dot{\epsilon}_o} \omega \dot{c}_{max}$ . The strain rate exponent  $m$ , the volume expansion associated with Li insertion  $\eta$  and the strain rate constant  $\dot{\epsilon}_o$  are material properties, whereas the product  $\omega \dot{c}_{max}$  is related to the Li diffusivity in the material, and can vary with experimental conditions. A similar expression for the decreasing portion of Fig. 4.13a, which is not shown for brevity.

To illustrate the influence of the parameters  $m$  and  $\frac{\eta}{\dot{\epsilon}_o} \omega \dot{c}_{max}$  on the normalized rate-dependent stress, Figs. 4.13b and 4.13c show calculations of  $\frac{\sigma}{\sigma_o}$  for different values of  $m$  and  $\frac{\eta}{\dot{\epsilon}_o} \omega \dot{c}_{max}$ , respectively, with the values indicated in the figures. It can be seen that when  $\frac{\dot{c}}{\dot{c}_{max}}$  is positive and large, it leads to a high rate-dependent stress. In contrast, when  $\frac{\dot{c}}{\dot{c}_{max}}$  is positive but small,  $\frac{\sigma}{\sigma_o}$  approaches 1 as the rate-dependent stress approaches the nominal yield stress. As shown in Fig. 4.13b, for smaller values of  $m$ ,

$\frac{\sigma}{\sigma_0}$  is more sensitive to  $\frac{\dot{c}}{\dot{c}_{max}}$  and results in a larger magnitude of  $\frac{\sigma}{\sigma_0}$ . The parameters  $\frac{\eta}{\varepsilon_0}$  and  $\omega\dot{c}_{max}$  influence stress evolution through the non-dimensional group  $\frac{\eta}{\varepsilon_0}\omega\dot{c}_{max}$ , which is illustrated in Fig. 4.13c. Higher volume expansion coefficient  $\eta$  and higher lithiation rate  $\omega\dot{c}_{max}$  lead to higher stress as expected.

#### 4.4.2 Elastic unloading

There is also a second mechanism that can contribute to the transient stress response. When the phase boundary nucleates and begins to propagate, the Li flux in the supersaturated Sn phase can reverse its direction and flow towards the phase boundary. Such a reversal leads to elastic unloading of the Sn phase due to a decrease in volume. The relaxation of the transient stress response would be due to a combination of decreasing rate of concentration change and elastic unloading. The stress state of the elastic unloading can be described as

$$\sigma_{Sn} = \sigma_{Sn}^{ul} - B\Delta C^{ul} \quad \{4.38\}$$

where  $B = \eta M_{Sn}$  for the thin film geometry.  $\sigma_{Sn}^{ul}$  is the local stress in Sn right before elastic unloading; it is a function of position  $x$  and its magnitude is given by Eq. (4.35).  $\Delta C^{ul}$  is the local decrease of concentration during elastic unloading. This mechanism causes the stress in Sn to be reduced from the stress produced by the plastic deformation. Note that the two mechanisms may happen at different positions in the Sn phase at the same time, e.g., elastic unloading can start happening in a region near the phase boundary

while the interior of the layer remains at the state of plastic yield.

#### 4.4.3 Correlation between Li concentration evolution and diffusion-induced stress

Fig. 4.14 shows a schematic plot to demonstrate the correlation between the evolution of Li concentration and the corresponding stress for the two-phase system being investigated here. In Fig. 4.14a, two calculated Li concentration profiles (at time step  $t$  and its preceding time step  $t-1$ ) are presented. It is seen that as the phase boundary propagates from  $S(t-1)$  to  $S(t)$ , the Li concentrations in the Sn phase at the phase boundary decreases (which is also seen in Figs. 4.10 and 4.11b).

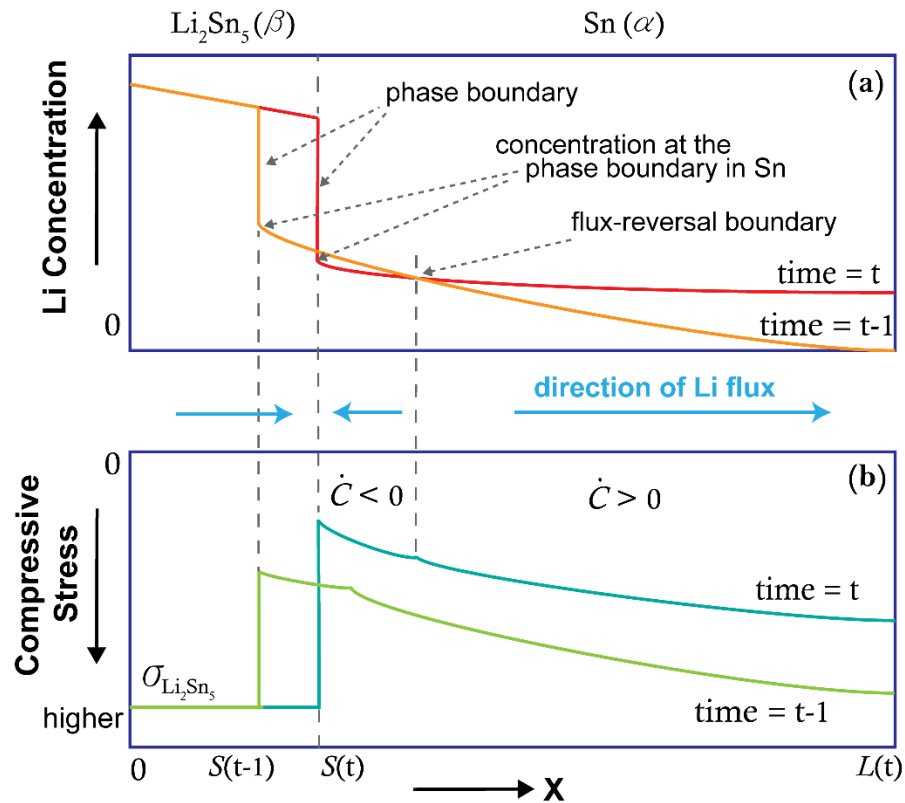


**Figure 4.14.** Schematic plots of: (a) Li concentration profiles at time  $t$  and  $t-1$  showing the flux-reversal boundary induced by the phase boundary propagation; (b) the stress distribution at time  $t$  corresponding to the evolution in (a) and the preceding stress distribution at time  $t-1$ .

Such evolution leads to the two overlapping concentration profiles in the Sn phase shown in the figure. The point where the two profiles have the same concentration is labeled as “flux-reversal boundary” in Fig. 4.14a. The directions of the Li flux on either side of it are in opposite directions as shown by the arrows in light blue. Depending on the direction of Li flux (i.e., the sign of  $\dot{C}$ ), the corresponding stress in Sn at time  $t$  (Fig. 4.14b) can be determined using the mechanisms discussed above. As mentioned earlier, the concentration profile in the  $\text{Li}_2\text{Sn}_5$  phase is linear and the stress is assumed to be at a constant low strain-rate yield stress  $\sigma_{\text{Li}_2\text{Sn}_5}$ . For the Sn phase region beyond the flux-reversal boundary, the Li concentration increases from time  $t-1$  to time  $t$  (i.e.,  $\dot{C} > 0$ ), and the higher stress state is due to the rate-dependent plasticity (i.e., viscoplasticity) associated with the strain rate induced by the increasing Li concentration (Eq. 4.35). For the Sn phase region closed to the phase boundary, the Li concentration decreases from time  $t-1$  to time  $t$  (i.e.,  $\dot{C} < 0$ ), in which the stress decreases from its rate-dependent stress (elastic unloading, Eq. 4.38) due to the reversed Li flux from Sn to the phase boundary. Similarly, the stress distribution at time  $t-1$  shown in Fig. 4.14b (or other time steps) can be obtained from the corresponding Li concentration profiles at the preceding times.

#### 4.4.4 Calculation of stress evolution observed in experiments

In the numerical solution, the rate of concentration change  $\dot{C}$  at each nodal point  $n$  at a given time step can be calculated from the concentrations in that and the preceding time steps, which can be expressed as

$$\dot{C}_n^{j+1} = \frac{C_n^{j+1} - C_n^j}{\Delta t} \quad \{4.39\}$$

For nodal points that have positive sign  $\dot{C}_n^{j+1}$ , the states of stress are determined by Eq. (4.35). In contrast, if the sign is negative, the stress is determined by Eq. (4.38). Sequentially, an integral of stress with thickness is performed to have the calculated stress-thickness that can be used to compare with the measured values in the experiment. As discussed in chapter 3, the stress-thickness of the entire anode  $\langle \sigma \rangle h_f$  can be represented as

$$\langle \sigma \rangle h_f = \langle \sigma_{SEI} \rangle h_{SEI} + \langle \sigma_{Sn} \rangle h_{Sn} + \langle \sigma_{Li_2Sn_5} \rangle h_{Li_2Sn_5} \quad \{4.40\}.$$

In addition, by the steady-state analysis, we found the low strain-rate yield stress of  $Li_2Sn_5$  is around -29 MPa, and stress-thickness contribution from the SEI layer is around 8.8 MPa- $\mu$ m. Here, we use the information obtained previously from the steady-state and the diffusion profile by numerical solution to analyze the transient state. The elastic modulus and Poisson's ratio of Sn reported by Stournara et al.<sup>26</sup> and the material parameters applied in the calibration are shown in Table 4.4.

**Table 4.4.** Parameters used in the stress calculation

Biaxial modulus of fused-silica, $M_S$	86.4 GPa
Biaxial modulus of Sn, $M_{Sn}$	76.9 GPa
Thickness of fused-silica substrate, $h_S$	500 $\mu$ m
Nominal yield stress of Sn, $\sigma_o$	-20 MPa
Low strain-rate yield stress of $Li_2Sn_5$ , $\sigma_{Li_2Sn_5}$	-29 MPa
Stress-thickness of SEI, $\sigma_{SEI} h_{SEI}$	8.8 MPa- $\mu$ m

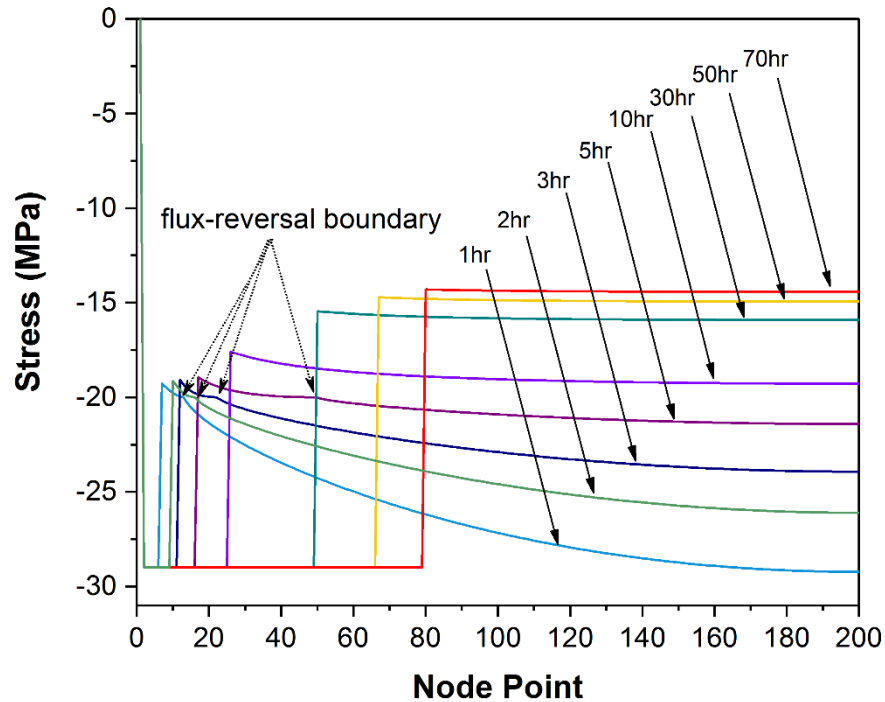


**Figure 4.15.** The calculated evolution of stress distribution in the Sn anode during the potentiostatic lithiation at 0.65 V.

The calculated stress distribution in the anode is shown in Fig. 4.15 for different times indicated on the figure. The regions where the different stress mechanisms activate are distinguished by the arrows labeled “flux-reversal boundary” in each stress profile. As discussed above, the stress in the regions of Sn far away from the phase boundary (distances greater than indicated by the arrows) is at a higher stress state governed by viscoplasticity (Eq. 4.35). Near the phase boundary (distances less than the arrows), the stress decreases from its rate-dependent stress as described by elastic unloading (Eq. 4.38). The integrated stress-thickness of the entire anode is used to fit to the experimental values by wafer curvature measurements and calibrate the mechanical parameters used in Eqs. (4.35) and (4.38). The fitting result is shown in Fig. 4.1b, in which the solid line

corresponds to experimental data and the dash line corresponds to the simulation result. The points marked by arrows correspond to the concentration profile in Fig. 4.10 and Fig. 4.11 and the stress profile in Fig. 4.15 at the corresponding times. The results of calibrated parameters are presented in Table 4.5.

**Table 4.5.** Material parameters obtained by the stress-thickness fitting in Fig. 4.1b

Strain rate exponent, $m$	1.46
Strain rate coefficient, $\varepsilon_0$	$1.6 \times 10^{-7}$
Volume expansion of Sn phase due to Li insertion, $\eta$	$6.5 \times 10^{20}$ nm <sup>3</sup> /mol

According to the results in Figs. 4.1b and 4.15, the stress in Sn induced by Li diffusion leads to a stress state above the initial yield stress at the beginning of the phase transformation. At this stage, the contribution to the stress-thickness from the Li<sub>2</sub>Sn<sub>5</sub> phase is smaller than the Sn phase since the majority of the anode remains in the Sn phase. Therefore, the high stress-thickness in the transient behavior is mostly the result of rate-dependent stress in Sn. Subsequently, as the excess Li concentration in the Sn layer approaches saturation, the decrease in the rate of concentration change relaxes the high stress state in Sn (1-5 hours at region greater than the flux reversal boundary in Fig. 4.15), so that the high stress-thickness value of the anode is eased. The decrease in the excess Li concentration leads to a lower stress state in Sn by elastic unloading (the entire Sn region beyond 10 hour in Fig. 4.15). A balance between the high stress in Li<sub>2</sub>Sn<sub>5</sub> and the lower stress in Sn leads to the fairly constant value of stress-thickness between 10 and 30 hours (Fig. 4.1b). As the Sn/Li<sub>2</sub>Sn<sub>5</sub> phase boundary propagates in Sn, the compressive stress-thickness reaches a steady rate of increase as the contribution from Li<sub>2</sub>Sn<sub>5</sub> phase becomes dominant and the stress in Sn reaches a steady-state value.

## 4.5 Conclusions

In this chapter, we studied the large transient stress observed at the beginning of the Sn-Li<sub>2</sub>Sn<sub>5</sub> phase transformation. We performed a finite-difference calculation to simulate the 1-D moving boundary problem of the Li<sub>2</sub>Sn<sub>5</sub> phase growing into the parent Sn phase during potentiostatic lithiation. Using the calculated Li concentration profiles, we proposed mechanisms for the observed stress evolution in Sn. The kinetic and mechanical parameters were calibrated with the experimental measurements. The main conclusions of this study are:

- The obtained results of the kinetic modeling indicate that the Li diffusivity in Sn and Li<sub>2</sub>Sn<sub>5</sub> are approximately  $10^{-12}$  cm<sup>2</sup>/s, and the reaction rate coefficient is approximately  $5 \times 10^{-6}$  cm<sup>4</sup>/mol s. The results obtained by the numerical solution are consistent with the values found in the steady-state analysis (chapter 3).
- The high value of stress-thickness of the transient behavior at the beginning of Sn-Li<sub>2</sub>Sn<sub>5</sub> phase transformation is induced by rate-dependent plasticity associated with the excess Li diffusion in Sn layer.
- As the phase boundary propagates, the flux of Li diffusion decreases and the relaxation of the excess Li concentration leads to a lower state of stress in Sn by elastic unloading. Following the steep drop, the balance between the region of elastic unloading and the growing new phase result in a period of approximate constant stress-thickness. Subsequently, the compressive stress-thickness begins to increase at a steady rate as the new phase continues to grow.

The modeling and analysis method developed in this chapter may can be extended to other material systems to study phase transformation problems and future research on

the failure mechanisms of the battery electrodes.

## References

1. A. F. Bower and P. R. Guduru, *Modelling Simul. Mater. Sci. Eng.*, **20** 045004 (2012).
2. J. Zhang, B. Lu, Y. Song, and X. Ji, *Journal of Power Sources*, **209** 220-227 (2012).
3. J. Christensen, *Journal of The Electrochemical Society*, **157** (3), A366-A380 (2010).
4. T. G. Myers and S. L. Mitchell, *Applied Mathematical Modeling*, **35** 4281-4294 (2011).
5. L. I. Rubinshteĭn, *The Stefan Problem*, American Mathematical Soc. (1971).
6. J. M. Hill, *One-dimensional Stefan problems: an introduction.*, Longman Scientific & Technical (1987).
7. H. S. Carslaw and J. C. Jaeger, *Conduction of Heat in Solids*, Oxford University Press (1959).
8. Z. Cui, F. Gao, and J. Qu, *Journal of the Mechanics and Physics of Solids*, **61** 293-310 (2013).
9. A. Singer, A. Ulvestad, H.-M. Cho, J. W. Kim, J. Maser, R. Harder, Y. S. Meng, and O. G. Shpyrko, *Nano Letter*, **14** (9), 5295-5300 (2014).
10. S. Hulikal, C.-H. Chen, E. Chason, and A. Bower, *Journal of Electrochemical Society*, **163** (13), A2647-A2659 (2016).
11. M. D. Levi, E. Markevich, C. Wang, and D. Aurbach, *Journal of Electroanalytical Chemistry*, **600** (1), 13-22 (2007).
12. M. Hillert, in *Lectures on the Theory of Phase Transformations*, H. I. Aaronson, ed., The Minerals, Metals & Materials Society, (1999).
13. A. V. Virkar, *Journal of Power Sources*, **147** (1-2), 8-31 (2005).
14. W. G. Moffatt, *The Handbook of Binary Phase Diagrams*, Schenectady, N.Y. (1978).
15. J. Svoboda, F. D. Fischer, P. Fratzl, E. Gamsjager, and N. K. Simha, *Acta Materialia*, **49** 1249-1259 (2001).
16. J. Sietsma and S. v. d. Zwaag, *Acta Materialia*, **52** 4143-4152 (2004).
17. J. Crank and R. S. Gupta, *IMA Journal of Applied Mathematics*, **10** (1), 19-33 (1972).
18. J. Crank, *Free and Moving Boundary Problems*, Oxford (1984).
19. B. Chao, S.-H. Chae, X. Zhang, K.-H. Lu, M. Ding, J. Im, and P. S. Ho, *Journal of Applied Physics*, **100** 084909 (2006).
20. J. W. Cahn and J. E. Hilliard, *American Institute of Physics*, **31** 688 (1959).
21. J. W. D. Connolly and A. R. Williams, *Physical Review B*, **27** (8), 5169-5172 (1983).
22. H. Ji, D. Chopp, and J. E. Dolbow, *International Journal for Numerical Methods in Engineering*, **54** (8), 1209-1233 (2002).
23. M. Hillert, *Metallurgical Transactions A*, **6** (1), 5-19 (1975).
24. M. Winter and J. O. Besenhard, *Electrochimica Acta*, **45** 31-50 (1999).
25. A. F. Bower, *Applied Mechanics of Solids*, CRC Press (2009).
26. M. Stournara, P. R. Guduru, and V. Shenoy, *Journal of Power Sources*, **208** 165-169 (2012).

# Chapter 5.

## Measurements and Numerical Solution of Two Moving Boundaries

---

In Chapter 4, the numerical solution using the finite-difference method is developed to investigate the Sn/Li<sub>2</sub>Sn<sub>5</sub> phase boundary movement. The simulated concentration profile enabled the further analysis of the stress-induced stress in Sn phase observed in the *in situ* curvature measurements.

In this chapter, we study the Li-Sn phase transformations involving Sn, Li<sub>2</sub>Sn<sub>5</sub>, and LiSn phases. *In situ* curvature measurement is also employed to investigate the stress evolution in the anodes while phase transformations take place. Two types of electrochemical experiments are used to understand the phase boundary propagation. In the first case, the Li<sub>2</sub>Sn<sub>5</sub> phase is grown first to approximate half of the sample thickness, and then the LiSn phase transformation is activated. Thus, in the first stage of this experiment, the observations in current density and curvature measurement are related to the progression of a single phase boundary. In the subsequent stage, the observations are contributed from the movement of two phase boundaries. The second type of experiment involves the simultaneous growth of Li<sub>2</sub>Sn<sub>5</sub> and LiSn phase from the Sn anode surface.

To quantitatively understand how the phase boundaries propagate correlated with the measured current density and the acquired curvature change of the thin film samples,

the finite-difference method for a single moving boundary in chapter 4 is extended into a framework of two moving boundaries. The simulated results are compared with the experimental values to obtain the relevant kinetic and mechanical parameters.

## **5.1. Experimental condition**

### *5.1.1 Sample description*

The Sn thin film sample used in this study included a 25 nm Ti layer, a 50 nm Cu layer, and a Sn layer deposited on a fused-silica wafer. The thickness of the Sn layer was 1.85  $\mu\text{m}$  or 1  $\mu\text{m}$  as described in the following. The details of the sample fabrication is described in section 2.1. The 500  $\mu\text{m}$  thick fused-silica wafer served as the substrate in the *in situ* curvature measurement.

### *5.1.2 Electrochemical experiment*

The thin film Sn sample was employed as the working electrode, where as a Li metal foil (1.5 mm thick, 50.8 mm in diameter) was served as the counter electrode and the reference electrode in the customized half cell (section 2.2.1). The composition electrolyte used in this work was 1.2 M  $\text{LiPF}_6$  in EC/DEC solvent (3:7 wt %). The experimental setup was enabled to stabilize for 12 hours before performing the electrochemical experiment.

The electrochemical processes of the experiments for the investigation of phase boundary propagation and for the numerical analysis are described as follow. In each experiment, the potential was first brought down from the original open circuit potential ( $\sim 2.7$  V) to 0.8 V vs.  $\text{Li/Li}^+$  by a galvanostatic lithiation ( $-12.5 \mu\text{A}/\text{cm}^2$ ). The potential was then held at 0.8 V for 20 hours for the formation of the solid electrolyte interphase

(SEI), in order to distinguish the Li consumption by SEI formation from the subsequent phase transformations as much as possible. The cell then proceeded with the following electrochemical processes.

For the first type of experiment (with 1.85  $\mu\text{m}$  Sn), after the 20 hour potential hold at 0.8 V, the potential was changed to 0.65 V for 50 hours, where the formation of  $\text{Li}_2\text{Sn}_5$  phase was activated. The potential was then kept at 0.5 V for 100 hours for the formation of  $\text{Li}_2\text{Sn}_5$  and LiSn phases.<sup>1, 2</sup> This experiment is referred to as “Experiment [i]” in the later discussion, and the experimental procedure is presented in Table 5.1.

**Table 5.1.** Experimental condition of Experiment [i]: the growth of  $\text{Li}_2\text{Sn}_5$  and LiSn phases with a pre-grown  $\text{Li}_2\text{Sn}_5$  layer

#	Step	Description
1	lithiation	galvanostatic, $-12.5 \mu\text{A}/\text{cm}^2$ from OCP to 0.8 V
2	SEI formation	potentiostatic, at 0.8 V for 20 hours
3	phase transformation of $\text{Li}_2\text{Sn}_5$	potentiostatic, at 0.65 V for 50 hours
4	phase transformations of $\text{Li}_2\text{Sn}_5$ and LiSn	potentiostatic, at 0.5 V for 100 hours

For the second type of experiment (with 1.85  $\mu\text{m}$  Sn), the potential was directly changed to 0.5 V after the 20 hour SEI formation at 0.8 V. The potential was held at 0.5 V for 80 hours where both the formation of  $\text{Li}_2\text{Sn}_5$  and LiSn phases occurred. This experiment is referred to as “Experiment [ii]”, and the experimental procedure is presented in Table 5.2.

**Table 5.2.** Experimental condition of Experiment [ii]: the simultaneous growth of  $\text{Li}_2\text{Sn}_5$  and  $\text{LiSn}$  phases

#	Step	Description
1	lithiation	galvanostatic, $-12.5 \mu\text{A}/\text{cm}^2$ from OCP to 0.8 V
2	SEI formation	potentiostatic, at 0.8 V for 20 hours
3	phase transformations of $\text{Li}_2\text{Sn}_5$ and $\text{LiSn}$	potentiostatic, at 0.5 V for 80 hours

To estimate the surface Li concentration for the kinetic modeling, the third type of experiment with a 1  $\mu\text{m}$  Sn film is performed. After a 20 hour SEI formation at 0.8 V, the potential at 0.5 V until the current density decreased below  $-0.04 \mu\text{A}/\text{cm}^2$  ( $\sim C/2500$ ), where the film was considered fully transformed in the  $\text{LiSn}$  phase. Subsequently, the sample was switched to open circuit potential measurement for 10 hours to let the Li concentration in the anode to reach equilibrium as the potential relaxed to around 0.65 V. Following the open circuit, a potentiostatic intermittent titration technique (PITT) experiment was performed: the potential was decreased in 20 mV steps over a range of from 0.58 V to 0.5 V. The sample was held at each potential until the current density decreased below  $-0.025 \mu\text{A}/\text{cm}^2$  ( $\sim C/4000$ ), at which the sample was considered to have reach a new equilibrium state of charge with the applied potential. This experiment is referred to as Experiment [iii], and the experimental procedure is presented in Table 5.3.

**Table 5.3.** Experimental condition of Experiment [iii]: the estimation of surface Li concentration in LiSn phase

#	Step	Description
1	lithiation	galvanostatic, -12.5 $\mu\text{A}/\text{cm}^2$ from OCP to 0.8 V
2	SEI formation	potentiostatic, at 0.8 V for 20 hours
3	phase transformations of $\text{Li}_2\text{Sn}_5$ and LiSn	potentiostatic, at 0.5 V until the current density below -0.04 $\mu\text{A}/\text{cm}^2$
4	open circuit	10 hours
5	PITT	20 mV step from 0.58 V to 0.5 V with cut-off current density of -0.025 $\mu\text{A}/\text{cm}^2$

### 5.1.3 In situ stress measurement

During the electrochemical experiments, the MOSS system (section 2.1) was employed to acquire the real time curvature change of the substrates.<sup>3</sup> The measured curvature change  $\frac{1}{R}$  is related to the product of stress  $\langle\sigma\rangle$  and thickness  $h_f$  of the film (referred to as stress-thickness  $\langle\sigma\rangle h_f$ ) as described by the Stoney Equation.<sup>4</sup> For a film consisting of multiple layers, the measured stress-thickness is related to the contributions from the layers that involves with Li incorporation. In this chapter, phase formations of both  $\text{Li}_2\text{Sn}_5$  and LiSn phases are studied; thus, the measured curvature change  $\frac{1}{R}$  can be represented as

$$\frac{M_s h_s^2}{6} \frac{1}{R} = \langle\sigma\rangle h_f = \langle\sigma_{SEI}\rangle h_{SEI} + \langle\sigma_{Sn}\rangle h_{Sn} + \langle\sigma_{Li_2Sn_5}\rangle h_{Li_2Sn_5} + \langle\sigma_{LiSn}\rangle h_{LiSn} \quad \{5.1\}$$

where  $h_s$  and  $M_s$  are the thickness and biaxial modulus of the substrate, respectively.

The subscripts denote the stress and thickness of SEI, Sn,  $\text{Li}_2\text{Sn}_5$ , and LiSn layers. In Eq. (5.1), the thickness and the stress in the lateral direction are assumed to be uniform.

#### 5.1.4 Focused-ion beam and X-ray diffraction analysis

Focused-ion beam (FIB) cross-section and  $\theta$ - $2\theta$  X-ray diffraction (XRD) were performed after the electrochemical experiments to examine the film thickness and the resulting phases in the lithiated samples. The results of FIB cross-section images are presented in Fig. 5.1, and the XRD results are shown in Fig. 5.2. To prevent sample degradation by moisture and air during the XRD measurement, the lithiated samples were assembled into the customized coin cell casing with a Kapton window (section 2.3); thus, the influences and peaks of the Kapton window and stainless steel coin cell casing were observed in the XRD results.

Fig. 5.1a shows the cross-section of the sample in Experiment [i], in which a two-layer structure is observed, and in the corresponding XRD result (Fig. 5.2a),  $\text{Li}_2\text{Sn}_5$  and LiSn phases are identified. Whereas, for the Experiment [ii] shown in Fig. 5.1b, a three-layered structure is seen in the cross-section, and the corresponding XRD result (Fig. 5.2b) indicates the existence of Sn,  $\text{Li}_2\text{Sn}_5$ , and LiSn phases. The layers are labeled with the phases in the figures. These findings show that the phase boundaries propagate relatively homogeneously in the Sn films. Therefore, a 1-D kinetic modeling with finite-difference analysis is applied in this chapter to study the movement of the phase boundaries.

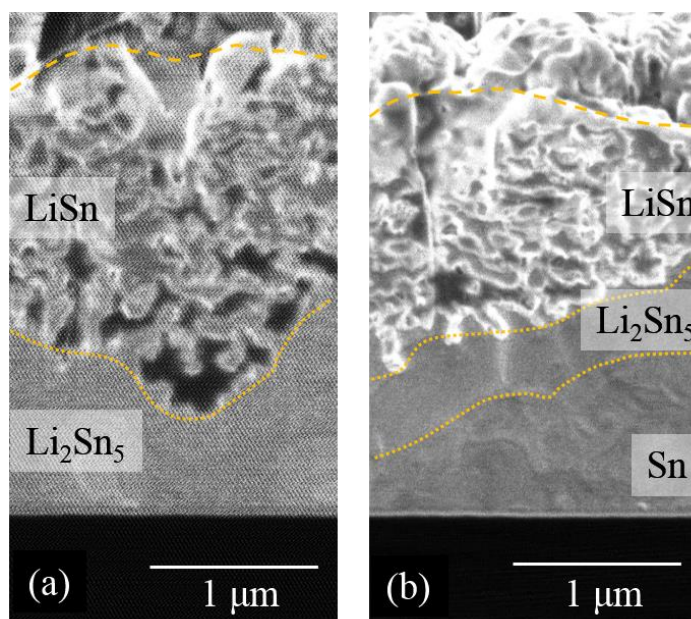


**Figure 5.1.** Cross-section images of lithiated samples in: (a) Experiment [i] showing a two layer structure with the  $\text{Li}_2\text{Sn}_5/\text{LiSn}$  phase boundary, (b) Experiment [ii] showing a three layer structure with the  $\text{Sn}/\text{Li}_2\text{Sn}_5$  and  $\text{Li}_2\text{Sn}_5/\text{LiSn}$  phase boundaries. The surface is indicated by a dash line and the phase boundaries are by dotted lines.

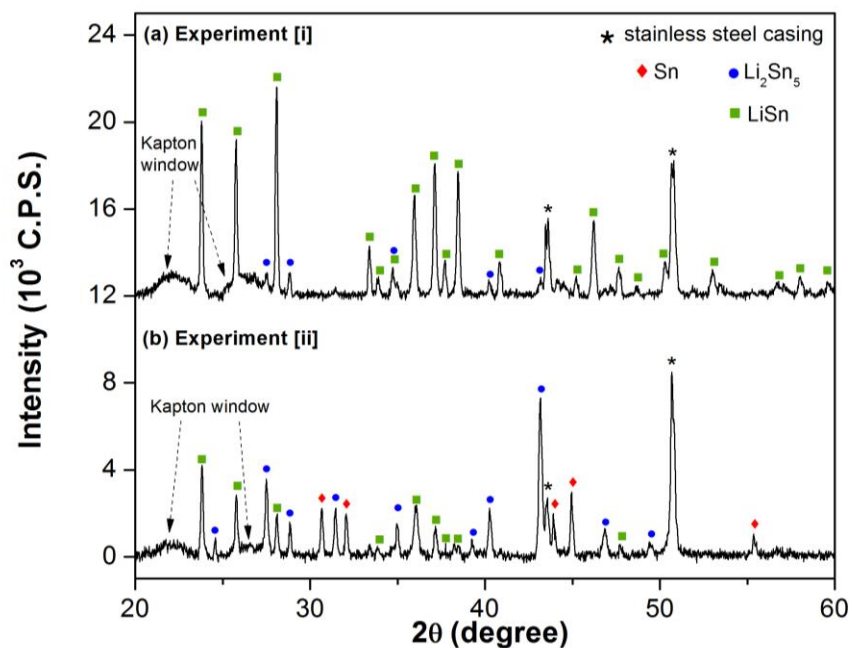


**Figure 5.2.** XRD results of lithiated samples in: (a) Experiment [i] identifying the existence of  $\text{Li}_2\text{Sn}_5$  and  $\text{LiSn}$  phases, (b) Experiment [ii] identifying the existence of  $\text{Sn}$ ,  $\text{Li}_2\text{Sn}_5$  and  $\text{LiSn}$  phases.

## 5.2. Observation in electrochemical and stress measurements

In this section, the experimental results are presented. The modeling analysis of the phase boundary movement and stress evolution is discussed in section 5.4.

### 5.2.1 Experiment [i]: the growth of $\text{Li}_2\text{Sn}_5$ and $\text{LiSn}$ phases with a pre-grown $\text{Li}_2\text{Sn}_5$ layer

In the Experiment [i], after the 20 hour SEI formation at 0.8 V vs.  $\text{Li}/\text{Li}^+$ , the potential was held at 0.65 V for 50 hours and then changed to 0.5 V for 100 hours. The current density and the corresponding stress-thickness are shown in Fig. 5.3. Three segments of current density (Fig. 5.3a) and stress-thickness (Fig. 5.3b) that correspond to the potential holds at 0.8 V, 0.65 V, and 0.5 V are seen. As discussed in chapters 3 and 4, the saturated stress-thickness at 0.8 V relates to the yielded Sn layer and the surface SEI. When the potential was changed to 0.65 V, the  $\text{Sn-Li}_2\text{Sn}_5$  phase transformation was activated, and a transient stress state was observed in the stress-thickness followed by a steady and linear decreasing. When the potential changed to 0.5 V, the  $\text{Li}_2\text{Sn}_5\text{-LiSn}$  phase transformation was initiated, the stress-thickness gradually increased as the phase transformations took place. The details of kinetic modeling and stress analysis correspond to the simulation values (dash lines) in Fig. 5.3 are discussed in section 5.4.1.

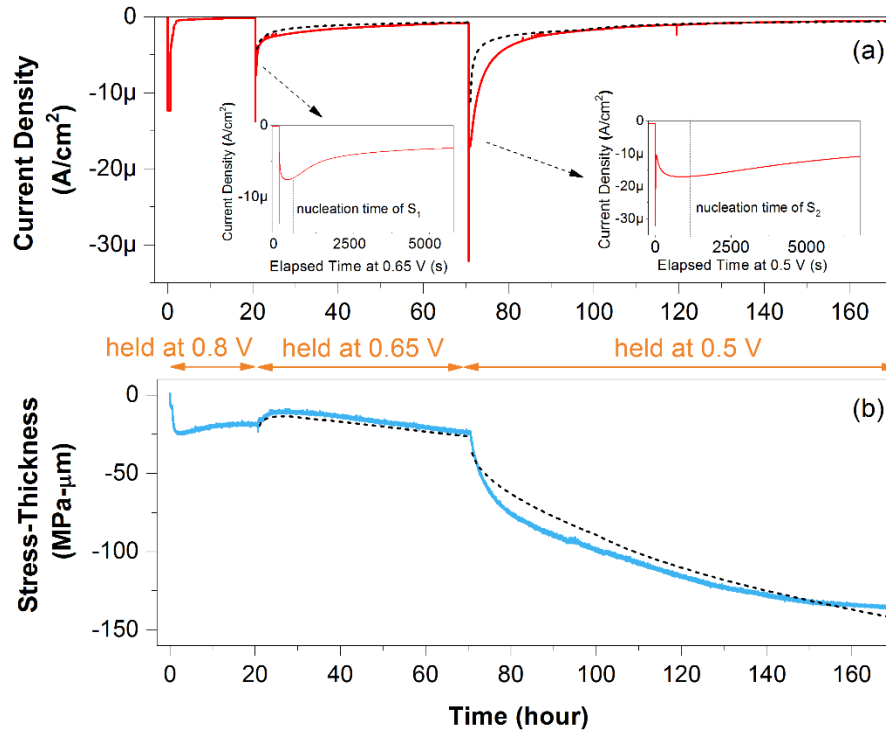


**Figure 5.3.** Measurements and calculation (dash lines) of the Experiment [i], in which the potential held at 0.8 V, 0.65 V and 0.5 V sequentially: (a) current density and two insets showing the nucleation of  $\text{Li}_2\text{Sn}_5$  and  $\text{LiSn}$  phases respectively, (b) stress-thickness.

### 5.2.2 Experiment [ii]: the simultaneous growth of $\text{Li}_2\text{Sn}_5$ and $\text{LiSn}$ phases

In the Experiment [ii], the potential was directly changed to 0.5 V vs.  $\text{Li}/\text{Li}^+$  after the 20 hour SEI growth at 0.8 V. The current density and the stress-thickness are shown in Fig. 5.4. For the potential hold at 0.8 V, the current density and the measured stress-thickness relate to the SEI formation at the surface and the yielded Sn layer. When the potential was changed to 0.5 V, the phase transformations of  $\text{Li}_2\text{Sn}_5$  and  $\text{LiSn}$  were activated simultaneously. A transient high stress was found which decreased rapidly and was followed by steady-state behavior. The details of kinetic modeling and stress analysis for the calculated values (dash lines) in Fig. 5.4 are discussed in section 5.4.2.

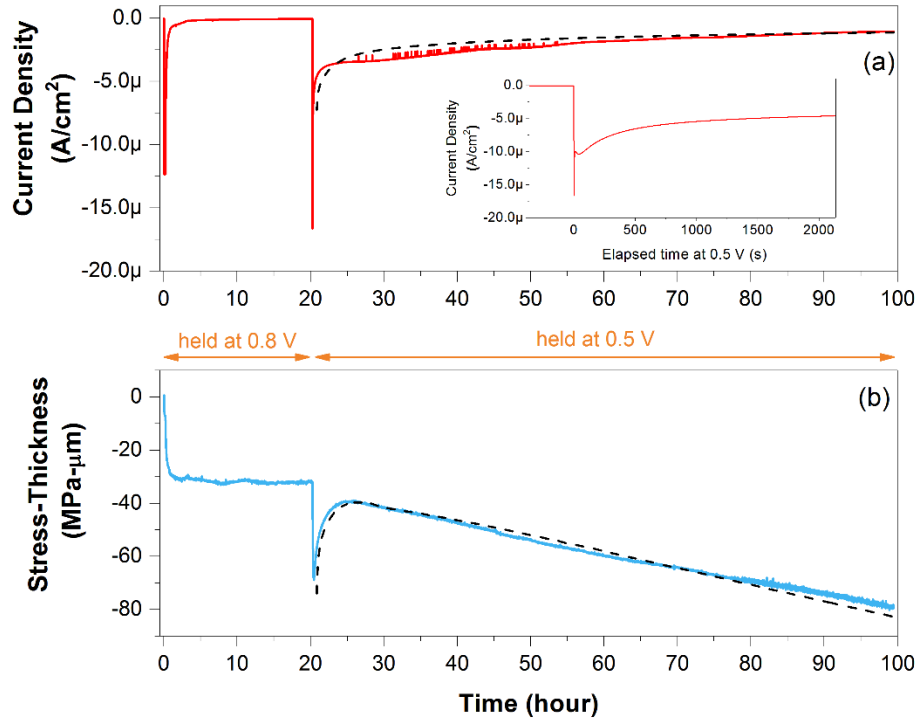


**Figure 5.4.** Measurements and calculation (dash lines) of the Experiment [ii], in which the potential held at 0.8 V and 0.5 V: (a) current density and inset showing the nucleation of  $\text{Li}_2\text{Sn}_5$  and  $\text{LiSn}$  phases, (b) the corresponding stress-thickness showing a transient high stress.

### 5.2.3 Experiment [iii]: the estimation of surface Li concentration in $\text{LiSn}$ phase

During the potential hold at 0.5 V in Experiment [ii], the Sn layer was considered fully transformed into the  $\text{LiSn}$  phase as the current density decreased to a very small value ( $-0.04 \mu\text{A}/\text{cm}^2$ ). The accumulated Li concentration obtained at each potential holding during subsequent PITT process is shown in Fig 5.5, in which the corresponding capacity is also marked. Here, we assume a new equilibrium of Li concentration in each potential hold is reached as the current density decreases to  $-0.025 \mu\text{A}/\text{cm}^2$  in each step. The surface Li concentration at each potential hold is assumed to be the same as the averaged Li concentration at that potential. The result is used as the surface Li concentration  $C_S$  in the finite-difference calculation discussed in section 5.3.

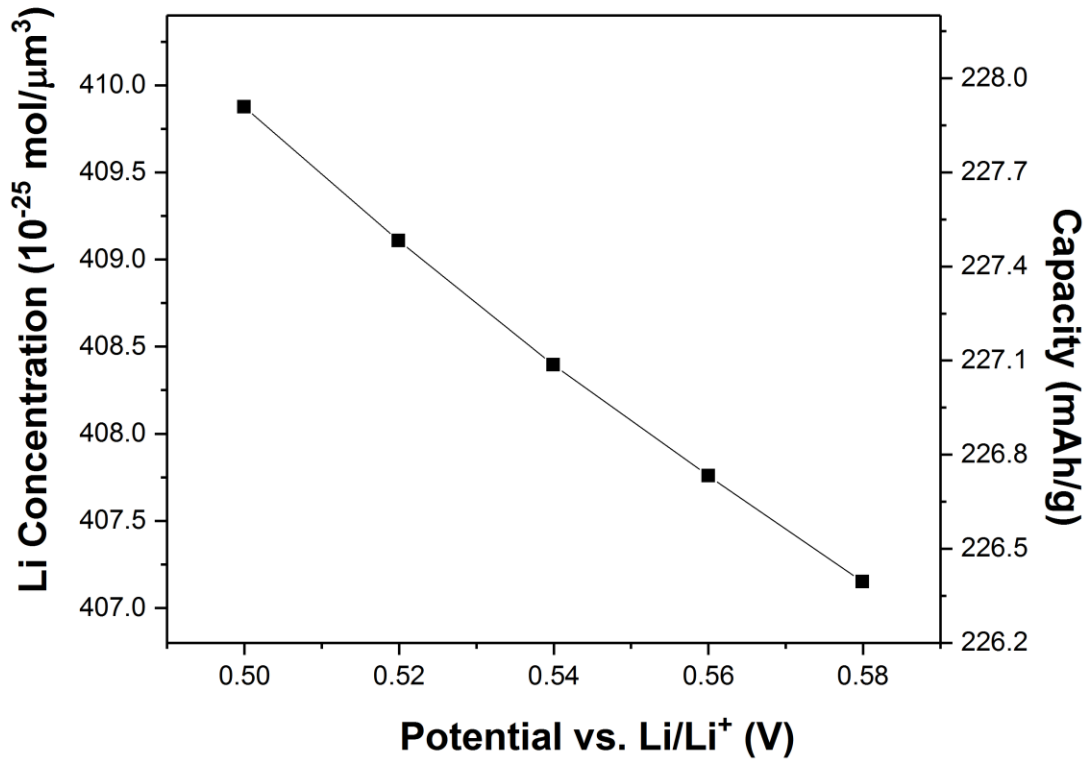


Figure 5.5. Surface Li concentration  $C_S$  in the LiSn phase at different applied potentials.

### 5.3. Kinetic model of two moving boundaries

In this section, we extend the kinetic model and the finite-difference calculation of a single moving boundary discussed in chapter 4 to the configuration of two moving boundaries.

#### 5.3.1 Initial condition

Two initial conditions are considered as described below to account the different experimental conditions used in this chapter. In the first case that corresponds to Experiment [ii], in which the potential directly changes to a value which activates both

$\text{Li}_2\text{Sn}_5$  ( $\beta$ ) and  $\text{LiSn}$  ( $\gamma$ ) phases from the Sn ( $\alpha$ ) anode surface simultaneously. A schematic plot for this case is shown in Fig. 5.6.

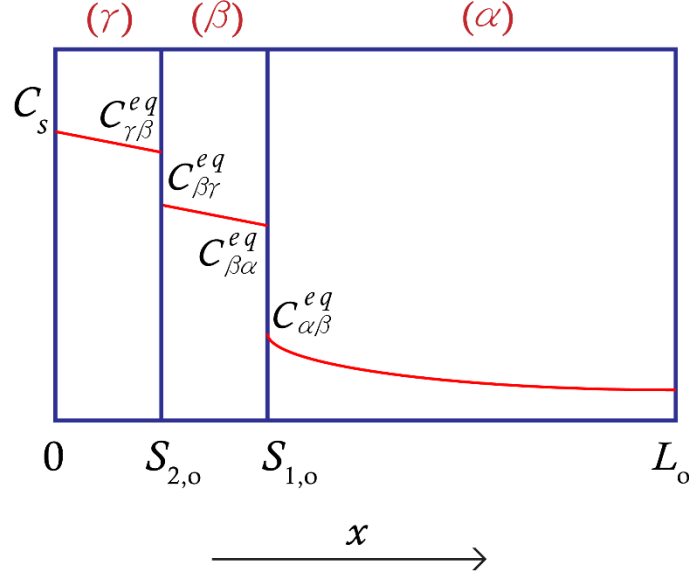


**Figure 5.6.** Schematic plot of initial concentration profile for Experiment [ii], in which both  $\text{Li}_2\text{Sn}_5$  and  $\text{LiSn}$  phases simultaneously grow from the anode surface.

As the potential is changed below the threshold of phase transformation, a higher Li concentration is established at the anode surface ( $x = 0$ ), which activates the nucleation of both  $\beta$  and  $\gamma$  phases.  $L_0$  is the original thickness of the Sn anode. Here, we assume that the nucleation happens within a thin nucleation region near the anode surface, where the  $\beta$  and  $\gamma$  phases nucleate and grow. At the same time, Li can diffuse and accumulate in the  $\alpha$  phase. At the end of nucleation, a continuous  $\gamma$  phase layer is formed at  $0 < x < S_{2,0}$ , and a continuous  $\beta$  phase layer is formed at  $S_{2,0} < x < S_{1,0}$ . Thus, the initial positions of the  $\alpha/\beta$  phase boundaries (interface  $S_1$ ) and the  $\beta/\gamma$  phase boundary (interface  $S_2$ ) are at  $x = S_{1,0}$  and  $x = S_{2,0}$  respectively. As shown in Fig. 5.6, the Li concentration profiles in  $\beta$  and  $\gamma$  phases are assumed to be linear with the equilibrium

concentrations ( $C_{\beta\alpha}^{eq}$ ,  $C_{\beta\gamma}^{eq}$  and  $C_{\gamma\beta}^{eq}$ ) and the surface Li concentration  $C_s$ . Here,  $C_{\beta\alpha}^{eq}$  is the stoichiometric Li concentration of  $\beta$  phase;  $C_{\beta\gamma}^{eq}$  is the Li solubility in  $\beta$  phase;  $C_{\gamma\beta}^{eq}$  is considered as the stoichiometric Li concentration of  $\gamma$  phase and  $C_{\alpha\beta}^{eq}$  is the Li solubility in  $\alpha$  phase. The accumulated Li concentration in Sn phase during nucleation can be obtained by the solution of 1-D diffusion shown in Eq. (5.2) as discussed in section 4.1.3.

$$\theta(\xi, \tau) = \sum_{n=0}^{\infty} \frac{4}{(2n+1)\pi} \frac{\sin(2n+1)\pi\xi}{2} e^{-\frac{(2n+1)^2\pi^2}{4}\tau} \quad \{5.2\}$$

where  $\xi = x/L_0$  is the normalized position;  $\tau = D_\alpha t_o/L_0^2$  is the normalized time ( $D_\alpha$  is the Li diffusivity in Sn and  $t_o$  is the nucleation time);  $\theta = (C_\alpha - C_{\alpha\beta}^{eq})/(C_i - C_{\alpha\beta}^{eq})$  is the normalized Li concentration. The resulting Li concentration profile is used as the initial condition in the numerical solution for analysis of Experiment [ii].

The other case corresponds to the Experiment [i], in which the  $\text{Li}_2\text{Sn}_5$  ( $\beta$ ) is grown during the first state of lithiation and then the potential is changed to activate the LiSn ( $\gamma$ ) phase in the second state. A schematic plot for each stage in this case is shown in Fig. 5.7.

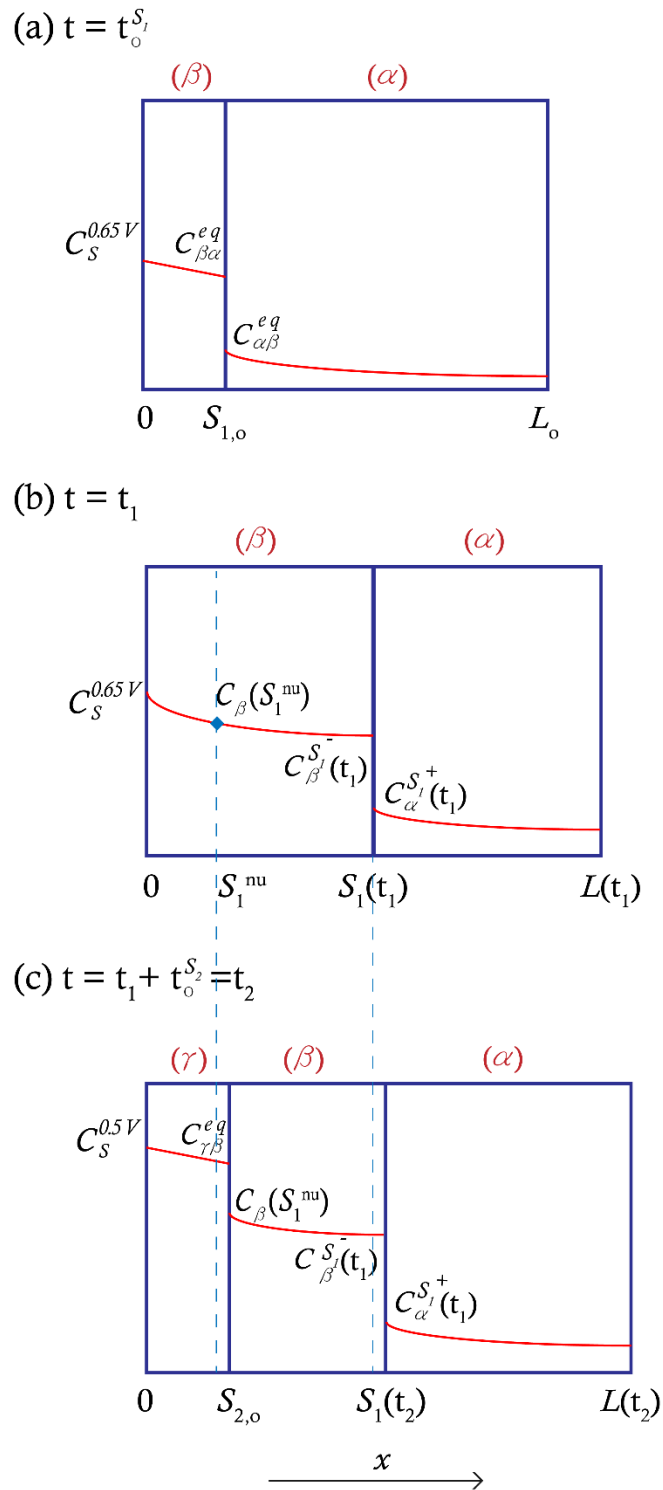


**Figure 5.7.** Schematic plots of concentration profile for the Experiment [1]: (a) the initial condition of lithiation at 0.65 V, (b) the resulting concentration at the end of lithiation at 0.65 V, (c) the initial condition of the subsequent lithiation at 0.5 V. The dash lines indicate the redefinition of interfaces induced by the nucleation of the  $\gamma$  phase at the surface.

In the first stage, where the  $\beta$  phase grows, there is only one moving boundary. The initial condition for this state is shown in Fig. 5.7a, in which the concentration in the  $\beta$  phase is assumed to be linear with the surface Li concentration  $C_S^{0.65V}$  and the equilibrium concentration at the interface  $C_{\beta\alpha}^{eq}$ . The concentration in  $\alpha$  phase is obtained by Eq. (5.2) with the nucleation time  $t_0^{S_1}$ . Then the evolution of Li concentration and phase transformation is calculated by the finite-difference method for single moving boundary as described in chapter 4.

At the end of potential holding at 0.65 V ( $t = t_1$ ), the  $\alpha/\beta$  phase boundary reaches  $x = S_1(t_1)$ , and the total film thickness expands to  $x = L(t_1)$  as shown in Fig. 5.7b. The Li concentrations at the phase boundary are represented as  $C_{\beta}^{S_1^-}(t_1)$  and  $C_{\alpha}^{S_1^+}(t_1)$ .

In the second state, the potential is changed to 0.5 V, where the LiSn ( $\gamma$ ) phase nucleates at the surface. Here, we assume at the end of the nucleation ( $t = t_1 + t_0^{S_2} = t_2$ ), a thin layer of  $\beta$  phase at the surface ( $0 \leq x \leq S_1^{nu}$  in Fig. 5.7b) has been transformed into the  $\gamma$  phase ( $0 \leq x \leq S_{2,o}$  in Fig. 5.7c). Since the  $\beta - \gamma$  phase transformation involves a volume expansion,  $S_{2,o}$  is larger than  $S_1^{nu}$ , and can be represented as  $S_{2,o} = r_{\beta\gamma} S_1^{nu}$ .  $r_{\beta\gamma}$  is the volume expansion ratio of  $\gamma$  with respect to  $\beta$  phase, and its value is 1.23 for the  $\text{Li}_2\text{Sn}_5$ -LiSn phase transformation. Similarly, the positions of  $S_1(t_1)$  and  $L(t_1)$  are redefined as  $S_1(t_2)$  and  $L(t_2)$  to account for the volume expansion. The Li concentration profile in the nucleation region  $0 \leq x \leq S_{2,o}$  is assumed to be linear with the surface Li concentration at 0.5 V  $C_S^{0.5V}$  and the equilibrium concentration  $C_{\gamma\beta}^{eq}$ . The Li concentration in the  $\beta$  phase is imported from the concentration profile at  $t = t_1$ , in

which  $C_\beta(S_1^{nu})$  is the concentration at the  $\beta/\gamma$  phase boundary in  $\beta$  phase. The Li concentration in the  $\alpha$  phase is also imported from profile at  $t = t_1$ . The resulting profile is the used as the initial condition for numerical analysis of the Experiment [i]. The two initial conditions discussed here are subsequently calculated by the finite-difference method in section 5.3.3.

### 5.3.2 Modeling configuration: governing equations and boundary conditions

When the nucleation is finished, there are three phase regions with two phase boundaries in the anode. During the following lithiation, many Li atoms that enter the anode are consumed by advancing at the Sn/Li<sub>2</sub>Sn<sub>5</sub> phase boundary. If the Sn/Li<sub>2</sub>Sn<sub>5</sub> phase boundary doesn't move fast enough, some Li can diffuse toward the other interface, the Li<sub>2</sub>Sn<sub>5</sub>/LiSn phase boundary resulting in its progression. Similarly, if the Li atoms are not fully consumed at the Li<sub>2</sub>Sn<sub>5</sub>/LiSn phase boundary, some excess Li can diffuse into the Sn phase. The continuum kinetic model applied here includes the Li diffusion in the three phase layers and the reactions at the two moving phase boundaries. A schematic plot of the kinetic modeling configuration is shown in Fig. 5.8.

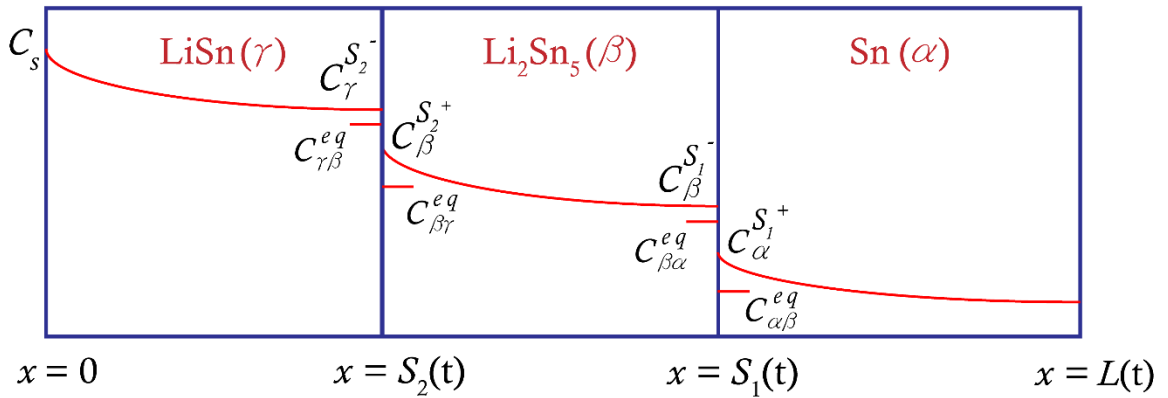


**Figure 5.8.** Schematic plot of the kinetic model of two moving boundaries.

The entirety of Sn anode is defined as  $0 \leq x \leq L(t)$ , where the electrolyte/anode interface (i.e., anode surface) is located at  $x = 0$ , and the anode/substrate interface is at  $x = L(t)$ .  $L(t)$  is a function of time due to the volume expansions induced by the phase transformations. The Sn ( $\alpha$ ) phase,  $\text{Li}_2\text{Sn}_5$  ( $\beta$ ) phase and LiSn ( $\gamma$ ) phases in the anode are separated by the two moving interfaces,  $S_1$  (the Sn/ $\text{Li}_2\text{Sn}_5$  phase boundary) and  $S_2$  (the  $\text{Li}_2\text{Sn}_5$ /LiSn phase boundary).

The governing equations are:

$$(g1) \quad \frac{\partial c_\gamma(x,t)}{\partial t} = D_\gamma \frac{\partial^2 c_\gamma(x,t)}{\partial x^2}, \text{ for LiSn } (\gamma \text{ phase}) \text{ region, } 0 \leq x \leq S_2(t)$$

$$(g2) \quad \frac{\partial c_\beta(x,t)}{\partial t} = D_\beta \frac{\partial^2 c_\beta(x,t)}{\partial x^2}, \text{ for } \text{Li}_2\text{Sn}_5 \text{ } (\beta \text{ phase}) \text{ region, } S_2(t) \leq x \leq S_1(t)$$

$$(g3) \quad \frac{\partial c_\alpha(x,t)}{\partial t} = D_\alpha \frac{\partial^2 c_\alpha(x,t)}{\partial x^2}, \text{ for Sn } (\alpha \text{ phase}) \text{ region, } S_1(t) \leq x \leq L(t)$$

$$(g4) \quad D_\gamma \frac{\partial c_\gamma^{S_2^-}}{\partial x} - D_\beta \frac{\partial c_\beta^{S_2^+}}{\partial x} = (C_\beta^{S_2^+} - C_\gamma^{S_2^-}) v_{S_2}, \text{ for } x = S_2(t)$$

$$(g5) \quad D_\beta \frac{\partial c_\beta^{S_1^-}}{\partial x} - D_\alpha \frac{\partial c_\alpha^{S_1^+}}{\partial x} = (C_\alpha^{S_1^+} - C_\beta^{S_1^-}) v_{S_1}, \text{ for } x = S_1(t)$$

where  $D_\alpha$ ,  $D_\beta$ , and  $D_\gamma$  are the Li diffusivity in Sn,  $\text{Li}_2\text{Sn}_5$ , and LiSn, respectively.  $v_{S_1}$  and  $v_{S_2}$  are the velocities of the phase boundaries. The subscripts represent the corresponding phases. Here, the Li diffusion in the three layers is assumed to be described by the Fick's second law as shown in the governing equations (g1-g3). In the governing equation (g4), the velocity of  $\text{Li}_2\text{Sn}_5$ /LiSn phase boundary  $v_{S_2}$  is related to the difference of Li flux across the phase boundary (i.e., interface  $S_2$ ).  $C_\beta^{S_2^+}$  and  $C_\gamma^{S_2^-}$ , respectively,

denote the Li concentrations at  $\text{Li}_2\text{Sn}_5/\text{LiSn}$  phase boundary in the  $\text{Li}_2\text{Sn}_5$  phase and the  $\text{LiSn}$  phase. A similar expression is seen in the governing equation (g5) for the interface  $S_1$ . In other words, the governing equations (g4 and g5) are the mass conservation of Li at the phase boundaries.

The boundary conditions are selected to agree with the experimental conditions. Note that the influence of SEI on the electrochemical processes is not included in the modeling. The boundary conditions are:

$$(b1) \quad C_\gamma(0, t) = C_s$$

$$(b2) \quad \frac{\partial C_\alpha(L(t), t)}{\partial x} = 0$$

$$(b3) \quad C_\alpha^{S_1^+} = C_{\alpha\beta}^{eq} + (C_\beta^{S_1^-} - C_{\beta\alpha}^{eq})$$

$$(b4) \quad C_\beta^{S_2^+} = C_{\beta\gamma}^{eq} + (C_\gamma^{S_2^-} - C_{\gamma\beta}^{eq})$$

$$(b5) \quad v_{S_1} = K_{\alpha\beta}(C_\beta^{S_1^-} - C_{\beta\alpha}^{eq})$$

$$(b6) \quad v_{S_2} = K_{\beta\gamma}(C_\gamma^{S_2^-} - C_{\gamma\beta}^{eq})$$

As described in section 5.1.2, the phase transformations were conducted by potentiostatic lithiation. Therefore, in boundary condition (b1), it is assumed that the constant applied potential corresponds to a constant Li concentration  $C_s$  at  $x = 0$ . The fused-silica substrate is assumed to be impervious to Li; thus, in boundary condition (b2), the Li flux at the anode/substrate interface,  $x = L(t)$ , is set to zero.

When the system is at equilibrium, the phase boundaries (interfaces  $S_1$  and  $S_2$ ) remains stationary and the Li concentrations at the interfaces are at the equilibrium values.

Thus, the chemical potential of Li across each interface is the same (i.e.,  $\mu_{\beta\alpha, Li}^{eq} = \mu_{\alpha\beta, Li}^{eq}$  for interface  $S_1$ ;  $\mu_{\gamma\beta, Li}^{eq} = \mu_{\beta\gamma, Li}^{eq}$  for interface  $S_2$ ).<sup>5</sup> In contrast, when the phase boundaries are moving, the Li concentrations at the phase boundaries are expected to deviate from their equilibrium values. Therefore, in Fig. 5.8, the concentrations at the interfaces  $S_1$  and  $S_2$  are higher than the equilibrium values. As discussed in section 4.2.2, we consider a chemical potential discontinuity ( $\Delta\mu^{S_1}$  or  $\Delta\mu^{S_2}$ ) across each moving boundary, and it is assumed can be represented as

$$\Delta\mu^{S_1} = \mu_{\beta\alpha, Li}^{eq} + kT \ln \varphi_\beta \delta C_{\beta, Li}^{S_1^-} - \mu_{\alpha\beta, Li}^{eq} - kT \ln \varphi_\alpha \delta C_{\alpha, Li}^{S_1^+} \quad \{5.3\}$$

and

$$\Delta\mu^{S_2} = \mu_{\gamma\beta, Li}^{eq} + kT \ln \varphi_\gamma \delta C_{\gamma, Li}^{S_2^-} - \mu_{\beta\gamma, Li}^{eq} - kT \ln \varphi_\beta \delta C_{\beta, Li}^{S_2^+} \quad \{5.4\}$$

where  $\varphi_\alpha$ ,  $\varphi_\beta$  and  $\varphi_\gamma$  are the activity coefficients, and the logarithmic terms include the deviations of chemical potential from the equilibrium values (i.e.,  $\delta C_{\alpha, Li}^{S_1^+} = C_{\alpha}^{S_1^+} - C_{\alpha\beta}^{eq}$ ,  $\delta C_{\beta, Li}^{S_1^-} = C_{\beta}^{S_1^-} - C_{\beta\alpha}^{eq}$ ,  $\delta C_{\beta, Li}^{S_2^+} = C_{\beta}^{S_2^+} - C_{\beta\gamma}^{eq}$ , and  $\delta C_{\gamma, Li}^{S_2^-} = C_{\gamma}^{S_2^-} - C_{\gamma\beta}^{eq}$ ). By eliminating the equilibrium chemical potentials, Eqs. (5.3) and (5.4) can be represented as

$$\frac{\varphi_\alpha}{\varphi_\beta} \exp\left(\frac{\Delta\mu^{S_1}}{kT}\right) = \frac{\delta C_{\beta, Li}^{S_1^-}}{\delta C_{\alpha, Li}^{S_1^+}} = \frac{C_{\beta}^{S_1^-} - C_{\beta\alpha}^{eq}}{C_{\alpha}^{S_1^+} - C_{\alpha\beta}^{eq}} \quad \{5.5\}$$

and

$$\frac{\varphi_{\beta}}{\varphi_{\gamma}} \exp\left(\frac{\Delta\mu^{S_2}}{kT}\right) = \frac{\delta C_{\gamma, Li}^{S_2^-}}{\delta C_{\beta, Li}^{S_2^+}} = \frac{C_{\gamma}^{S_2^-} - C_{\gamma\beta}^{eq}}{C_{\beta}^{S_2^+} - C_{\beta\gamma}^{eq}} \quad \{5.6\}.$$

According to the Li-Sn phase diagram,<sup>6</sup> the phases studied here (i.e., Sn, Li<sub>2</sub>Sn<sub>5</sub> and LiSn phases) have limited Li solubility, so the non-ideal behavior of Li in these phases are assumed to be similar to dilute solutions (i.e.,  $\frac{\varphi_{\alpha}}{\varphi_{\beta}} \sim 1$  and  $\frac{\varphi_{\beta}}{\varphi_{\gamma}} \sim 1$ ). In addition, the Li diffusion across the phase boundaries is assumed to be fast and the thickness of the interfaces is thin enough to be negligible, which leads to  $\Delta\mu^{S_1} \sim 0$  and  $\Delta\mu^{S_2} \sim 0$ .<sup>7</sup> Therefore, the left-hand side of Eqs. (5.5) and (5.6) can be approximated to be one, and result in the boundary conditions (b3) and (b4).

While the phase boundaries are moving, the deviation from the equilibrium Li concentration (i.e., supersaturation of Li) at the phase boundaries are essentially the driving force for the phase transformations. Therefore, the velocities of the phase boundaries  $v_{S_1}$  and  $v_{S_2}$  can be represented with the reaction rate coefficients ( $K_{\alpha\beta}$  and  $K_{\beta\gamma}$  respectively) as shown in boundary conditions (b5) and (b6). Similar to the discussion in section 4.2.2, the reaction rate coefficients determine the mobility of the phase boundaries. For a larger reaction rate coefficient, the corresponding phase boundary moves faster with a specific supersaturation at the phase boundary. If the reaction coefficient approaches infinity, the movement of the phase boundary depends only on the diffusion near the phase boundary, so called the diffusion-controlled case. Whereas, if the reaction coefficient approach zero, the movement of the boundary is only determined by the reaction at the phase boundary and is called the interface-controlled case. In general, the reaction rate coefficient has a finite value, and the phase boundary propagation is

considered in a mixed mode. In the following section 5.3.3, the finite-difference method is utilized to calculate the phase boundary movement with the governing equations and boundary conditions discussed above.

### 5.3.3 Finite-difference analysis

The finite-difference calculation employed to simulate the propagation of two moving boundaries is based on the method developed by J. Crank.<sup>8,9</sup> The calculation also involves the Forward-Time Central-Space method with Lagrangian interpolation and the front-tracking method with a fixed grid. Since the derivation is similar to the case of single moving boundary problem in section 4.3, it is abbreviated in this section.

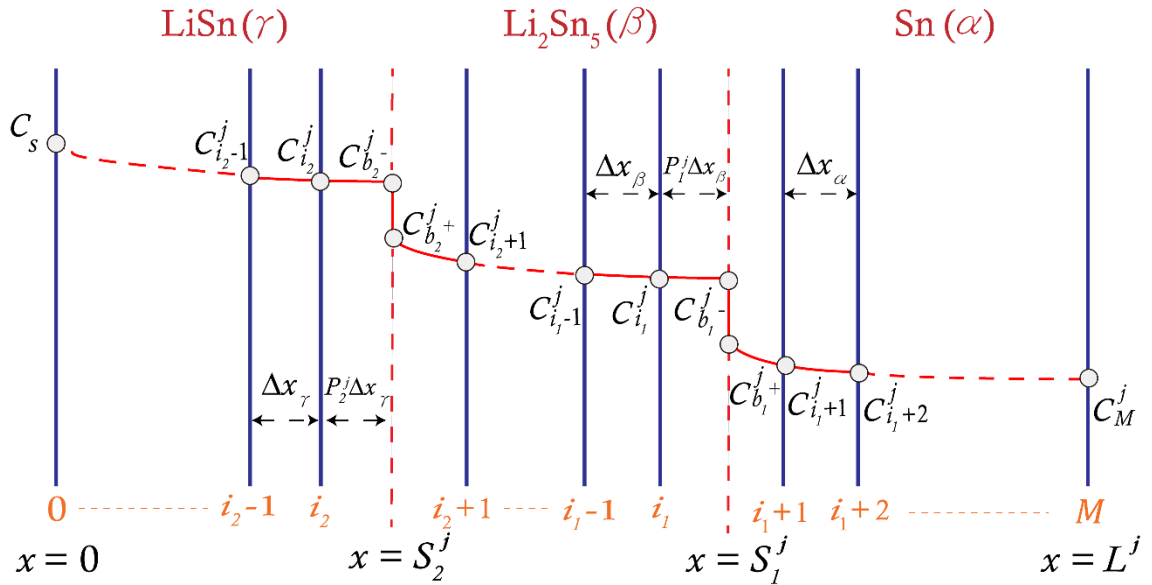


**Figure 5.9.** Schematic plot of the finite-difference framework with two moving boundaries.

The framework of the finite-difference calculation consisting of two moving boundaries is shown in Fig. 5.9. The entire simulation domain is subdivided into  $M$  intervals, and is partitioned into three phases by the interfaces  $S_1$  and  $S_2$ . For the

concentration at each nodal point, the superscript denotes the time step, and the subscript denotes the nodal point.  $\Delta x_\alpha, \Delta x_\beta$ , and  $\Delta x_\gamma$  are the grid spacing of the corresponding phases. To account for the volume expansion induced by the phase transformations,  $\Delta x_\alpha, \Delta x_\beta$ , and  $\Delta x_\gamma$  can have different values. Here, the grid spacing of  $\alpha$  phase is defined as  $\Delta x_\alpha = \frac{L_o}{M}$ , where  $L_o$  is the original thickness of Sn anode. The other grid spacing are defined accordingly as  $\Delta x_\beta = r_{\alpha\beta}\Delta x_\alpha$  and  $\Delta x_\gamma = r_{\alpha\gamma}\Delta x_\alpha$ , where  $r_{\alpha\beta}$  is the volume expansion of  $\beta$  phase relative to  $\alpha$  phase and  $r_{\alpha\gamma}$  is the volume expansion of  $\gamma$  phase relative to  $\alpha$  phase. The nodal points in front of the phase boundaries  $S_1$  and  $S_2$  are defined as  $i_1$  and  $i_2$  respectively. When the interface  $S_1$  (or  $S_2$ ) progresses across a grid and moves into the next interval, the  $i_1$  (or  $i_2$ ) node is updated accordingly in the calculation.

For the method involving the central difference in space and the forward Euler method in time, the discretized form of the time-dependent diffusion described by the Fick's second law (governing equations g1-g3) can be represented as

$$\frac{C_n^{j+1} - C_n^j}{\Delta t} = D_k \frac{(C_{n-1}^j - 2C_n^j + C_{n+1}^j)}{\Delta x_k^2} \quad \{5.7\}$$

where  $k$  denotes the phase ( $\alpha$ ,  $\beta$  or  $\gamma$ ). As shown in Eq. (5.7), each phase has its specific Li diffusivity  $D_k$  and grid spacing  $\Delta x_k$ . Eq. (5.7) can be rearranged into

$$C_n^{j+1} = C_n^j + \frac{D_k \Delta t}{\Delta x_k^2} (C_{n-1}^j - 2C_n^j + C_{n+1}^j) \quad \{5.8\}.$$

Eq. (5.8) can be used to calculate the concentration at a general nodal point at the next time step  $j+1$  with the concentrations at neighboring positions at time step  $j$ . For the nodal points at the edges of the framework ( $n = 0$  or  $M$ ), the concentrations can be obtained by applying the boundary conditions (b1) and (b2). For the surface node ( $n = 0$ ), the concentration is assumed to be remained at the constant value  $C_S$  (boundary condition b1). For the  $M^{th}$  node, Eq. (5.8) can be modified to agree with the boundary condition (b2), and concentration is represented as

$$C_M^{j+1} = C_M^j + \frac{2D_\alpha \Delta t}{\Delta x_\alpha^2} (C_{M-1}^j - C_M^j) \quad \{5.9\}.$$

The position of interface  $S_2$  at time step  $j$  is

$$S_2^j = (i_2 + P_2^j) \Delta x_\gamma \quad \{5.10\}$$

where  $P_2^j$  is the progression factor indicating the position of interface  $S_2$  in the present  $(i_2 + 1)^{th}$  interval and has a value between 0 and 1. The position of interface  $S_1$  is

$$S_1^j = S_2^j + (i_1 - i_2 + P_1^j - P_2^j) \Delta x_\beta = (i_2 + P_2^j) (\Delta x_\gamma - \Delta x_\beta) + (i_1 + P_1^j) \Delta x_\beta \quad \{5.11\}$$

where  $P_1^j$  is the progression factor for interface  $S_1$ . Eq. (5.11) shows that the position of interface  $S_1$  can be influenced by the movement of interface  $S_2$ , due to the volume

expansion of the phase transformations. Since the distance between the phase boundaries and the grids are uneven, Lagrangian interpolation is performed to calculate the concentration at the nodal points located near the phase boundaries (i.e.,  $i_1$ ,  $i_1 + 1$ ,  $i_2$  and  $i_2 + 1$ ). As the results, the derivatives of concentration with respect to position can be obtained. The first derivatives at the phase boundaries are:

$$\frac{\partial C}{\partial x} = \frac{1}{\Delta x_\alpha} \left( \frac{2P_1^j - 3}{(1-P_1^j)(2-P_1^j)} C_{b_1^+}^j + \frac{(2-P_1^j)}{(1-P_1^j)} C_{i_1+1}^j - \frac{(1-P_1^j)}{(2-P_1^j)} C_{i_1+2}^j \right), x = S_1^j \text{ in } \alpha \text{ phase} \quad \{5.12\}$$

and

$$\frac{\partial C}{\partial x} = \frac{1}{\Delta x_\beta} \left( \frac{P_1^j}{P_1^j+1} C_{i_1-1}^j - \frac{(P_1^j+1)}{P_1^j} C_{i_1}^j + \frac{(2P_1^j+1)}{P_1^j(P_1^j+1)} C_{b_1^-}^j \right), x = S_1^j \text{ in } \beta \text{ phase} \quad \{5.13\}$$

and

$$\frac{\partial C}{\partial x} = \frac{1}{\Delta x_\beta} \left( \frac{2P_2^j - 3}{(1-P_2^j)(2-P_2^j)} C_{b_1^+}^j + \frac{(2-P_2^j)}{(1-P_2^j)} C_{i_2+1}^j - \frac{(1-P_2^j)}{(2-P_2^j)} C_{i_2+2}^j \right), x = S_2^j \text{ in } \beta \text{ phase} \quad \{5.14\}$$

and

$$\frac{\partial C}{\partial x} = \frac{1}{\Delta x_\gamma} \left( \frac{P_2^j}{P_2^j+1} C_{i_2-1}^j - \frac{(P_2^j+1)}{P_2^j} C_{i_2}^j + \frac{(2P_2^j+1)}{P_2^j(P_2^j+1)} C_{b_2^-}^j \right), x = S_2^j \text{ in } \gamma \text{ phase} \quad \{5.15\}$$

where  $C_{b_2^-}^j$ ,  $C_{b_2^+}^j$ ,  $C_{b_1^-}^j$ , and  $C_{b_1^+}^j$  are the concentrations at the phase boundaries as shown

in Fig. 5.9. The second derivatives at the nodes near the phase boundaries are:

$$\frac{\partial^2 C}{\partial x^2} = \frac{2}{\Delta x_\alpha^2} \left( \frac{C_{b_1^+}^j}{(1-P_1^j)(2-P_1^j)} - \frac{C_{i_1+1}^j}{(1-P_1^j)} + \frac{C_{i_1+2}^j}{(2-P_1^j)} \right), \text{ for the } i_1 + 1 \text{ node in } \alpha \text{ phase} \quad \{5.16\}$$

and

$$\frac{\partial^2 C}{\partial x^2} = \frac{2}{\Delta x_\beta^2} \left( \frac{C_{i_1-1}^j}{P_1^{j+1}} - \frac{C_{i_1}^j}{P_1^j} + \frac{C_{b_1^-}^j}{P_1^j(P_1^{j+1})} \right), \text{ for the } i_1 \text{ node in } \beta \text{ phase} \quad \{5.17\}$$

and

$$\frac{\partial^2 C}{\partial x^2} = \frac{2}{\Delta x_\beta^2} \left( \frac{C_{b_2^+}^j}{(1-P_2^j)(2-P_2^j)} - \frac{C_{i_2+1}^j}{(1-P_2^j)} + \frac{C_{i_2+2}^j}{(2-P_2^j)} \right), \text{ for the } i_2 + 1 \text{ node in } \beta \text{ phase} \quad \{5.18\}$$

and

$$\frac{\partial^2 C}{\partial x^2} = \frac{2}{\Delta x_\gamma^2} \left( \frac{C_{i_2-1}^j}{P_2^{j+1}} - \frac{C_{i_2}^j}{P_2^j} + \frac{C_{b_2^-}^j}{P_2^j(P_2^{j+1})} \right), \text{ for the } i_2 \text{ node in } \gamma \text{ phase} \quad \{5.19\}.$$

These second derivatives are utilized with the Fick's second law (governing equations g1-g3) to obtain the concentrations at the  $i_1$ ,  $i_1 + 1$ ,  $i_2$  and  $i_2 + 1$  nodes. The concentration at the  $i_1 + 1$  node is

$$C_{i_1+1}^{j+1} = C_{i_1+1}^j + \frac{2D_\alpha \Delta t}{\Delta x_\alpha^2} \left( \frac{C_{b_1^+}^j}{(1-P_1^j)(2-P_1^j)} - \frac{C_{i_1+1}^j}{1-P_1^j} + \frac{C_{i_1+2}^j}{2-P_1^j} \right) \quad \{5.20\}$$

and for the  $i_1$  node,

$$C_{i_1}^{j+1} = C_{i_1}^j + \frac{2D_\beta \Delta t}{\Delta x_\beta^2} \left( \frac{C_{i_1-1}^j}{P_1^{j+1}} - \frac{C_{i_1}^j}{P_1^j} + \frac{C_{b_1^-}^j}{P_1^j(P_1^{j+1})} \right) \quad \{5.21\}$$

and for the  $i_2 + 1$  node,

$$C_{i_2+1}^{j+1} = C_{i_2+1}^j + \frac{2D_\beta \Delta t}{\Delta x_\beta^2} \left( \frac{C_{b_2^+}^j}{(1-P_2^j)(2-P_2^j)} - \frac{C_{i_2+1}^j}{1-P_2^j} + \frac{C_{i_2+2}^j}{2-P_2^j} \right) \quad \{5.22\}$$

and for the  $i_2$  node,

$$C_{i_2}^{j+1} = C_{i_2}^j + \frac{2D_\gamma \Delta t}{\Delta x_\gamma^2} \left( \frac{C_{i_2-1}^j}{P_2^j + 1} - \frac{C_{i_2}^j}{P_2^j} + \frac{C_{b_2^-}^j}{P_2^j(P_2^j + 1)} \right) \quad \{5.23\}.$$

The first derivatives in Eqs. (5.12)-(5.15) can be utilized to obtain the concentrations at the phase boundaries (i.e.,  $C_{b_2^-}^j$ ,  $C_{b_2^+}^j$ ,  $C_{b_1^-}^j$ , and  $C_{b_1^+}^j$ ). For the interface  $S_1$ , Eqs. (5.12) and (5.13), and the governing equation (g5) are applied, leading to

$$D_\beta \left[ \frac{1}{\Delta x_\beta} \left( \frac{P_1^j C_{i_1-1}^j}{P_1^j+1} - \frac{(P_1^j+1)C_{i_1}^j}{P_1^j} + \frac{(2P_1^j+1)C_{b_1^-}^j}{P_1^j(P_1^j+1)} \right) \right] \dots$$

$$-D_\alpha \left[ \frac{1}{\Delta x_\alpha} \left( \frac{(2P_1^j-3)C_{b_1^+}^j}{(1-P_1^j)(2-P_1^j)} + \frac{(2-P_1^j)C_{i_1+1}^j}{1-P_1^j} - \frac{(1-P_1^j)C_{i_1+2}^j}{2-P_1^j} \right) \right] = (C_{b_1^+}^j - C_{b_1^-}^j) v_{S_1} \quad \{5.24\}$$

where  $(C_{b_1^+}^j - C_{b_1^-}^j)$  can be substituted with the equilibrium concentrations  $(C_{\alpha\beta}^{eq} - C_{\beta\alpha}^{eq})$  by the boundary condition (b3). Also, the velocity  $v_{S_1}$  can be substituted with  $K_{\alpha\beta}(C_{b_1^-}^j - C_{\beta\alpha}^{eq})$  by the boundary condition (b5). Thus, Eq. (5.24), can be rewritten for the concentration  $C_{b_1^-}^j$  as

$$C_{b_1^-}^j = \frac{\frac{D_\beta}{\Delta x_\beta} \left[ \frac{P_1^j C_{i_1-1}^j}{P_1^{j+1}} - \frac{(P_1^{j+1}) C_{i_1}^j}{P_1^j} \right] - \frac{D_\alpha}{\Delta x_\alpha} \left[ \frac{(2P_1^j-3)(C_{\alpha\beta}^{eq} - C_{\beta\alpha}^{eq})}{(1-P_1^j)(2-P_1^j)} + \frac{(2-P_1^j) C_{i_1+1}^j}{1-P_1^j} - \frac{(1-P_1^j) C_{i_1+2}^j}{2-P_1^j} \right] + K_{\alpha\beta} C_{\beta\alpha}^{eq} (C_{\alpha\beta}^{eq} - C_{\beta\alpha}^{eq})}{\frac{D_\alpha}{\Delta x_\alpha} \left[ \frac{(2P_1^j-3)}{(1-P_1^j)(2-P_1^j)} \right] - \frac{D_\beta}{\Delta x_\beta} \left[ \frac{(2P_1^j+1)}{P_1^j(P_1^{j+1})} \right] + K_{\alpha\beta} (C_{\alpha\beta}^{eq} - C_{\beta\alpha}^{eq})} \quad \{5.25\}.$$

Since all the concentrations in Eq. (5.25) are at the same time step  $j$ . It can be rewritten for the time step  $j+1$  as

$$C_{b_1^-}^{j+1} = \frac{\frac{D_\beta}{\Delta x_\beta} \left[ \frac{P_1^{j+1} C_{i_1-1}^{j+1}}{P_1^{j+1+1}} - \frac{(P_1^{j+1+1}) C_{i_1}^{j+1}}{P_1^{j+1}} \right] - \frac{D_\alpha}{\Delta x_\alpha} \left[ \frac{(2P_1^{j+1}-3)(C_{\alpha\beta}^{eq} - C_{\beta\alpha}^{eq})}{(1-P_1^{j+1})(2-P_1^{j+1})} + \frac{(2-P_1^{j+1}) C_{i_1+1}^{j+1}}{1-P_1^{j+1}} - \frac{(1-P_1^{j+1}) C_{i_1+2}^{j+1}}{2-P_1^{j+1}} \right] + K_{\alpha\beta} C_{\beta\alpha}^{eq} (C_{\alpha\beta}^{eq} - C_{\beta\alpha}^{eq})}{\frac{D_\alpha}{\Delta x_\alpha} \left[ \frac{(2P_1^{j+1}-3)}{(1-P_1^{j+1})(2-P_1^{j+1})} \right] - \frac{D_\beta}{\Delta x_\beta} \left[ \frac{(2P_1^{j+1}+1)}{P_1^{j+1}(P_1^{j+1+1})} \right] + K_{\alpha\beta} (C_{\alpha\beta}^{eq} - C_{\beta\alpha}^{eq})}$$

{5.26}

where  $P_1^{j+1}$  is

$$P_1^{j+1} = P_1^j + \frac{\Delta t}{\Delta x_\alpha} K_{\alpha\beta} (C_{b_1^-}^j - C_{\beta\alpha}^{eq}) \quad \{5.27\}$$

Eq. (5.26) can be used to calculate the concentration  $C_{b_1^-}^{j+1}$  if  $P_1^{j+1} < 1$ . Then, by using the boundary condition (b3), the concentration on the other side of the phase boundary  $C_{b_1^+}^{j+1}$  can be obtained.

If  $P_1^{j+1} > 1$ , the phase boundary will move into the next interval in time step  $j+1$ , and the  $i_1$  node have to be updated as  $i_1^{j+1} = i_1^j + 1$ . Thus, the terms  $C_{i_1}^{j+1}$  and  $C_{i_1+1}^{j+1}$  in Eq. (5.26) need to be substituted by the Lagrangian interpolation:

$$C_{i_1}^{j+1} = \frac{-P_1^{j+1}}{2 + P_1^{j+1}} C_{i_1-2}^{j+1} + \frac{2P_1^{j+1}}{1 + P_1^{j+1}} C_{i_1-1}^{j+1} + \frac{2}{(2 + P_1^{j+1})(1 + P_1^{j+1})} C_{b_1^-}^{j+1} \quad \{5.28\}$$

and

$$C_{i_1+1}^{j+1} = \frac{2}{(P_1^{j+1} - 2)(P_1^{j+1} - 3)} C_{b_1^+}^{j+1} + \frac{2 - 2P_1^{j+1}}{2 - P_1^{j+1}} C_{i_1+2}^{j+1} + \frac{P_1^{j+1} - 1}{3 - P_1^{j+1}} C_{i_1+3}^{j+1} \quad \{5.29\}.$$

Then the  $C_{b_1^-}^{j+1}$  becomes

$$C_{b_1^-}^{j+1} = \frac{\frac{D_\beta}{\Delta x_\beta} \left[ \frac{P_1^{j+1+1} C_{i_1-2}^{j+1}}{P_1^{j+1+2}} - \frac{P_1^{j+1+2} C_{i_1-1}^{j+1}}{P_1^{j+1+1}} \right] - \frac{D_\alpha}{\Delta x_\alpha} \left[ \frac{\frac{(2P_1^{j+1}-3)(C_{\alpha\beta}^{eq} - C_{\beta\alpha}^{eq})}{(1-P_1^{j+1})(2-P_1^{j+1})} + \frac{2(C_{\alpha\beta}^{eq} - C_{\beta\alpha}^{eq})}{(1-P_1^{j+1})(3-P_1^{j+1})} \dots}{\frac{(3-P_1^{j+1})C_{i_1+2}^{j+1}}{2-P_1^{j+1}} + \frac{(P_1^{j+1}-2)C_{i_1+3}^{j+1}}{3-P_1^{j+1}}} \right] + K_{\alpha\beta} C_{\beta\alpha}^{eq} (C_{\alpha\beta}^{eq} - C_{\beta\alpha}^{eq})}{\frac{D_\alpha}{\Delta x_\alpha} \left[ \frac{(2P_1^{j+1}-3)}{(1-P_1^{j+1})(2-P_1^{j+1})} + \frac{2}{(1-P_1^{j+1})(3-P_1^{j+1})} \right] - \frac{D_\beta}{\Delta x_\beta} \left[ \frac{(2P_1^{j+1}+1)}{P_1^{j+1}(P_1^{j+1}+1)} - \frac{2}{P_1^{j+1}(P_1^{j+1}+2)} \right] + K_{\alpha\beta} (C_{\alpha\beta}^{eq} - C_{\beta\alpha}^{eq})}$$

{5.30}

At last, the progression factor is redefined as  $P_1^{j+1'} = P_1^{j+1} - 1$ , and used to update the concentrations at  $i_1$  and  $i_1 + 1$  nodes to complete the calculations for the next time step  $j+1$ .

A similar procedure can be performed for the concentrations near and at the interface  $S_2$ .

The progression factor of interface  $S_2$  is

$$P_2^{j+1} = P_2^j + \frac{\Delta t}{\Delta x_\beta} K_{\beta\gamma} (C_{b_2^-}^j - C_{\gamma\beta}^{eq}) \quad \{5.31\}.$$

If  $P_2^{j+1} < 1$ , the concentration at the phase boundary is

$$C_{b_2^-}^{j+1} =$$

$$\frac{D_\gamma \left[ \frac{P_2^{j+1} C_{i_2-1}^{j+1}}{P_2^{j+1}+1} - \frac{(P_2^{j+1}+1) C_{i_2}^{j+1}}{P_2^{j+1}} \right] - \frac{D_\beta \left[ \frac{(2P_2^{j+1}-3)(C_{\beta\gamma}^{eq} - C_{\gamma\beta}^{eq})}{(1-P_2^{j+1})(2-P_2^{j+1})} + \frac{(2-P_2^{j+1}) C_{i_2+1}^{j+1}}{1-P_2^{j+1}} - \frac{(1-P_2^{j+1}) C_{i_2+2}^{j+1}}{2-P_2^{j+1}} \right] + K_{\beta\gamma} C_{\gamma\beta}^{eq} (C_{\beta\gamma}^{eq} - C_{\gamma\beta}^{eq})}{\Delta x_\gamma \left[ \frac{P_2^{j+1}+1}{P_2^{j+1}+1} - \frac{P_2^{j+1}}{P_2^{j+1}} \right] - \frac{D_\beta \left[ \frac{(2P_2^{j+1}-3)}{(1-P_2^{j+1})(2-P_2^{j+1})} \right] - \frac{D_\gamma \left[ \frac{(2P_2^{j+1}+1)}{P_2^{j+1}(P_2^{j+1}+1)} \right] + K_{\beta\gamma} (C_{\beta\gamma}^{eq} - C_{\gamma\beta}^{eq})}{\Delta x_\beta \left[ \frac{(2P_2^{j+1}-3)}{(1-P_2^{j+1})(2-P_2^{j+1})} \right] - \frac{D_\gamma \left[ \frac{(2P_2^{j+1}+1)}{P_2^{j+1}(P_2^{j+1}+1)} \right] + K_{\beta\gamma} (C_{\beta\gamma}^{eq} - C_{\gamma\beta}^{eq})}$$

{5.32}

If  $P_2^{j+1} > 1$ , the  $i_2$  node needs to be updated by  $i_2^{j+1} = i_2^j + 1$  and the progression

factor is updated by  $P_2^{j+1'} = P_2^{j+1} - 1$ ; so, the concentration at the phase boundary is

$$C_{b_2^-}^{j+1} =$$

$$\frac{D_\gamma \left[ \frac{P_2^{j+1}+1}{P_2^{j+1}+2} C_{i_2-2}^{j+1} - \frac{P_2^{j+1}+2}{P_2^{j+1}+1} C_{i_2-1}^{j+1} \right] - \frac{D_\beta \left[ \frac{(2P_2^{j+1}-3)(C_{\beta\gamma}^{eq} - C_{\gamma\beta}^{eq})}{(1-P_2^{j+1})(2-P_2^{j+1})} + \frac{2(C_{\beta\gamma}^{eq} - C_{\gamma\beta}^{eq})}{(1-P_2^{j+1})(3-P_2^{j+1})} + \frac{(3-P_2^{j+1}) C_{i_2+2}^{j+1}}{2-P_2^{j+1}} + \frac{(P_2^{j+1}-2) C_{i_2+3}^{j+1}}{3-P_2^{j+1}} \right] + K_{\beta\gamma} C_{\gamma\beta}^{eq} (C_{\beta\gamma}^{eq} - C_{\gamma\beta}^{eq})}{\Delta x_\gamma \left[ \frac{P_2^{j+1}+1}{P_2^{j+1}+2} - \frac{P_2^{j+1}+2}{P_2^{j+1}+1} \right] - \frac{D_\beta \left[ \frac{(2P_2^{j+1}-3)}{(1-P_2^{j+1})(2-P_2^{j+1})} + \frac{2}{(1-P_2^{j+1})(3-P_2^{j+1})} \right] - \frac{D_\gamma \left[ \frac{(2P_2^{j+1}+1)}{P_2^{j+1}(P_2^{j+1}+1)} - \frac{2}{P_2^{j+1}(P_2^{j+1}+2)} \right] + K_{\beta\gamma} (C_{\beta\gamma}^{eq} - C_{\gamma\beta}^{eq})}{\Delta x_\beta \left[ \frac{(2P_2^{j+1}-3)}{(1-P_2^{j+1})(2-P_2^{j+1})} + \frac{2}{(1-P_2^{j+1})(3-P_2^{j+1})} \right] - \frac{D_\gamma \left[ \frac{(2P_2^{j+1}+1)}{P_2^{j+1}(P_2^{j+1}+1)} - \frac{2}{P_2^{j+1}(P_2^{j+1}+2)} \right] + K_{\beta\gamma} (C_{\beta\gamma}^{eq} - C_{\gamma\beta}^{eq})}$$

{5.33},

and the  $i_2$  and  $i_2 + 1$  nodes have to be recalculated by

$$C_{i_2}^{j+1} = \frac{-P_2^{j+1}}{2 + P_2^{j+1}} C_{i_2-2}^{j+1} + \frac{2P_2^{j+1}}{1 + P_2^{j+1}} C_{i_2-1}^{j+1} + \frac{2}{(2 + P_2^{j+1})(1 + P_2^{j+1})} C_{b_2^-}^{j+1} \quad \{5.34\}$$

and

$$C_{i_2+1}^{j+1} = \frac{2}{(P_2^{j+1} - 2)(P_2^{j+1} - 3)} C_{b_2^-}^{j+1} + \frac{2 - 2P_2^{j+1}}{2 - P_2^{j+1}} C_{i_2+2}^{j+1} + \frac{P_2^{j+1} - 1}{3 - P_2^{j+1}} C_{i_2+3}^{j+1} \quad \{5.35\}.$$

A complete concentration profile can be obtained by applying Eqs. (5.8), (5.9), (5.20), (5.21), (5.22), (5.23), (5.26) and (5.32) sequentially. If  $P_1^{j+1} > 1$ , Eqs. (5.30), (5.28) and (5.29) have to be applied to update the concentration near the phase boundary. On the other hand, if  $P_2^{j+1} > 1$ , Eqs. (5.33), (5.34) and (5.35) are utilized.

#### 5.3.4 Demonstration of the two phase boundaries progression

The movement of each phase boundary is determined by the reaction at the phase boundary, and the Li diffusion. Such correlation can be described by the normalized reaction rate coefficient  $\kappa$  of the phase boundary.

For the interface  $S_1$ , it is defined as

$$\kappa_1 = \frac{K_{\alpha\beta}}{K_{\alpha\beta,o}} \quad \text{where} \quad K_{\alpha\beta,o} = \frac{D_\beta}{(c_{\beta\alpha}^{eq} - c_{\alpha\beta}^{eq})L_o} \quad \{5.36\}$$

For the interface  $S_2$ , it is defined as

$$\kappa_2 = \frac{K_{\beta\gamma}}{K_{\beta\gamma,o}} \quad \text{where} \quad K_{\beta\gamma,o} = \frac{D_\gamma}{(c_{\gamma\beta}^{eq} - c_{\beta\gamma}^{eq})L_o} \quad \{5.37\}.$$

If  $\kappa \rightarrow \infty$ , the movement of the phase boundary is only limited by the Li diffusion near the phase boundary, so called the diffusion-controlled case. If  $\kappa \rightarrow 0$ , the movement of the phase boundary is constrained by the reaction that takes place at the boundary, which requires a high supersaturation of Li atoms in front of the phase boundary as the driving force, and it is called the interface-controlled case. For a finite value of  $\kappa$ , the

characteristic of the phase boundary movement is considered as mixed-mode. In section 4.3.4, the progression of a single moving boundary with different values of  $\kappa$  is discussed. Here, the influence of the boundary movements with different values of  $\kappa_1$  and  $\kappa_2$  on the resulting layer composition is discussed. Two kinds of demonstration corresponding to the Experiments [i] and [ii] are discussed. For the case with a layer of pre-grown  $\text{Li}_2\text{Sn}_5$  ( $\beta$ ) phase, the simulations are shown in Fig. 5.10. The values of  $\kappa_1$  and  $\kappa_2$  are labeled in the figures. The initial positions  $S_{1,0}$  is 250 nm and  $S_{2,0}$  is 50 nm. The kinetic parameters used in the demonstration are presented in Table 5.4. Note that in the demonstrations, the original thickness of Sn anode is set to be 1  $\mu\text{m}$ . Thus, to reduce the influence of the film thickness on the phase growth, the Li diffusivities are assigned at smaller values.

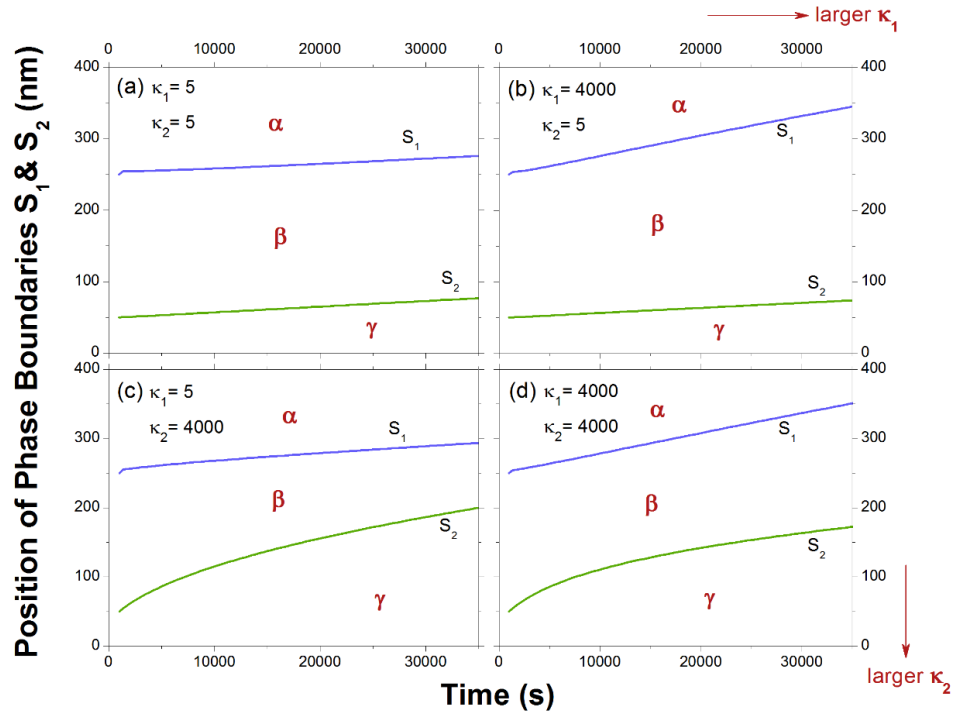


**Figure 5.10.** Comparison of the phase propagation in the film consisting of a pre-grown  $\beta$  layer with different values of normalized reaction rate coefficients  $\kappa_1$  and  $\kappa_2$ .

**Table 5.4.** Parameters used in the demonstration in Figs. 5.10 and 5.11

Assigned Li diffusivity in Sn ( $\alpha$ ) phase, $D_\alpha$	$3 \times 10^{-13} \text{ cm}^2/\text{s}$
Assigned Li diffusivity in $\text{Li}_2\text{Sn}_5$ ( $\beta$ ) phase, $D_\beta$	$2 \times 10^{-13} \text{ cm}^2/\text{s}$
Assigned Li diffusivity in $\text{LiSn}$ ( $\gamma$ ) phase, $D_\gamma$	$4 \times 10^{-13} \text{ cm}^2/\text{s}$
Li concentration at the surface in $\gamma$ phase, $C_s$	$4.338 \times 10^{-23} \text{ mol}/\text{nm}^3$
Equilibrium Li concentration at interface $S_2$ in $\gamma$ phase, $C_{\gamma\beta}^{eq}$	$4.298 \times 10^{-23} \text{ mol}/\text{nm}^3$
Equilibrium Li concentration at interface $S_2$ in $\beta$ phase, $C_{\beta\gamma}^{eq}$	$2.109 \times 10^{-23} \text{ mol}/\text{nm}^3$
Equilibrium Li concentration at interface $S_1$ in $\beta$ phase, $C_{\beta\alpha}^{eq}$	$2.059 \times 10^{-23} \text{ mol}/\text{nm}^3$
Equilibrium Li concentration at interface $S_1$ in $\alpha$ phase, $C_{\alpha\beta}^{eq}$	$5.0 \times 10^{-25} \text{ mol}/\text{nm}^3$

In Fig. 5.10a, the two boundaries are both limited by the reactions at the interfaces as both  $\kappa_1$  and  $\kappa_2$  are small. The progression of  $S_1$  and  $S_2$  are slow and shows a linearity with time, which results in a constant thickness of the  $\text{Li}_2\text{Sn}_5$  phase. In Fig. 5.10b, the higher value of  $\kappa_1$  leads to faster progression of  $S_1$ , whereas the movement of  $S_2$  remains relatively the same. Thus, the thickness of the  $\beta$  phase increases with time. Fig. 5.10c shows a case, in which the value of  $\kappa_2$  is larger than  $\kappa_1$ . Since the movement of  $S_2$  is much faster than  $S_1$ , the thickness of the  $\beta$  phase decreases as the two boundaries become closer. In Fig. 5.10d, both  $\kappa_1$  and  $\kappa_2$  are large, which means both of the boundaries are near the diffusion-controlled condition; however, since the interface  $S_2$  is closer to the surface, the distance of Li diffusion to reach  $S_2$  is smaller; thus the interface  $S_2$  can move faster, and the thickness of the  $\beta$  phase slightly decreases.

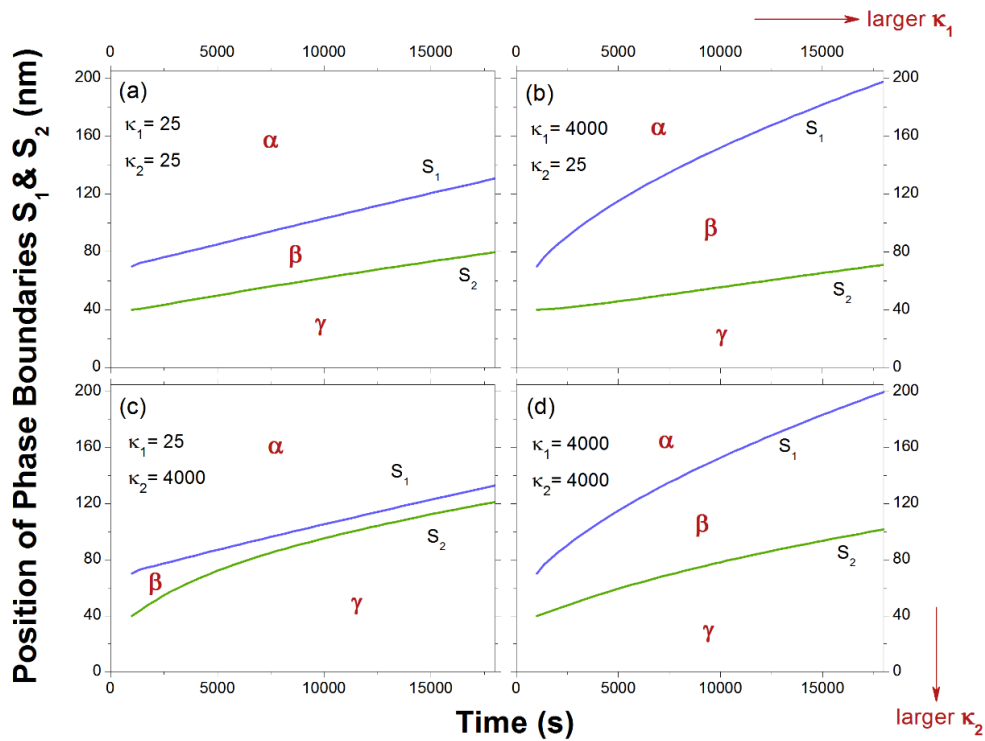


**Figure 5.11.** Comparison of the phase propagation that both  $\beta$  and  $\gamma$  phases initiate from the film surface with different values of normalized reaction rate coefficients  $\kappa_1$  and  $\kappa_2$ .

Fig. 5.11 shows the second demonstration corresponds to the case that the two phase boundaries initiate simultaneously at the anode surface. Note that in the calculation, the two interfaces have to start with some finite thickness of the  $\beta$  and  $\gamma$  phases; thus, in Fig. 5.11, the initial positions are  $S_{1,o}$  at  $x = 70$  nm and  $S_{2,o}$  at  $x = 40$  nm. The values of  $\kappa_1$  and  $\kappa_2$  for each simulation are labeled in the figures. In Fig. 5.11a, both  $\kappa_1$  and  $\kappa_2$  are small; so, the movements of  $S_1$  and  $S_2$  are similar and the thickness of the  $\beta$  phase slightly increases. In Fig. 5.11b,  $\kappa_1$  is large and leads to the parabolic and fast progression of  $S_1$ , whereas, the movement of  $S_2$  is linear and slow. Therefore, the thickness of the  $\beta$  phase increases.

In Fig. 5.11c,  $\kappa_2$  is larger than  $\kappa_1$ ; thus, the interface  $S_2$  moves faster than  $S_1$  which leads to a very thin  $\beta$  phase layer and a thick  $\gamma$  phase layer. Note that in the simulation framework, the phase boundaries cannot be created or removed during the calculation; therefore, the distance between the boundaries can only be reduced to a finite thickness as seen in Fig. 5.11c. In Fig. 5.11d, both  $\kappa_1$  and  $\kappa_2$  are large; therefore,  $S_1$  and  $S_2$  both progress parabolically, and the thickness of  $\beta$  phase increases with time.

#### 5.4. Calibration with experiments of two moving boundaries

The numerical solution is employed to understand the phase boundary propagation and analyze the stress evolution in the Sn anodes. The simulated results are compared with the current density and stress-thickness acquired in the Experiments [i] and [ii]. For brevity, the common parameters that utilized in the calculations are presented in Table 5.5. Note that the limited Li solubility in Sn ( $\alpha$ ) phase and  $\text{Li}_2\text{Sn}_5$  ( $\beta$ ) phase are assumed to be  $5.0 \times 10^{-25}$  mol/nm<sup>3</sup> ( $\sim 0.01$  Li atom per

Sn atom) higher than the corresponding stoichiometric Li concentrations and are considered as fitting parameters to have good agreement with the experiments.<sup>6</sup>

**Table 5.5.** Parameters used in the calculation for comparison with experiments

Initial thickness of anode, $L_0$	1850 nm
Number of node points, $M$	200
Grid spacing of Sn phase, $\Delta x_\alpha$	9.25 nm
Grid spacing of $\text{Li}_2\text{Sn}_5$ phase, $\Delta x_\beta$	11.285 nm
Grid spacing of LiSn phase, $\Delta x_\gamma$	13.968 nm
Volume expansion ratio of Sn- $\text{Li}_2\text{Sn}_5$ phase transformation, $r_{\alpha\beta}$	1.22
Volume expansion ratio of Sn-LiSn phase transformation, $r_{\alpha\gamma}$	1.51
Initial Li concentration in Sn phase, $C_i$	0 mol/nm <sup>3</sup>
Li solubility in Sn phase, $C_{\alpha\beta}^{eq}$	$5.0 \cdot 10^{-25}$ mol/nm <sup>3</sup>
(Equilibrium Li concentration at interface $S_1$ in $\alpha$ phase)	(i.e., $\sim 0.01$ Li per Sn atom)
Stoichiometric Li concentration of $\text{Li}_2\text{Sn}_5$ phase, $C_{\beta\alpha}^{eq}$	$2.0590 \times 10^{-23}$ mol/nm <sup>3</sup>
(Equilibrium Li concentration at interface $S_1$ in $\beta$ phase)	(i.e., 0.4 Li per Sn atom)
Li solubility in $\text{Li}_2\text{Sn}_5$ phase, $C_{\beta\gamma}^{eq}$	$2.109 \times 10^{-23}$ mol/nm <sup>3</sup>
(Equilibrium Li concentration at interface $S_2$ in $\beta$ phase)	(i.e., $\sim 0.41$ Li per Sn atom)
Stoichiometric Li concentration of LiSn phase, $C_{\gamma\beta}^{eq}$	$4.061 \times 10^{-23}$ mol/nm <sup>3</sup>
(Equilibrium Li concentration at interface $S_2$ in $\gamma$ phase)	(i.e., 1.0 Li per Sn atom)
Surface Li concentration in LiSn phase at 0.5 V, $C_S^{0.5V}$	$4.098 \times 10^{-23}$ mol/nm <sup>3</sup>
Surface Li concentration in $\text{Li}_2\text{Sn}_5$ phase at 0.65 V, $C_S^{0.65V}$	$2.083 \times 10^{-23}$ mol/nm <sup>3</sup>
Biaxial modulus of fused-silica substrate, $M_S$	86.4 GPa
Biaxial modulus of Sn, $M_{Sn}$	76.9 GPa
Thickness of fused-silica substrate, $h_S$	500 $\mu\text{m}$
Stress-thickness of SEI, $\sigma_{SEI} h_{SEI}$	8.8 MPa- $\mu\text{m}$

#### 5.4.1 Experiment [i]: the growth of $\text{Li}_2\text{Sn}_5$ and $\text{LiSn}$ phases with a pre-grown $\text{Li}_2\text{Sn}_5$ layer

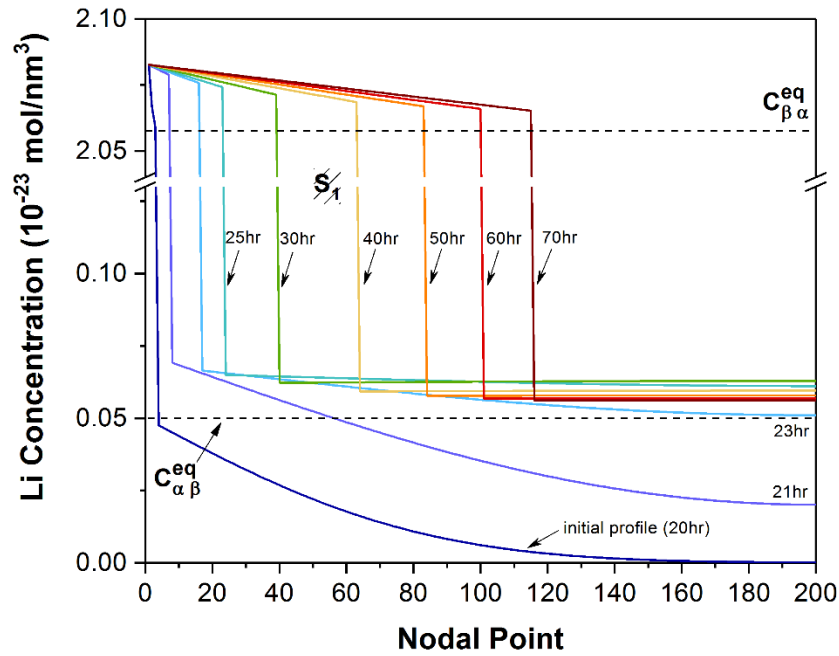
In the experiment, the potential was initially held at 0.65 V vs.  $\text{Li}/\text{Li}^+$  for 50 hours after the SEI formation at 0.8 V for 20 hours, and then changed to 0.5 V for 100 hours. During the potential hold at 0.65 V, the current density (Fig. 5.4a) only relates to the movement of interface  $S_1$ . A transient behavior in stress is observed in the curvature measurement at the beginning of the  $\text{Sn-Li}_2\text{Sn}_5$  phase transformation (Fig. 5.4b). The finite-difference analysis of a single moving boundary (described in chapter 4) is used to calculate the progression of interface  $S_1$  and the stress evolution during the potential hold at 0.65 V. The initial condition is illustrated in Fig. 5.7a and the initial concentration profile is shown in Fig. 5.12. The nucleation time of  $\text{Sn-Li}_2\text{Sn}_5$  phase transformation is about 700 s which is estimated by the nucleation characteristic in the current density at the beginning of 0.65 V holding as shown in the left inset in Fig. 5.4a. The details of the nucleation characteristic is discussed in sections 3.2.1 and 4.1.3. The calculated Li flux can be used to obtain the simulated current density and compared with the measured values. The parameters used in the calculation are provided in Table 5.6. The fitting procedure is performed by the non-linear square fitting and the result is shown as a dash line in Fig. 5.4.a. The acquired kinetic parameters ( $D_\alpha$ ,  $D_\beta$  and  $K_{\alpha\beta}$ ) are presented in Table 5.7. and the corresponding evolution of the concentration profile is shown in Fig. 5.12.

**Table 5.6.** Parameters used in calculation in Figs. 5.12 and 5.13: the lithiation at 0.65 V in Experiment [i]

Size of time step in simulation, $\Delta t$	0.0545 s
Nucleation time of $\text{Sn-Li}_2\text{Sn}_5$ phase transformation, $t_0^{S_1}$	700 s
Initial position of $\text{Li}_2\text{Sn}_5/\text{Sn}$ phase boundary, $S_{1,0}$	36 nm

**Table 5.7.** Material parameters obtained by numerical analysis of Experiment [i]

Li diffusivity in Sn phase, $D_\alpha$	$1.8 \times 10^{-12} \text{ cm}^2/\text{s}$
Li diffusivity in $\text{Li}_2\text{Sn}_5$ phase, $D_\beta$	$5.5 \times 10^{-12} \text{ cm}^2/\text{s}$
Li diffusivity in $\text{Li}_2\text{Sn}_5$ phase, $D_\gamma$	$3.5 \times 10^{-12} \text{ cm}^2/\text{s}$
Reaction rate coefficient of Sn- $\text{Li}_2\text{Sn}_5$ phase transformation, $K_{\alpha\beta}$	$6.0 \times 10^{-6} \text{ cm}^4/\text{mol s}$
Reaction rate coefficient of $\text{Li}_2\text{Sn}_5$ -LiSn phase transformation, $K_{\beta\gamma}$	$4.0 \times 10^{-5} \text{ cm}^4/\text{mol s}$
Nominal yield stress of Sn, $\sigma_0$	-9 MPa
Low strain-rate yield stress of $\text{Li}_2\text{Sn}_5$ , $\sigma_{\text{Li}_2\text{Sn}_5}$	-25 MPa
Low strain-rate yield stress of LiSn, $\sigma_{\text{LiSn}}$	-61 MPa
Strain rate exponent, $m$	1.45
Strain rate coefficient, $\dot{\epsilon}_0$	$1.6 \times 10^{-7}$
Volume expansion of Sn phase due to Li insertion, $\eta$	$6.5 \times 10^{20} \text{ nm}^3/\text{mol}$

**Figure 5.12.** The calculated evolution of the Li concentration profile during the potentiostatic lithiation at 0.65 V in the Experiment [i].

As shown in Fig. 5.12, while the phase boundary (interface  $S_1$ ) moves, the Li concentration in the  $\text{Li}_2\text{Sn}_5$  phase remains linear and is above the stoichiometric value  $C_{\beta\alpha}^{eq}$ . For the Li concentration in the Sn phase, it accumulates beyond the solubility limit  $C_{\alpha\beta}^{eq}$  and then relaxes by diffusion toward the interface  $S_1$ . Therefore, in the stress calculation, we consider the stress in  $\text{Li}_2\text{Sn}_5$  phase  $\sigma_{\text{Li}_2\text{Sn}_5}$  to be at a low strain-rate yield stress, and assume it is a constant. Whereas, the stress in Sn phase varies due to the Li diffusion. Here, the mechanisms of rate-dependent plasticity and elastic unloading are considered (as discussed in section 4.4). When the Li concentration is increasing (i.e., the rate of Li concentration change  $\dot{C} > 0$ ), the rate-dependent stress is assumed can be described by viscoplasticity<sup>10</sup> as

$$\sigma_{Sn} = \sigma_o \left( \frac{2\eta}{3\dot{\epsilon}_o} \dot{C} + 1 \right)^{\frac{1}{m}} \quad \{5.38\}$$

where  $\sigma_o$  is the nominal yield stress of Sn;  $\eta$  is the volume expansion of Sn due to Li insertion;  $\dot{\epsilon}_o$  is the strain rate constant and  $m$  is the strain rate exponent. If  $\dot{C}$  is large and positive, the large strain rate leads to a high stress in Sn. On the other hand, when the Li diffuses toward the phase boundary, the Li flux is reversed and  $\dot{C} < 0$ , and the stress is decreased and can be described by elastic unloading as

$$\sigma_{Sn} = \sigma_{Sn}^{ul} - \eta M_{Sn} \Delta C^{ul} \quad \{5.39\}$$

where  $\sigma_{Sn}^{ul}$  is the local stress in Sn right before elastic unloading; it is a function of

position  $x$  and its magnitude is given by Eq. (5.38).  $\Delta C^{ul}$  is the local decrease of concentration during the elastic unloading. Note that the two mechanisms can happen at different positions in the anode simultaneously, depending on  $\dot{C}$  at each position. The stress in the Sn layer is then calculated depending on the sign of  $\dot{C}$ , and the stress in the  $\text{Li}_2\text{Sn}_5$  layer is set to be constant. The evolution of stress distribution in the Sn anode is shown in Fig. 5.13. The simulated stress-thickness obtained by the stress integration of the entire anode is compared with the measured values, and is shown as a dash line in Fig. 5.4b. The acquired mechanical parameters ( $\sigma_0$ ,  $\sigma_{\text{Li}_2\text{Sn}_5}$ ,  $m$ ,  $\epsilon_0$ , and  $\eta$ ) are presented in Table. 5.7. and are in good agreement with the results in chapter 4. The two stress mechanisms can happen in the Sn layer at the same time depending on the sign of  $\dot{C}$  at each position. The position where the two the stress mechanism are distinguished in the Sn layer is referred to as the flux-reversal boundary as demonstrated in section 4.4.3.

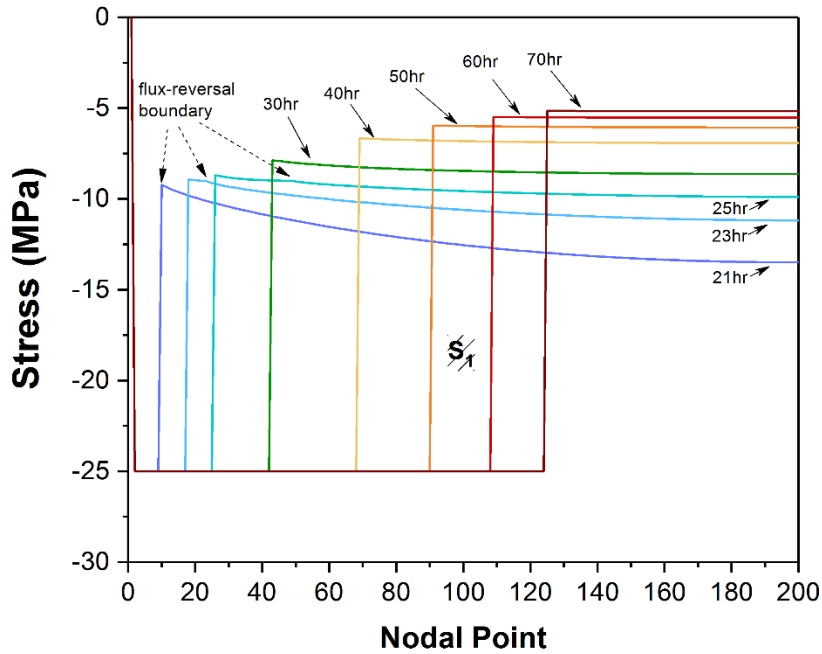


**Figure 5.13.** The calculated evolution of stress distribution in the anode during the potentiostatic lithiation at 0.65 V in the Experiment [i].

In Fig. 5.13, the flux-reversal boundary distinguished by the sign of  $\dot{C}$  in the Sn layer is seen at time 21, 23 and 25 hours. For the region beyond the flux-reversal boundary, the Li increases and stress is described by viscoplasticity (Eq. 5.38). For the region close to the phase boundary  $S_1$ , the stress is reduced by elastic unloading (Eq. 5.39). It is noticed that the flux-reversal boundary moves away from the interface as the interface progresses. This evolution of the flux-reversal boundary means the dominant stress mechanism in the Sn layer alters from viscoplasticity to elastic unloading as the phase transformation takes place. Thus, for the time greater than 30 hours, the entire Sn layer is under the state of elastic unloading.

At the end of the lithiation at 0.65 V ( $t = 70$  hours), the interface  $S_1$  reaches approximately the 125<sup>th</sup> node ( $x \sim 1300$  nm). The stress in Sn becomes fairly constant with an approximate value of -5 MPa as the result of elastic unloading mechanism. These findings are used in the following stress analysis for the lithiation at 0.5 V.

As shown in the measured current density in Fig. 5.4a, when the potential is changed to 0.5 V, a higher Li concentration is established and leads to a large current density. The higher surface Li concentration also activates the  $\text{Li}_2\text{Sn}_5/\text{LiSn}$  phase transformation. The nucleation time ( $t_0^{S_2} = 940$  s) is estimated from the nucleation characteristic of current density shown in the right inset in Fig. 5.4a. At the end of LiSn phase nucleation, a thin layer of  $\text{Li}_2\text{Sn}_5$  phase at the surface is transformed into a continuous layer of LiSn phase (thickness of  $S_{2,0}$ ) as illustrated in Fig. 5.7c. The thickness of  $S_{2,0}$  is estimated from the accumulated charge during the nucleation time at 0.5 V. The Li concentration profile at 70 hours in Fig. 5.12 is imported as part of the initial condition as discussed in 5.3.1. The resulting initial condition is shown as concentration profile at 70.3 hours in Fig. 5.14.

The numerical solution of two moving boundaries is used to solve the phase

propagation and to analyze the measured current density. The simulated current density is shown as a dash line in Fig. 5.4.a, and the corresponding evolution of Li concentration is shown in Fig. 5.14. The parameters used in the calculation are presented in Table 5.8, and the fitting results of the kinetic parameters ( $D_\gamma$  and  $K_{\beta\gamma}$ ) are shown in Table 5.7.

**Table 5.8.** Parameter values used in calculation in Fig. 5.14: the lithiation at 0.5 V in the Experiment [1]

Size of time step in simulation, $\Delta t$	0.048 s
Nucleation time of $\text{Li}_2\text{Sn}_5$ -LiSn phase transformation, $t_0^{S_2}$	940 s
Initial position of LiSn/ $\text{Li}_2\text{Sn}_5$ phase boundary, $S_{2,0}$	70 nm
Initial position of $\text{Li}_2\text{Sn}_5$ /Sn phase boundary, $S_1(t_2)$	1250 nm

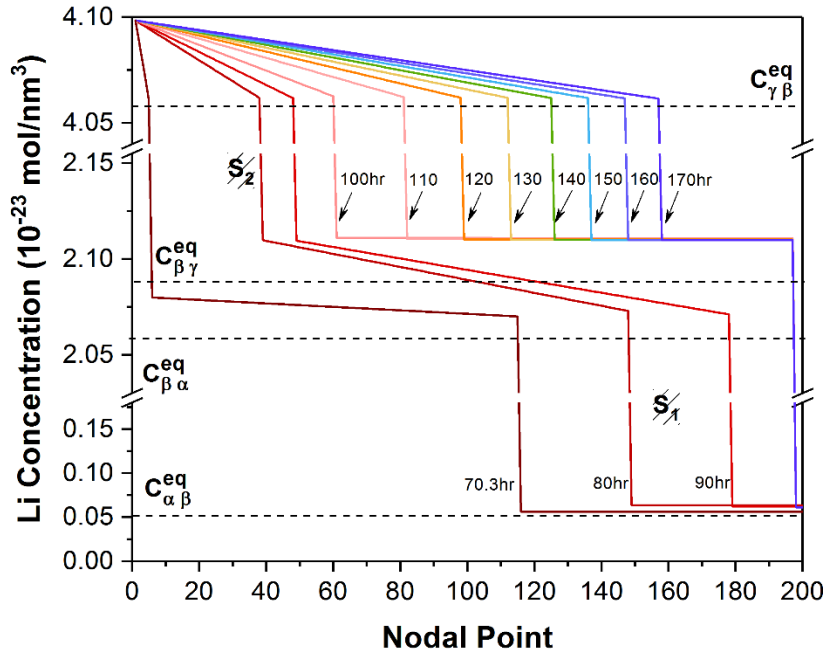


**Figure 5.14.** The calculated evolution of the Li concentration profile during the potentiostatic lithiation at 0.5 V in the Experiment [1].

As shown in Fig. 5.14, interfaces  $S_1$  and  $S_2$  move together during the potential hold at 0.5 V. At a time of around 100 hours, the interface  $S_1$  reaches the end of the anode, which means for time greater than 100 hours, only the interface  $S_2$  moves in the anode. Note that the phase boundary cannot be removed from the simulation framework during calculation; thus, the interface  $S_1$  remains stationary located near the end of anode (i.e., node M-3). It is also seen that the Li concentration in all the phases (Sn,  $\text{Li}_2\text{Sn}_5$ , and LiSn) remains almost linear while the phase boundaries move. The Li concentration in the LiSn phase is above the stoichiometric value  $C_{\gamma\beta}^{eq}$ . The Li concentration in  $\text{Li}_2\text{Sn}_5$  phase is between the stoichiometric value  $C_{\beta\alpha}^{eq}$  and the Li solubility of  $\text{Li}_2\text{Sn}_5$   $C_{\beta\gamma}^{eq}$ . In addition, as the interface  $S_1$  reaches the end of the anode, the Li concentration in  $\text{Li}_2\text{Sn}_5$  phase is saturated and slightly beyond the solubility value  $C_{\beta\gamma}^{eq}$ . The Li concentration in the Sn phase remains fairly constant and slightly above the Li solubility of Sn  $C_{\alpha\beta}^{eq}$ . Therefore, in the stress calculation, the stress of Sn and  $\text{Li}_2\text{Sn}_5$  are assumed to be at the same value as those at the end of potentiostatic lithiation at 0.65 V in Fig. 5.13. The stress in the LiSn phase is assumed to be at a constant low strain rate stress, and its value ( $\sigma_{\text{LiSn}} = -61$  MPa) is obtained by comparing the measured stress-thickness in Fig. 5.4b with the calculated stress-thickness (Eq. 5.1).

The comprehensive phase boundary propagation of the Experiment [i] is presented in Fig. 5.15, in which the anode surface (i.e., the electrolyte/anode interface) is located at  $x = 0$ . From 20 to 70 hours (potential held at 0.65 V), the interface  $S_1$  moves from 35 nm to 1300 nm, and the anode expands (i.e.,  $L(t)$  increases) due to the Sn- $\text{Li}_2\text{Sn}_5$  phase transformation. A mixed process of diffusion-controlled and interfaced-controlled describes the movement of interface  $S_1$ . From 70 to 170 hours (potential held at 0.5 V),

the interface  $S_2$  initiates from  $x = 70$  nm near the surface. Between 70 to 98 hours, it is seen that as the interface  $S_2$  moving, many of Li atoms pass through the interface  $S_2$  and diffuse toward the interface  $S_1$ . Therefore, the interface  $S_1$  continuously progresses and reaches the end of anode around 98 hours. Note that the progression of the interface  $S_1$  beyond 98 hours is due to the volume expansion of  $\text{Li}_2\text{Sn}_5$ - $\text{LiSn}$  phase transformation as shown in Eq. (5.11). For time greater than 98 hours, the Li concentration in the  $\text{Li}_2\text{Sn}_5$  phase accumulates and reaches the solubility  $C_{\beta\gamma}^{eq}$  as seen in Fig. 5.14. In the subsequent lithiation, the reaction at phase interface  $S_2$  becomes dominant. A mixture behavior of diffusion-controlled and interfacial-controlled is also found from the movement of interface  $S_2$ .

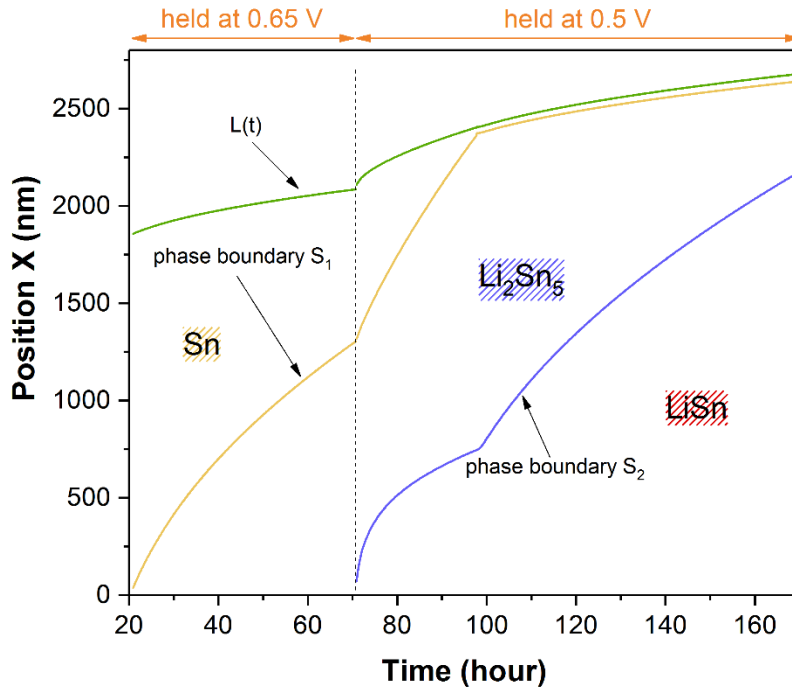


**Figure 5.15.** The propagation of phase boundaries during the potential hold at 0.65 V and 0.5 V in the Experiment [1] obtained by the numerical analysis. The electrolyte/anode interface is located at  $x = 0$ .

An alternative way to present the phase boundary movement is shown in Fig. 5.16, in which the end of the film (i.e., the anode/substrate interface) is located at  $x = 0$ , and it is essentially the evolution of cross-section of the anode.

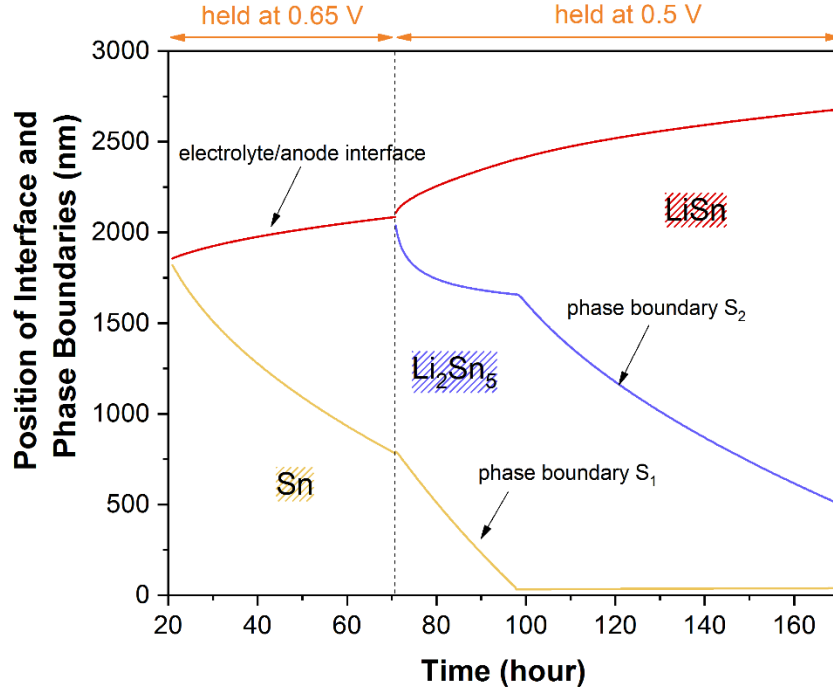


**Figure 5.16.** The propagation of phase boundaries at 0.65 V and 0.5 V in Experiment [1] obtained by the numerical analysis. The anode/substrate interface is located at  $x = 0$ .

In addition, the phase boundary propagation can also be obtained directly from the accumulated coulombic charge and the measured stress-thickness. The balance equations for this analysis are:

$$q_{\alpha\beta}h_{Li_2Sn_5} + q_{\alpha\gamma}h_{LiSn} = Q_{total} \quad \{5.40\}$$

and

$$\langle\sigma_{SEI}\rangle h_{SEI} + \langle\sigma_{Sn}\rangle \left( h_{Sn}^o - \frac{h_{Li_2Sn_5}}{r_{\alpha\beta}} - \frac{h_{LiSn}}{r_{\alpha\gamma}} \right) + \langle\sigma_{Li_2Sn_5}\rangle h_{Li_2Sn_5} + \langle\sigma_{LiSn}\rangle h_{LiSn} = \langle\sigma\rangle h_f \quad \{5.41\}$$

where  $q_{\alpha\beta}$  and  $q_{\alpha\gamma}$  are, respectively, the Li consumption for transforming Sn into  $\text{Li}_2\text{Sn}_5$  and  $\text{LiSn}$ . The term  $(h_{\text{Sn}}^o - \frac{h_{\text{Li}_2\text{Sn}_5}}{r_{\alpha\beta}} - \frac{h_{\text{LiSn}}}{r_{\alpha\gamma}})$  in Eq. (5.41) is the thickness of Sn phase, as  $h_{\text{Sn}}^o$  is the original thickness of the Sn layer. This analysis assumes that all the charge accumulated below 0.8 V is consumed by the phase transformations and the stress in the layers is uniform. The thicknesses  $h_{\text{Li}_2\text{Sn}_5}$  and  $h_{\text{LiSn}}$  can be solved from Eqs. (5.40) and (5.41). For the lithiation at 0.65 V, the thickness  $h_{\text{Li}_2\text{Sn}_5}$  can be estimated from the accumulated charge. The parameter values used in this analysis is presented in Table 5.9 and the results are shown in Fig. 5.17. A good agreement is found between the results of phase propagation presented in Figs. 5.16 and 5.17. Furthermore, the position of the phase boundaries at 170 hours is consistent with the results of cross-section (Fig. 5.1a) and XRD (Fig. 5.2a).

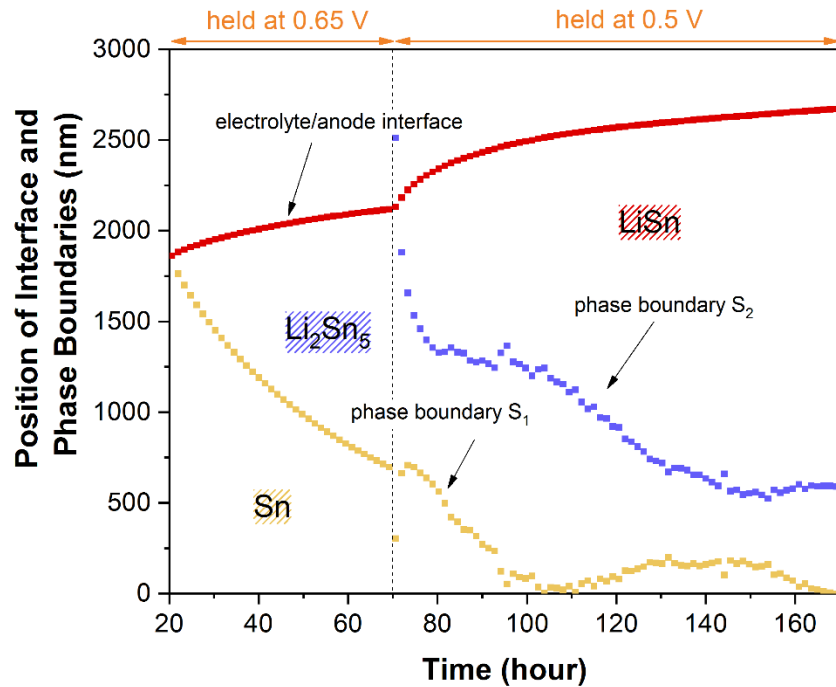


**Figure 5.17.** The propagation of phase boundaries during lithiation at 0.65 V and 0.5 V in Experiment [1] obtained from the balance of the measured stress-thickness and coulombic charge. The anode/substrate interface is located at  $x = 0$ .

**Table 5.9.** Parameters used in calculation with Eqs. (5.40) and (5.41) for the Experiment [i]

Li consumption of Sn-Li <sub>2</sub> Sn <sub>5</sub> phase transformation, $q_{\alpha\beta}$	$3.934 \times 10^{-3}$ C / nm of Li <sub>2</sub> Sn <sub>5</sub>
Li consumption of Sn-LiSn phase transformation, $q_{\alpha\gamma}$	$7.946 \times 10^{-3}$ C / nm of LiSn
Original thickness of Sn phase, $h_{Sn}^0$	1850 nm
Stress-thickness of SEI, $\langle \sigma_{SEI} \rangle h_{SEI}$	8.8 MPa- $\mu$ m
Stress in Sn phase, $\langle \sigma_{Sn} \rangle$	-5 MPa
Stress in Li <sub>2</sub> Sn <sub>5</sub> phase, $\langle \sigma_{Li_2Sn_5} \rangle$	-25 MPa
Stress in LiSn phase, $\langle \sigma_{LiSn} \rangle$	-62.5 MPa

#### 5.4.2. Experiment [ii]: the simultaneous growth of Li<sub>2</sub>Sn<sub>5</sub> and LiSn phases

In the Experiment [ii], the potential was directly changed to 0.5 V after the 20-hour SEI growth at 0.8 V. The measured current density and stress-thickness are shown in Fig. 5.4. The solid lines are the experimental data, and the dash lines are the results obtained by finite-difference analysis described as follow.

In Fig. 5.4b, a transient stress is observed at the beginning of the potential hold at 0.5 V, which relates to the progression of two moving boundaries. In order to understand the transient stress here, the phase boundary propagation is analyzed by the finite-difference method described in section 5.3.3. The initial condition of Li concentration is illustrated in Fig. 5.6. As seen in the nucleation characteristic of current density (inset in Fig. 5.4a), the nucleation period is very short (approximately 100 s). However, the estimated thickness of nucleation layers from the accumulated charge is too thin to use in the calculation due to the limit of grid spacing in the computational framework. Therefore, the starting point of the numerical solution is set at 1500 s after the potential changed to 0.5 V with  $S_{2,0} = 40$  nm and  $S_{1,0} = 80$  nm that agrees with the accumulated

charge during this period. The parameters applied in the calculation are presented in Table 5.10. The kinetic parameters ( $D_\alpha$ ,  $D_\beta$ ,  $D_\gamma$ ,  $K_{\alpha\beta}$  and  $K_{\beta\gamma}$ ) are obtained by fitting the calculated current density (dash line) with the measured current density in Fig. 5.5a. The results are presented in Table 5.11. The values of parameters obtained here are comparable with the findings in previous analyses (chapter 4 and section 5.4.1). The evolution of Li concentration profile and the corresponding movement of the phase boundaries are shown in Figs. 5.18 and 5.19 respectively.

**Table 5.10.** Parameters used in calculation of Experiment [ii] in Figs. 5.18 and 5.19

Size of time step in simulation, $\Delta t$	0.036 s
Nucleation time, $t_o$	1500 s
Initial position of LiSn/Li <sub>2</sub> Sn <sub>5</sub> phase boundary, $S_{2,o}$	40 nm
Initial position of Li <sub>2</sub> Sn <sub>5</sub> /Sn phase boundary, $S_{1,o}$	80 nm

**Table 5.11.** Material parameters obtained by numerical analysis of Experiment [ii]

Li diffusivity in Sn phase, $D_\alpha$	$1.8 \times 10^{-12}$ cm <sup>2</sup> /s
Li diffusivity in Li <sub>2</sub> Sn <sub>5</sub> phase, $D_\beta$	$2.0 \times 10^{-12}$ cm <sup>2</sup> /s
Li diffusivity in Li <sub>2</sub> Sn <sub>5</sub> phase, $D_\gamma$	$5.5 \times 10^{-12}$ cm <sup>2</sup> /s
Reaction rate coefficient of Sn-Li <sub>2</sub> Sn <sub>5</sub> phase transformation, $K_{\alpha\beta}$	$1.0 \times 10^{-6}$ cm <sup>4</sup> /mol s
Reaction rate coefficient of Li <sub>2</sub> Sn <sub>5</sub> -LiSn phase transformation, $K_{\beta\gamma}$	$3.0 \times 10^{-6}$ cm <sup>4</sup> /mol s
Nominal yield stress of Sn, $\sigma_o$	-17 MPa
Low strain-rate yield stress of Li <sub>2</sub> Sn <sub>5</sub> , $\sigma_{Li_2Sn_5}$	-25 MPa
Low strain-rate yield stress of LiSn, $\sigma_{LiSn}$	-52 MPa
Strain rate exponent, $m$	1.2
Strain rate coefficient, $\dot{\epsilon}_o$	$1.2 \times 10^{-7}$
Volume expansion of Sn phase due to Li insertion, $\eta$	$4.6 \times 10^{20}$ nm <sup>3</sup> /mol

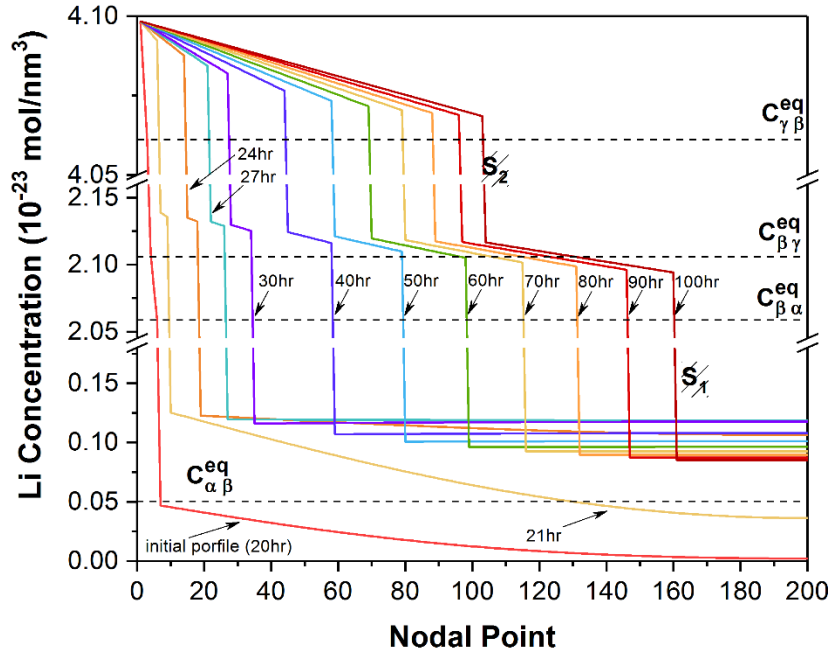


**Figure 5.18.** The calculated evolution of the Li concentration profile during the potentiostatic lithiation at 0.5 V in Experiment [ii].

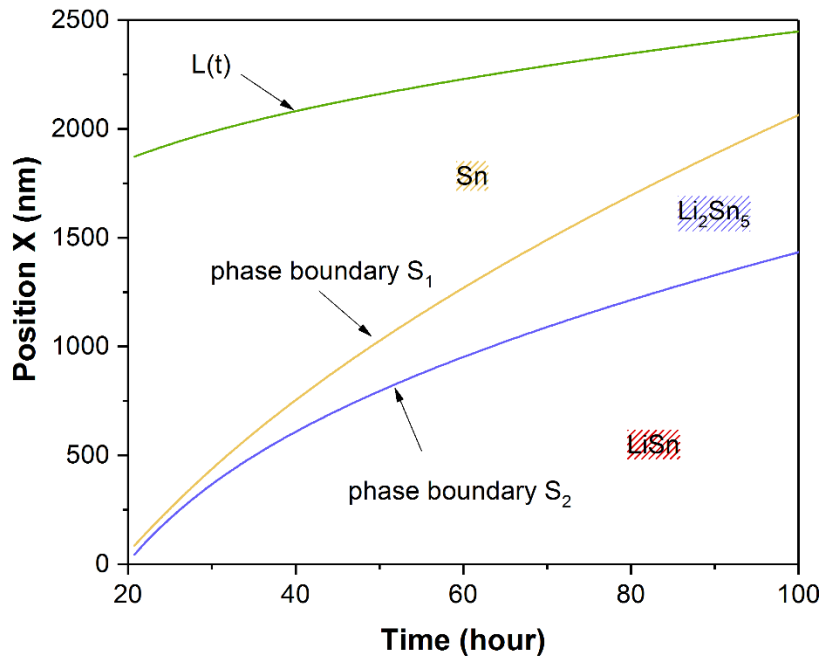


**Figure 5.19.** The propagation of phase boundaries during lithiation at 0.5 V in the Experiment [ii] obtained by numerical analysis. The electrolyte/anode interface is located at  $x = 0$ .

As shown in Fig. 5.19 both the interfaces  $S_1$  and  $S_2$  exhibit the mixed characteristic of diffusion-controlled and interface-controlled, and they progress together in the Sn anode leading to a thin  $\text{Li}_2\text{Sn}_5$  phase layer. In Fig. 5.18 the Li concentration in both the LiSn and  $\text{Li}_2\text{Sn}_5$  phases remains linear. Thus, the stresses in the  $\text{Li}_2\text{Sn}_5$  and LiSn phases are assumed to be at their low strain-rate yield stress values. Whereas, the Li concentration in the Sn phase evolves as the phase boundaries move. It accumulates beyond the Li solubility of Sn  $C_{\alpha\beta}^{eq}$  and then decreases by diffusion toward the Sn/ $\text{Li}_2\text{Sn}_5$  phase boundary, which is similar to the previous cases of diffusion-induced stress. Therefore, the mechanisms of viscoplasticity (Eq. 5.38) and elastic unloading (Eq. 5.39) are applied here to calculate the stress in the Sn layer. The mechanical parameters ( $\sigma_0$ ,  $\sigma_{\text{Li}_2\text{Sn}_5}$ ,  $\sigma_{\text{LiSn}}$ ,  $m$ ,  $\dot{\epsilon}_0$ , and  $\eta$ ) are acquired by fitting with the measured stress-thickness (Fig. 5.4b). The results are presented in Table 5.11 and the calculated stress-thickness is shown as a dash line in Fig. 5.4. The corresponding stress distribution in the anode is shown in Fig. 5.20. It is seen that the rate-dependent plasticity in Sn leads to a higher stress at the beginning of phase transformations and the high stress is relaxed as the Li diffusion slows down. The flux-reversal boundary distinguishing the stress mechanisms is seen from 21 to 27 hours. During the phase transformation, the flux-reversal boundary moves away from the Sn/ $\text{Li}_2\text{Sn}_5$  phase boundary and alters the dominant stress mechanism in the Sn layer from viscoplasticity to elastic unloading. Therefore, for time at 21 hours, almost the entire Sn layer is under the high rate-dependent stress; whereas, for time greater than 30 hours, the entire Sn layer is under the mechanism of elastic unloading and in a lower stress state. Subsequently, the higher stress in  $\text{Li}_2\text{Sn}_5$  and LiSn phases becomes dominant as the phase boundaries progress in the anode, and increases the magnitude of the stress-thickness linearly.

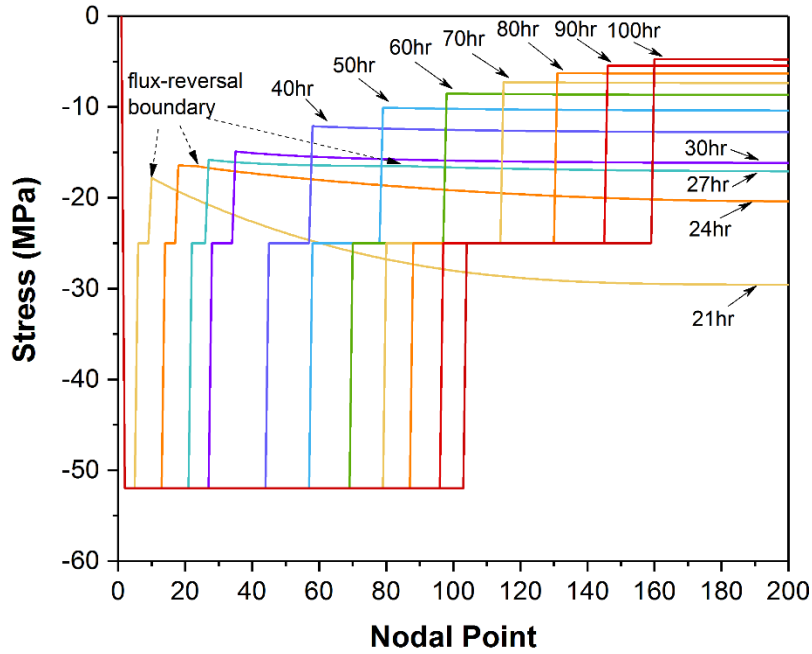


**Figure 5.20.** The calculated evolution of stress distribution in the anode during the potentiostatic lithiation at 0.5 V in Experiment [ii].

In addition, the phase boundary progression can be replotted in the perspective of cross-section as shown in Fig. 5.21, in which the anode/substrate interface is at  $x = 0$ . The phase boundary propagation can also be obtained from solving the equation set of coulombic charge and measured stress-thickness (Eqs. 5.40 and 5.41). However, as seen in Fig. 5.20, the stress in Sn varies as phase boundaries progress. Thus, the stress in Sn seen in Eq. (5.41) is considered to be a function of time. Here, the thickness-averaged stress of Sn layer calculated from the stress distribution in Fig. 5.20 is utilized in Eq. (5.40). The evolution of the cross-section acquired from the equation set is shown in Fig. 5.22, and the values of stress applied are presented in Table 5.12. A good agreement is found between the results shown in Figs. 5.21 and 5.22. The findings in the Experiment [ii] are consistent with results from the Experiment [i].

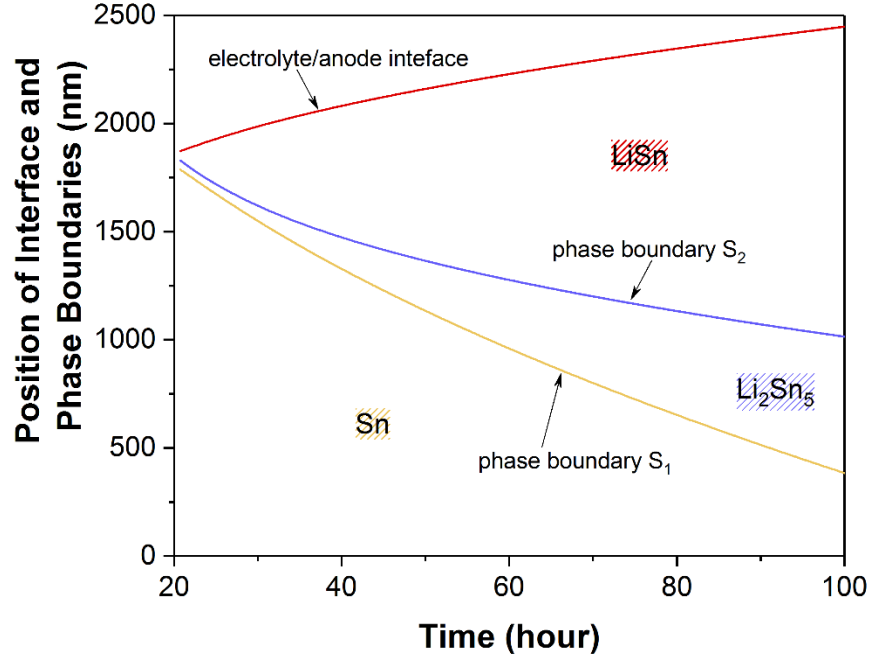


**Figure 5.21.** The propagation of phase boundaries during the potential hold at 0.5 V in Experiment [ii] obtained by the numerical analysis. The anode/substrate interface is at  $x = 0$ .

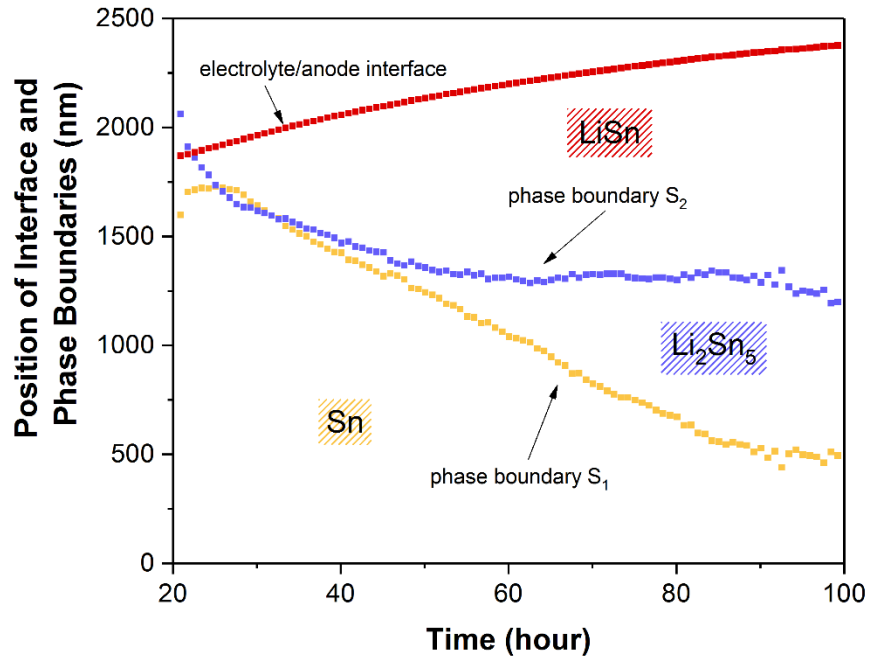


**Figure 5.22.** Evolution of interfaces in cross-section view of the Experiment [ii] obtained from measured stress-thickness and accumulated coulombic charge below 0.8 V.

**Table 5.12.** Parameters used in the calculation with Eqs. (5.40) and (5.41) for Experiment [ii]

Li consumption of Sn-Li <sub>2</sub> Sn <sub>5</sub> phase transformation, $q_{\alpha\beta}$	$3.934 \times 10^{-3}$ C / nm of Li <sub>2</sub> Sn <sub>5</sub>
Li consumption of Sn-LiSn phase transformation, $q_{\alpha\gamma}$	$7.946 \times 10^{-3}$ C / nm of LiSn
Original thickness of Sn phase, $h_{Sn}^0$	1850 nm
Stress-thickness of SEI, $\langle \sigma_{SEI} \rangle h_{SEI}$	8.8 MPa- $\mu$ m
Stress in Li <sub>2</sub> Sn <sub>5</sub> phase, $\langle \sigma_{Li_2Sn_5} \rangle$	-25 MPa
Stress in LiSn phase, $\langle \sigma_{LiSn} \rangle$	-58 MPa

### 5.5. Conclusions

In this chapter, we extended the finite-difference calculation discussed in chapter 4 to the case of two moving boundaries. The numerical solution were utilized to analyze the growth of Li<sub>2</sub>Sn<sub>5</sub> and LiSn phases in experiments. The *in situ* curvature measurement was employed to acquire the stress and thickness evolution of the anode. The kinetic and mechanical properties were obtained by comparing the simulation results and the experimental observations. The main conclusions of this study are:

- The results of the phase kinetic analysis including Li diffusivity in Sn, Li<sub>2</sub>Sn<sub>5</sub> and LiSn phases are on the order of  $10^{-12}$  cm<sup>2</sup>/s. The reaction rate coefficient of Sn-Li<sub>2</sub>Sn<sub>5</sub> phase transformation  $K_{\alpha\beta}$  is approximately on the order of  $10^{-6}$  cm<sup>4</sup>/mol s, and for Li<sub>2</sub>Sn<sub>5</sub>-LiSn phase transformation  $K_{\beta\gamma}$ , it is approximately on the order of  $10^{-5}$  to  $10^{-6}$  cm<sup>4</sup>/mol s. These findings indicate both of the phase transformations are a mixture of diffusion-controlled and interface-controlled.
- The phase propagation can also be obtained by solving the balance equations of measured stress-thickness and coulombic charge. The results are consistent with that obtained by the numerical solution.

- The stress in the  $\text{Li}_2\text{Sn}_5$  and  $\text{LiSn}$  phases were found to be at the low strain rate yield stress, and are approximately -25 MPa and -58 MPa respectively.
- The high value of stress-thickness of the transient behavior at the beginning of phase transformations in both studied cases is induced by rate-dependent plasticity associated with the excess Li diffusion in the Sn layer.
- As the phase boundary propagates, the flux of Li diffusion decreases and the relaxation of the excess Li concentration leads to a lower state of stress in Sn by elastic unloading. Subsequently, the magnitude of the stress-thickness begins to increase at a steady rate as the new phases continues to grow.

Here, the finite-difference calculation of two moving boundaries is developed, and it can be further extended to include more boundaries. This analysis can be performed to study other material systems that involve multiple phase transformations simultaneously.

## References

1. M. Winter and J. O. Besenhard, *Electrochimica Acta*, **45** 31-50 (1999).
2. J. Wang, D. X. Liu, M. Canova, R. G. Downing, L. R. Cao, and A. C. Co, *Journal of Radioanalytical and Nuclear Chemistry*, **301** 277-284 (2014).
3. E. Chason, *Thin Solid Films*, **526** 1-14 (2012).
4. L. B. Freund and S. Suresh, *Thin Film Materials: Stress, Defect Formation and Surface Evolution*, Cambridge University Press (2009).
5. M. Hillert, in *Lectures on the Theory of Phase Transformations*, H. I. Aaronson, ed., The Minerals, Metals & Materials Society, (1999).
6. W. G. Moffatt, *The Handbook of Binary Phase Diagrams*, Schenectady, N.Y. (1978).
7. J. Svoboda, F. D. Fischer, P. Fratzl, E. Gamsjager, and N. K. Simha, *Acta Materialia*, **49** 1249-1259 (2001).
8. J. Crank, *Free and Moving Boundary Problems*, Oxford (1984).
9. J. Crank and R. S. Gupta, *IMA Journal of Applied Mathematics*, **10** (1), 19-33 (1972).
10. A. F. Bower, *Applied Mechanics of Solids*, CRC Press (2009).

# Chapter 6.

## Elastic Modulus Measurement of Li-Sn Phases

---

During electrochemical cycling, Li reacts with Sn and the electrodes undergo phase transformations at different states of charge (SOC) and induce large volume expansion of Sn electrodes. It is well-known that such volume changes cause large stresses during electrochemical cycling, which leads to mechanical failure and loss of capacity.<sup>1, 2</sup>

At the same time, mechanical properties of the electrodes evolve as a function of Li concentration and volume change during cycling, which influences mechanical degradation. There have been recent reports of density functional theory (DFT) calculations,<sup>3-6</sup> which predicted significant decrease of elastic moduli of Sn electrodes as Li concentration increases. In this chapter, we report *in situ* stress measurement of evolution of stress and biaxial modulus in Sn films during electrochemical cycling. The measurement is compared with the reported computational results.

### 6.1 Experimental condition

#### 6.1.1 Sample description

The Sn thin film samples used in this study consist of a 25 nm Ti layer, a 35 nm Cu layer (both via e-beam depositions) and a 500 nm Sn layer (by electrodeposition). Fused silica wafers ( $\sim 500 \mu\text{m}$  thick, 50.8 mm in diameter, double-side polished) were used as

elastic substrates for the Sn thin films. Fig. 6.1 shows a top view of scanning electron microscope (SEM) image of an as-prepared Sn sample. It is seen that the grain size of Sn was in the range of 500 nm to 1.5  $\mu\text{m}$ . The samples were stored in an Ar-filled glove box (moisture and oxygen controlled below 0.1 ppm) after fabrication. During the storage at room temperature, an intermetallic compound (IMC)  $\text{Cu}_6\text{Sn}_5$  forms at the Cu/Sn interface.<sup>7</sup> The formation of IMC improves the adhesion of the Sn layer to the substrate, which helps the mechanical integrity of the films during stress evolution experiments. For the thickness of Cu (35 nm) in this configuration, the Cu layer is expected to be consumed by the IMC formation. As the Sn layer was much thicker than the Cu layer (i.e. 500 nm vs. 35 nm), the effect of IMC in the electrochemical experiments and stress measurements are assumed to be negligible in this study.

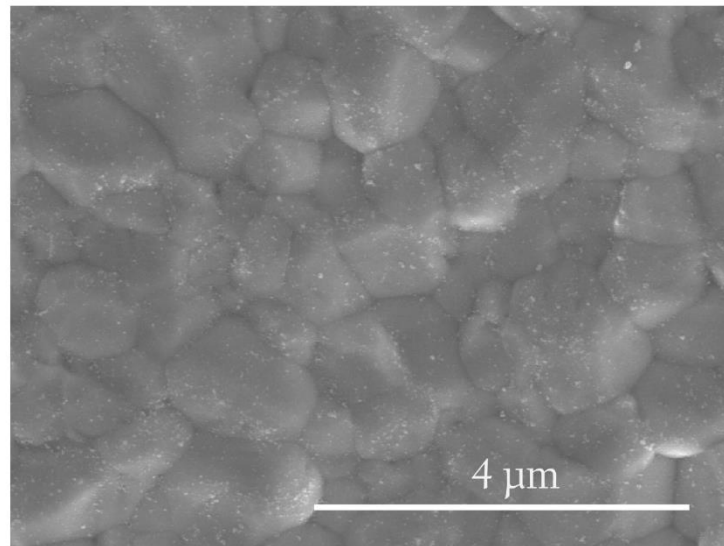


**Figure 6.1.** SEM image of as prepared 500 nm thick Sn film sample showing the grain size distribution between 500 nm and 1.5  $\mu\text{m}$ .

### 6.1.2 Electrochemical experiment

The Sn film sample served as the working electrode and was assembled into the customized electrochemical cell (section 2.2.1) with a Li metal foil (1.5 mm thick, 50.8 mm in diameter) served as the counter and reference electrode. A Celgard C480 membrane was the separator placed in between the Sn sample and the Li foil. The electrolyte composition was 1.2 M LiPF<sub>6</sub> in 3:7 (wt. %) ethylene carbonate/diethyl carbonate solvent. After the cell was assembled, the setup was left to stabilize for 12 hours before the electrochemical experiments were performed. Each experiment consisted of two stages: (i) transformation of Sn into specific Li-Sn phases at different SOC's by holding the electrode at a fixed potential; (ii) measurement of the biaxial modulus of that transformed layer through a series of delithiation-relithiation cycles.

During stage (i), the potential was brought down from the initial open circuit potential at 2.7 V to 0.8 V vs. Li/Li<sup>+</sup> by a galvanostatic lithiation (-12.5 μA/cm<sup>2</sup>, ~C/30). The potential was then held at 0.8 V for 20 hours to grow the solid electrolyte interphase (SEI) layer. This step was performed to quantify the charge consumed in forming the SEI layer as much as possible. Following SEI growth at 0.8 V, a galvanostatic lithiation (-6 μA/cm<sup>2</sup>, C/60) was used to bring down the potential to a selected value. For the different applied potentials, different phase transformations of Li-Sn phases were activated. The potential was then held until the current density decreased below -0.05 μA/cm<sup>2</sup> (< C/7200), when lithiation at the applied potential was considered complete (i.e., the entire film undergoes phase transformations and reaches a state of equilibrium corresponding to the applied potential). The cell was then switched to open circuit (OC) for 10 hours to let the Li concentration in the transformed layer to reach equilibrium. The experimental condition is presented in Table 6.1, while a list of experiments in this study including the

applied potentials during the potentiostatic lithiation in stage (i) and the corresponding specific capacities are presented in Table 6.2. The specific capacities of each sample was calculated from the accumulated charge below 0.8 V in stage (i).

In the stage (ii), a small delithiation ( $1.5 \mu\text{A}/\text{cm}^2$ ,  $\sim\text{C}/240$ ) was performed for 10 minutes followed by holding the cell at open circuit for 20 minutes. The cell was then re-lithiated with the same current density for 10 minutes, followed by a similar open circuit step. The cycle (delithiation-OC-relithiation-OC) was performed 10 times for each sample.

**Table 6.1.** Experimental condition of the elastic modulus measurement

Stage	Step	Description
(i)	lithiation	galvanostatic, $-12.5 \mu\text{A}/\text{cm}^2$ from OCP to 0.8 V
	SEI formation	potentiostatic, held at 0.8 V for 20 hrs
	Li-Sn phase transformations	potentiostatic, held at a constant value* until current density below $-0.05 \mu\text{A}/\text{cm}^2$
	open circuit	10 hrs
(ii)	delithiation	$1.5 \mu\text{A}/\text{cm}^2$ , 10 min
	open circuit	20 min
	relithiation	$-1.5 \mu\text{A}/\text{cm}^2$ , 10 min
	open circuit	20 min

\* The values of applied potential are listed in Table 6.2.

**Table 6.2.** List of samples in the elastic modulus measurement

#	Applied potential during potentiostatic lithiation (V vs. Li/Li <sup>+</sup> )	Specific capacity (mAh/g)	State of charge (X in Li <sub>x</sub> Sn)
1	0.65	120.3	0.5
2	0.50	254.5	1.1
3	0.40	543.9	2.4
4	0.10	769.1	3.4
5	0.05	842.2	3.7

### 6.1.3. *In situ stress measurement*

The stress measurements were performed during the electrochemical experiments using the MOSS system (section 2.1). The measured curvature  $\frac{1}{R}$  can relate to the product of the thickness-averaged stress in the film  $\langle\sigma\rangle$  and the film thickness  $h_f$  (also referred to as stress-thickness) by the Stoney equation,<sup>8</sup>

$$\langle\sigma\rangle h_f = \frac{M_s h_s^2}{6} \frac{1}{R} \quad \{6.1\}$$

where  $h_s$  is the thickness of the substrate, and  $M_s$  is the biaxial modulus of the substrate. In this study, the measured curvature is the change from that of the as-prepared Sn samples. It is seen in Eq. (6.1) that the measured curvature gives the product of the stress and the thickness,  $\langle\sigma\rangle h_f$  of the film. As the film thickness is expected to change during lithiation, it is necessary to know film thickness evolution in order to obtain the film stress  $\langle\sigma\rangle$  during the experiment. Beaulieu et al.<sup>9</sup> performed atomic force microscopy (AFM) measurements to investigate the thickness evolution of Sn films under galvanostatic lithiation and reported a reasonable agreement between the measured thickness and the predicted thickness based on the theoretical densities of the Li-Sn phases. Fig. 6.2 presents the theoretical prediction of the normalized thickness evolution of a 500 nm Sn film (solid line and square symbols).

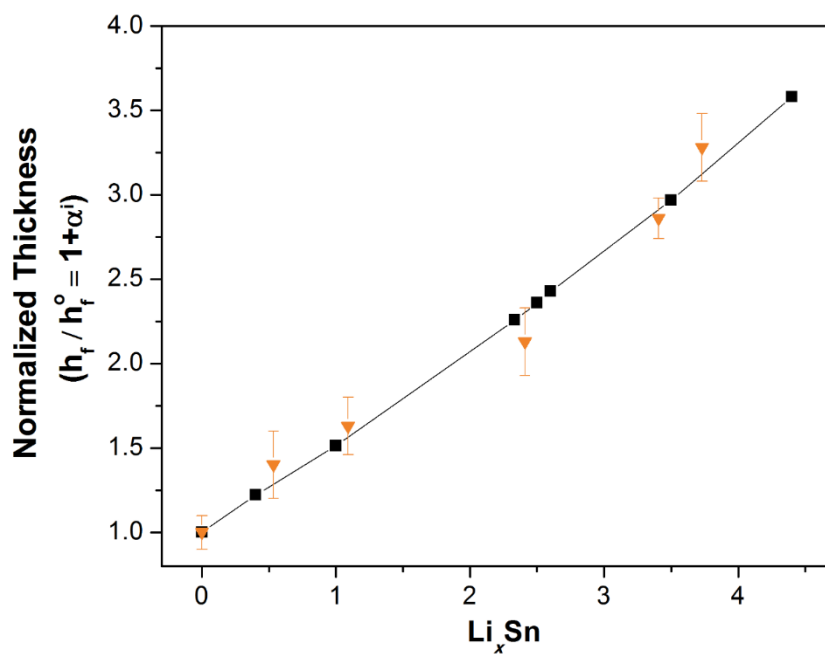


**Figure 6.2.** Thickness evolution by using the theoretical densities of Li-Sn phases. The triangular points are the observed thickness in cross-section images in Fig. 6.3. The thicknesses are normalized with respect to the original Sn thickness  $h_f^0 = 500$  nm.

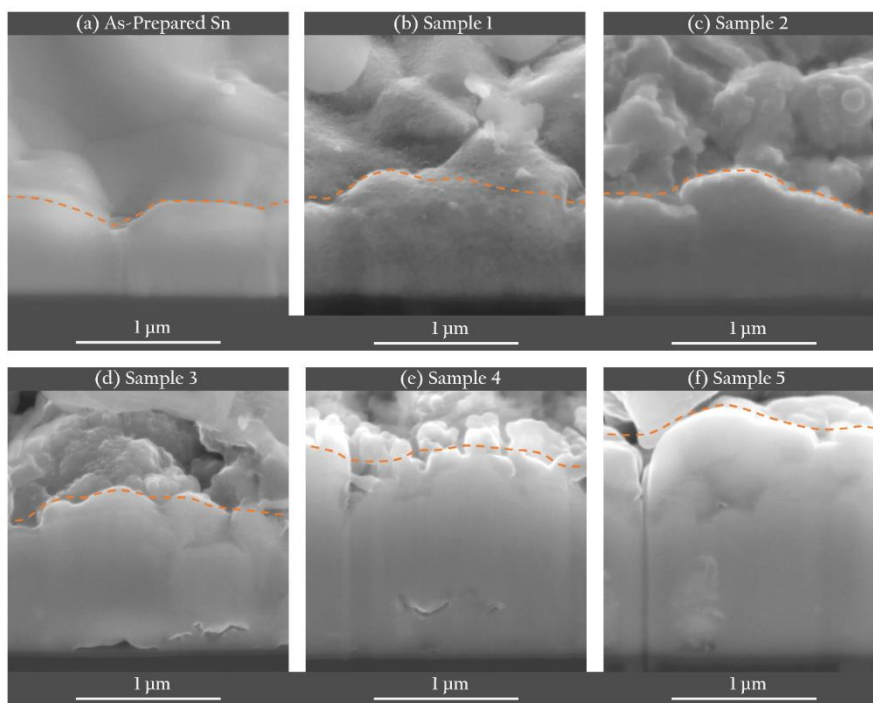


**Figure 6.3.** The cross-section images of the 500 nm Sn and lithiated Sn samples at different states of charge. The thickness values are also present in Fig. 6.2. The surface is marked by a dash line.

We have also directly measured the film thickness at different SOC<sub>s</sub> through scanning electron microscopy (SEM) of sample cross-sections prepared by focused-ion beam (FIB) milling. The corresponding cross-section images are shown in Fig. 6.3 for the as-prepared sample and those corresponding to the SOC<sub>s</sub> listed in Table 1. The measured thicknesses are shown as inverted triangles with error bars along with the theoretical prediction in Fig. 6.2; good agreement is seen between the two. Hence, we use the theoretically predicted film thicknesses at different SOC<sub>s</sub> when calculating the film stress from the measured stress-thickness values in the MOSS experiments.

For a pure phase  $i$ , where the SOC is at the stoichiometry, the theoretical film thickness  $h_f$  is

$$h_f = h_f^0(1 + \alpha^i) = h_f^i \quad \{6.2\}$$

where  $h_f^0$  is the original thickness of the Sn layer; the term in the parenthesis  $(1 + \alpha^i)$  represents the volume expansion of the film, in which  $\alpha^i$  is the volumetric strain with respect to original Sn phase.

For an SOC that is between two phases  $i$  and  $j$ , both phases are present in the film thickness. The theoretical thickness  $h_f$  of such a dual-phase film is given by

$$h_f = h_f^i(1 + \alpha^{i \rightarrow j} Z^{i \rightarrow j}) \quad \{6.3\}$$

where  $h_f^i$  is the theoretical thickness of the phase  $i$ ;  $\alpha^{i \rightarrow j}$  is the volumetric strain from phase  $i$  to phase  $j$  and  $Z^{i \rightarrow j}$  is the corresponding normalized change in SOC between the

two phases. For  $Z^{i \rightarrow j} = 0$ , it represents phase  $i$ , and  $Z^{i \rightarrow j} = 1$  corresponds to phase  $j$ . Eq. (6.2) is an interpolation (solid line) for film thickness between the values corresponding to the pure phases (square symbols) in Fig. 6.2. The values of theoretical capacities, densities, and volumetric strains  $\alpha^i$  and  $\alpha^{i \rightarrow j}$  are presented in Table 6.3.

**Table 6.3.** Material parameters of Li-Sn phases

Phase	Theoretical Specific Capacity (mAh/g)	Density (g/cm <sup>3</sup> ) [ $\cdot 10^3$ ]	Volumetric strain with respect to Sn $\alpha^i$ (%)	Volumetric strain between phase $i$ and the next phase $j$ $\alpha^{i \rightarrow j}$ (%)
Sn	-	7.29	-	22.1
Li <sub>2</sub> Sn <sub>5</sub>	90.3	6.11	22.1	23.9
LiSn	225.8	5.10	51.3	49.2
Li <sub>7</sub> Sn <sub>3</sub>	526.8	3.67	125.7	4.5
Li <sub>5</sub> Sn <sub>2</sub>	564.4	3.54	136.0	2.8
Li <sub>13</sub> Sn <sub>5</sub>	586.8	3.46	142.7	22.2
Li <sub>7</sub> Sn <sub>2</sub>	790.2	2.96	196.7	20.7
Li <sub>22</sub> Sn <sub>5</sub>	993.4	2.56	258.0	-

#### 6.1.4 Biaxial modulus calculation

Note that the strain induced by each Li-Sn phase transformation (Table 6.3) is much larger than the elastic strain limit of the corresponding phase<sup>11</sup>, which implies that the film is in a state of plastic yield at the end of stage (i) in each experiment. Therefore, during the small delithiation-relithiation excursion in stage (ii) of the experiment, the film undergoes an elastic unloading-reloading cycle. The ratio of the corresponding changes in biaxial stress  $\Delta\sigma$  and elastic strain  $\Delta\varepsilon^e$  gives the biaxial modulus  $M_f$  of the film at that SOC, which can be represented as

$$M_f = \frac{E_f}{1 - \nu_f} = \frac{\Delta\sigma}{\Delta\varepsilon^e} \quad \{6.4\}$$

where  $E_f$  and  $\nu_f$  are the Young's modulus and the Poisson's ratio of the film, respectively.

Here, we consider the film as an isotropic continuum bonded rigidly to the substrate, so the total in-plane strain of the film  $\Delta\varepsilon$  is constrained by the substrate. During the small delithiation, the total in-plane strain of the film  $\Delta\varepsilon$  can be represented as

$$\Delta\varepsilon = \Delta\varepsilon^e + \Delta\varepsilon^c = 0 \quad \{6.5\}$$

where  $\Delta\varepsilon^c$  is the change of compositional strain during the small delithiation-relithiation cycle, in which it is assumed that Li concentration is slightly altered without phase transformations. In the absence of independently measured information on the volume expansion ratio of Li-Sn phases due to changes in dissolved Li concentration, we assume it to be approximated by the slope of solid line in Fig. 6.2 at any SOC. Thus, the compositional strain is given by

$$\Delta\varepsilon^c = \left[ \frac{\Delta h_f}{h_f} \right]^{\frac{1}{3}} - 1 \quad \{6.6\}$$

where  $\Delta h_f$  is the change in film thickness due to the change of Li concentration. As noted above,  $\Delta h_f$  is obtained from the measured change of Li concentration during the delithiation-relithiation excursion and the slope of the solid line in Fig. 6.2.

By combining Eq. (6.4) and (6.5), the biaxial modulus of the film can be represented as

$$M_f = -\frac{\Delta\sigma}{\Delta\varepsilon^c} \quad \{6.7\}$$

in which  $\Delta\sigma$  is acquired from the MOSS measurement as shown in Eq. (6.1), and the procedure described in section 6.1.3. The compositional strain  $\Delta\varepsilon^c$  is calculated with Eq. (6.6). A similar approach has also been performed to measure the evolution of elastic modulus of Si thin film anode.<sup>12</sup>

### 6.1.5 X-ray diffraction of Li-Sn phases

After electrochemical and stress measurements,  $\theta$ - $2\theta$  X-ray diffraction (XRD) was used to identify the Li-Sn phases in the samples. To eliminate the degradation of the samples during the measurements, the samples were assembled into customized coin cells, which has a Kapton window for the XRD measurement. The customized coin cell consists of a stainless steel top case with a window (0.8 mm in diameter) sealed with Kapton film (0.0254 mm thick), a rubber gasket (1 mm thick), and three stainless steel parts including a spacer, a spring and a bottom case. Fig. 6.4a shows the XRD result of the as-prepared Sn sample assembled in the casing, in which additional peaks induced by the Kapton window (broad peaks at  $2\theta = 22^\circ$  and  $27^\circ$ ) and stainless steel casing (labeled with star signs) are observed. The influence of the casing on the XRD results is discussed in section 2.3.

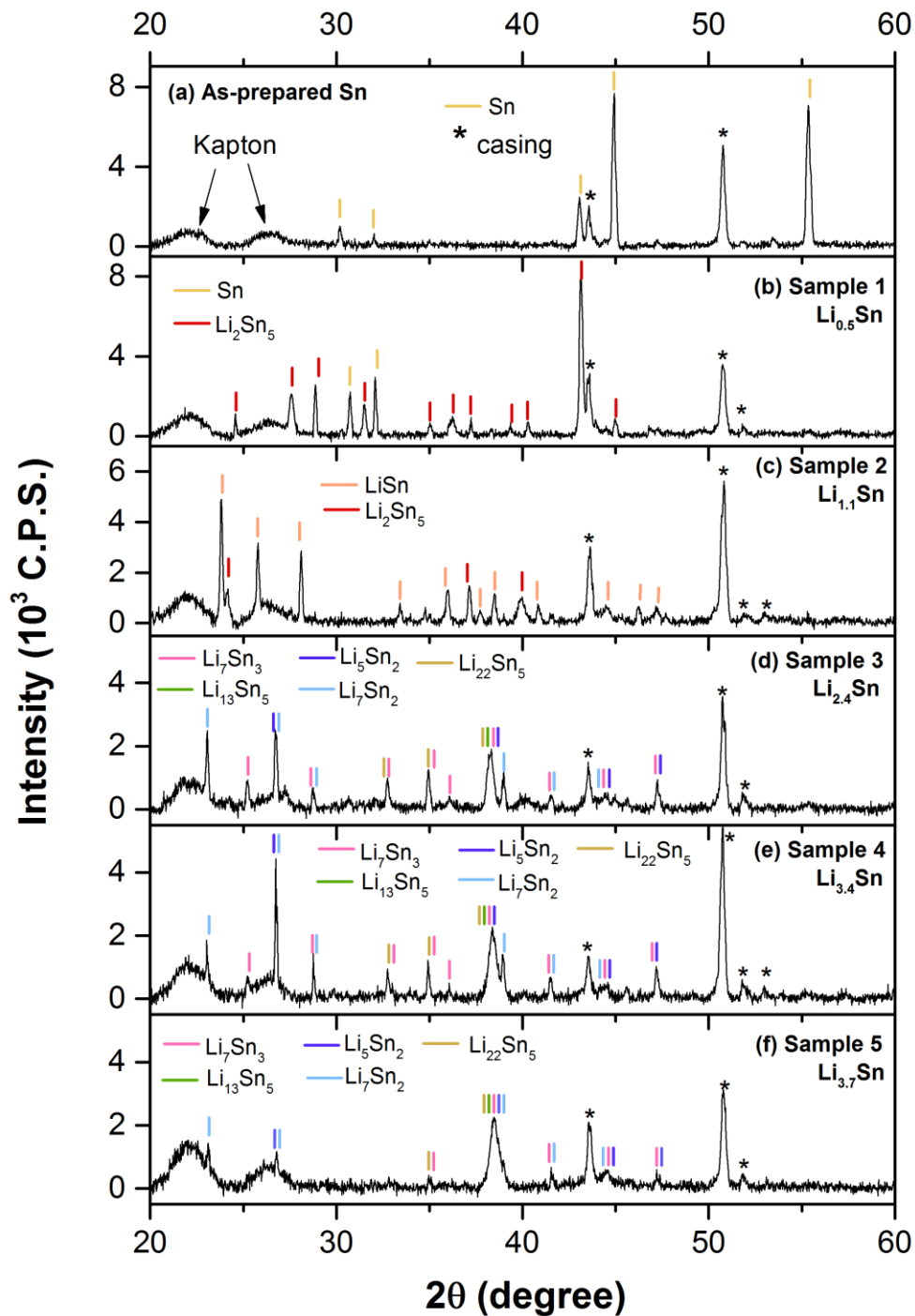


**Figure 6.4.** XRD results of Sn and lithiated Sn samples in Table 6.2: (a) As-prepared 500 nm Sn, (b) Sample 1 ( $\text{Li}_{0.5}\text{Sn}$ ), (c) Sample 2 ( $\text{Li}_{1.1}\text{Sn}$ ), (d) Sample 3 ( $\text{Li}_{2.4}\text{Sn}$ ), (e) Sample 4 ( $\text{Li}_{3.4}\text{Sn}$ ), (f) Sample 5 ( $\text{Li}_{3.7}\text{Sn}$ ). The influences of Kapton and stainless steel casing are also observed.

## 6.2 Results and Discussion

### 6.2.1. X-ray diffraction of Li-Sn phases

Fig. 6.4 shows the XRD results of the lithiated Sn samples at different SOC levels corresponding to the list in Table 6.2. Figs. 6.4b-c show samples at low SOC levels (lithiated at 0.65 V [sample 1] or 0.5 V [sample 2]) and Figs. 6.4d-f show samples at high SOC levels (lithiated at 0.4 V [sample 3], 0.1 V [sample 4], or 0.05 V [sample 5]). The corresponding phase of each peak is labeled by a vertical colored bar.

The results show that the sample 1 and sample 2 were mostly transformed into the  $\text{Li}_2\text{Sn}_5$  phase and the LiSn phase, respectively. The Sn phase is represented by a yellow bar; the  $\text{Li}_2\text{Sn}_5$  phase is identified by a red bar, and the LiSn phase by an orange bar. Note that the samples were sealed in the customized coin cells so the peaks induced by the Kapton window and stainless steel casing are also indicated in the figure.

For samples at high SOC levels, the XRD results are shown in Figs. 6.4d-f. The peaks are also labeled with colored bars: pink bars represent the  $\text{Li}_7\text{Sn}_3$  phase, green bars represent the  $\text{Li}_{13}\text{Sn}_5$  phase, deep-blue bars identify the  $\text{Li}_5\text{Sn}_2$  phase, light-blue bars identify the  $\text{Li}_7\text{Sn}_2$  phase, and deep-yellow bars represent the  $\text{Li}_{22}\text{Sn}_5$  phase. Note that the formation potentials of the Li-Sn phases at high SOC levels (i.e.,  $\text{Li}_7\text{Sn}_3$ ,  $\text{Li}_{13}\text{Sn}_5$ ,  $\text{Li}_5\text{Sn}_2$ ,  $\text{Li}_7\text{Sn}_2$  and  $\text{Li}_{22}\text{Sn}_5$ ) are closely spaced<sup>10</sup>; hence, it is difficult to control the formation of individual phases. Additionally, according to the references from the Joint Committee on Powder Diffraction Standards (JCPDS), the peaks from these high SOC level phases are very similar. Therefore, in the XRD results of high SOC level samples (Figs. 6.4d to 6.4f), most of the peaks are labeled with more than one phase (e.g., the broad peak approximately at  $38^\circ$ ). Nevertheless, several peaks can be identified with specific phases; the peaks at  $23^\circ$  and  $39^\circ$

show the existence of the  $\text{Li}_7\text{Sn}_2$  phase; the peaks at  $25^\circ$  and  $37^\circ$  identify the  $\text{Li}_7\text{Sn}_3$  phase. These findings suggest that multiple Li-Sn phases are presented in the samples at high SOC in this study. Nevertheless, from the evolution of the XRD results (Figs. 6.4d-e), it is suggested that the amount of  $\text{Li}_7\text{Sn}_2$  phase in the Sn electrodes increases as the Li concentration increases from  $\text{Li}_{2.4}\text{Sn}$  to  $\text{Li}_{3.4}\text{Sn}$ . As the Li concentration increases to  $\text{Li}_{3.7}\text{Sn}$  (Fig. 6.4f), the Sn electrodes become less crystalline as the peak at  $38^\circ$  becomes broader and the intensity of peaks at other degrees becomes smaller.

Rhode et al.<sup>13</sup> and Courtney et al.<sup>14</sup> conducted *in situ* XRD measurements during galvanostatic cycling on Sn electrodes and Sn-oxide electrodes, respectively. They reported similar XRD results as the one shown in Fig. 6.4f, where the peak at  $38^\circ$  is predominant when the potential is held below 0.4 V vs.  $\text{Li}/\text{Li}^+$  during the galvanostatic lithiation<sup>13, 14</sup>. However, the other peaks observed with samples at high SOC in this study have not been clearly identified in the relevant literature<sup>13, 14</sup>. The difference of the experimental conditions may account for the difference in the XRD results. Compared with potentiostatic lithiation, the phase transformations during galvanostatic lithiation are more dynamic; hence, long-range structures of these Li-Sn phases may be harder to form by galvanostatic lithiation. As seen in the XRD results, the samples at high SOC contain a mixture of Li-Sn phases in contrast to those at low SOC. As a result, the values of elastic modulus for high SOC samples reported here are the average of the mixture of Li-Sn phases present in the corresponding samples.

### 6.2.2 Stress during phase transformations

To demonstrate the sequences of experimental processing used for each sample, data from sample 2 (potentiostatic lithiated at 0.5 V) in stage (i) of the electrochemical experiment is present in Fig. 6.5, in which the potential, current density, capacity, stress-thickness, and stress measurement.

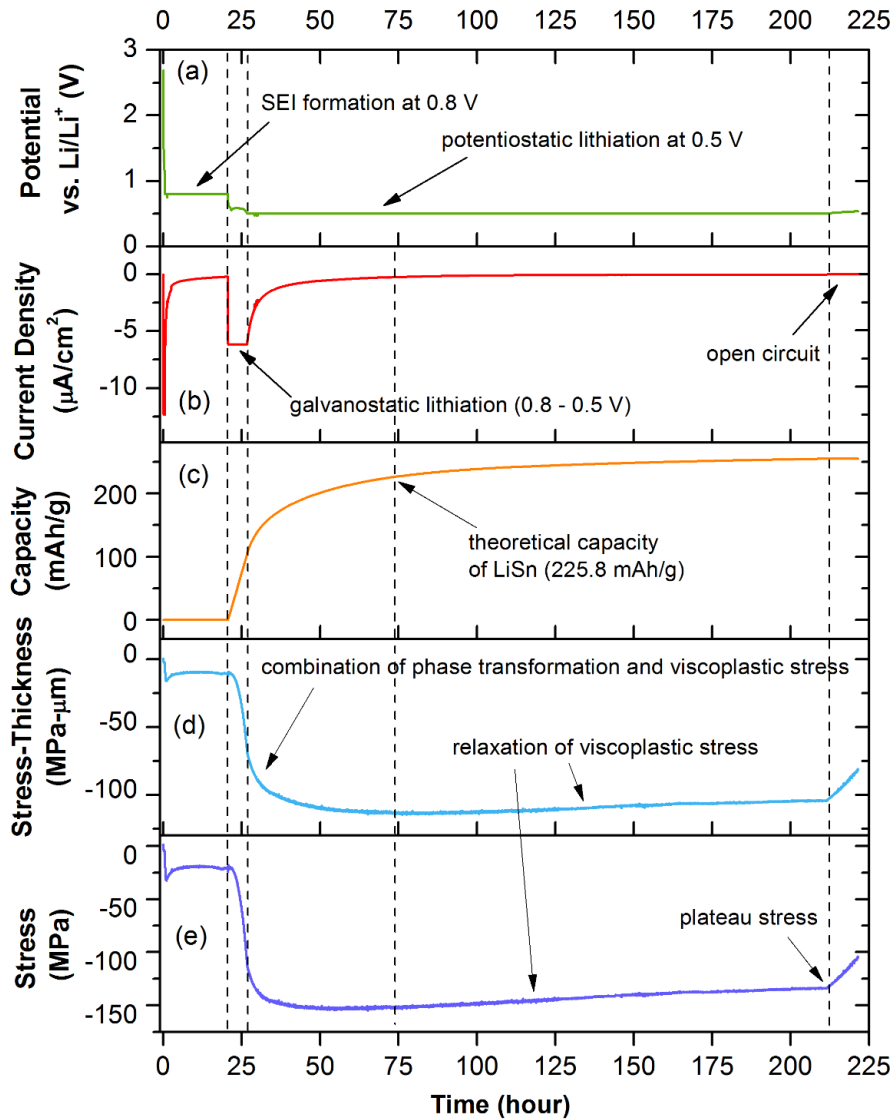


**Figure 6.5.** Experimental data of sample 2 lithiated at 0.5 V during stage (i) of the experiment: phase transformations of Li-Sn phases: (a) potential, (b) current density, (c) capacity, (d) stress-thickness, (e) thickness-averaged stress.

As described above, the sample first underwent a SEI formation at 0.8 V for 20 hours and then the potential was brought down from 0.8 V to 0.5 V by a galvanostatic lithiation. During the subsequent potentiostatic lithiation at 0.5 V, although the capacity continues to increase throughout the potential hold, most of the film appears to transform by time  $t = 75$  hours. The capacity at this time reaches the theoretical capacity of LiSn phase (225.8 mAh/g) as shown in Fig. 6.5c. Further slow increase of capacity beyond this time is possibly due to dissolving limited amount of Li into the transformed layer, or ongoing side reactions in the electrolyte. Fig. 6.5d shows the corresponding evolution the stress-thickness  $\langle\sigma\rangle h_f$ . Note that the stress in the film can depend on the rate of lithiation (which determines the strain rate) due to viscoplastic response of the material (as discussed in Ref. <sup>15</sup>). Hence, its time dependence can be quite complex because of the evolving current density shown in Fig. 6.6b. The evolution of stress-thickness is due to a combination of phase boundary progression and the evolving stress in the film. The stress-thickness reaches a plateau at around  $t = 75$  hours, and shows slight relaxation in the remaining duration of experiment, which may due to viscoplastic stress relaxation. Fig. 6.6e shows the thickness-averaged stress in the film, in which the uniform stress of the transformed layer is represented beyond  $t = 75$  hours. At the end of the potential hold at 0.5 V (approximate  $t = 210$  hours), the thickness-averaged stress value becomes fairly constant, which represents the low strain-rate flow stress of the lithiated film (referred to as plateau stress). Details of plateau stress are provided in the later discussion below.

Following the potentiostatic lithiation, the cell was switched to OC for 10 hours (approximately  $t = 210 - 220$  hours) during which some stress relaxation was observed. Part of the relaxation can be attributed to the change of the double layer capacitance when switched to OC. The rest of it can be attributed to residual side reactions that may

continue to occur at the electrode surface due to impurities in the electrolyte. Both of the processes results in removal of a small amount of Li from the electrode, resulting in the observed stress relaxation. Here, we consider that 10 hours of OC is adequate for the Li concentration in the electrode to reach equilibrium, after which the delithiation-relithiation can be carry out for the elastic modulus measurement.

### 6.2.3 Biaxial modulus measurement

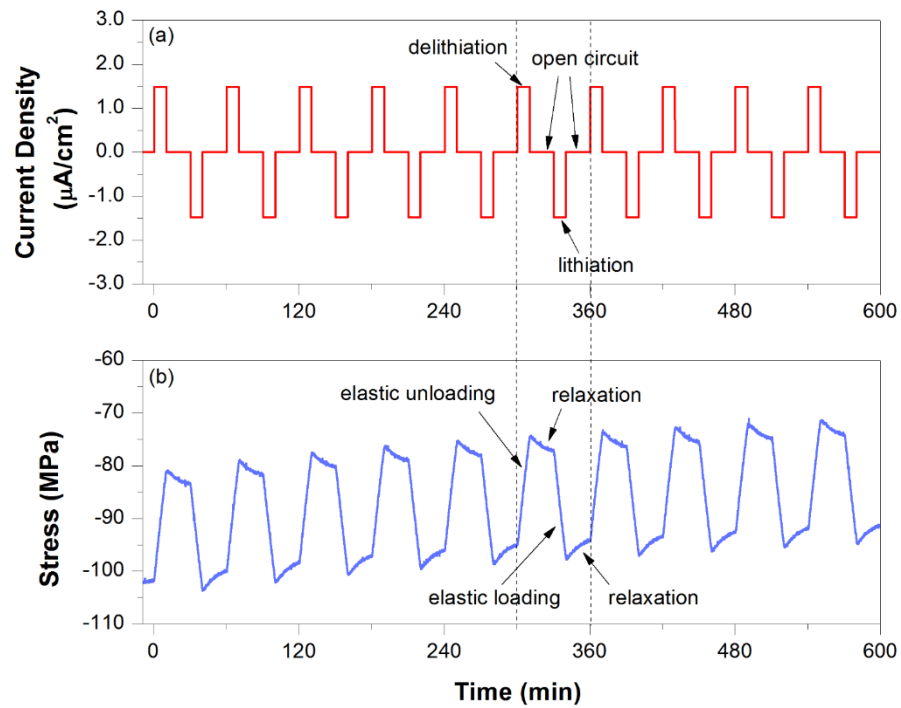


**Figure 6.6.** Experimental data of sample 2 during the stage (ii) of experiment: small scale delithiation/lithiation. (a) current density, (b) stress measurement showing the elastic response of the lithiated sample.

Fig. 6.6 shows the history of current density and film stress for the elastic modulus measurements through the 10 repeated delithiation-relithiation cycles of sample 2. The film was held at OC for 20 mins between delithiation and relithiation in each cycle, to

allow for stress relaxation due to any rate-dependent effects. Note that the change in Li concentration during the delithiation steps is so small that the modulus measurement can be considered to be made at essentially the same SOC. Since the film is at a state of yield, the decrease in the volume during the delithiation steps result in elastic unloading of the film, along with the associated decrease in the film stress as seen in Fig. 6.6b. As described above, the change in in-plane strain can be calculated from the change in Li concentration of the film (Eqs. 6.5 and 6.6). Thus, the ratio of the change in stress to the change in in-plane strain gives the biaxial modulus of the film as demonstrated in Eq. (6.7). The procedure is repeated for samples at different SOCs; the measured biaxial modulus as a function of Li concentration is presented in Fig. 6.7. The results show that the biaxial modulus decreases dramatically from 60 GPa to 20 GPa as the Sn film is transformed into the lithiated phases at higher SOCs.

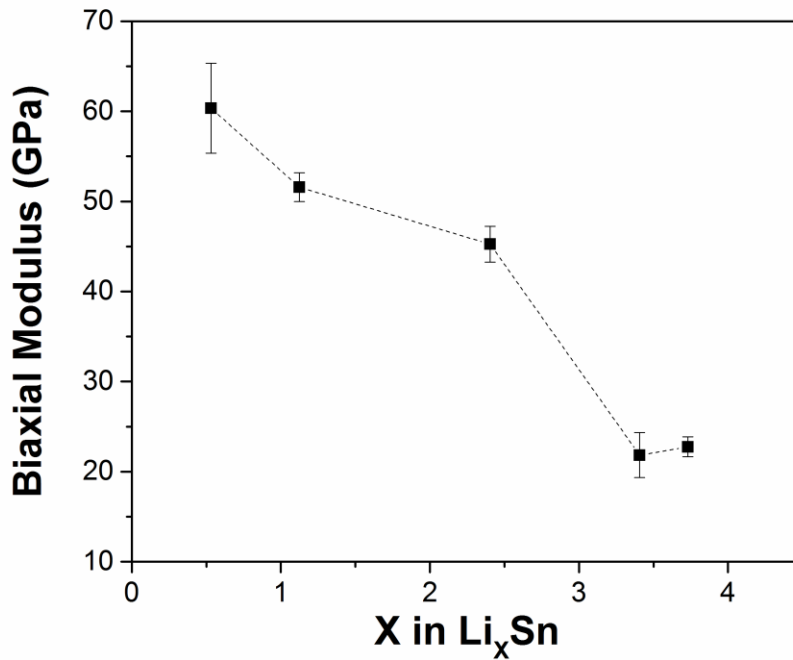


**Figure 6.7.** The biaxial modulus of lithiated Sn samples at different states of charge.

To compare with the reported computational bulk modulus<sup>3-5</sup>, the values of Poisson's ratio of Li-Sn phases reported by Stournara et al.<sup>5</sup> are used in the calculations of bulk modulus. Fig. 6.8 shows the bulk modulus obtained in this work along with the computational values reported in the literature. A similar trend of decreasing bulk modulus is found. Note that the lithiated samples at high SOC's consist of multiple phases; thus, the measured bulk modulus is the average of the Li-Sn phases in the samples.

The results from this study show that the bulk modulus decreases from 40 GPa to 10 GPa as the Li concentration in the Sn anodes increases from  $\text{Li}_{0.5}\text{Sn}$  to  $\text{Li}_{3.7}\text{Sn}$ . The computational results of Stournara et al.<sup>5</sup> are seen to be in very good agreement with our experimental results. Although the computational results of Li et al.<sup>3</sup> and Moon et al.<sup>4</sup> show consistently higher values, the decrease in the modulus predicted by them is in good qualitative and quantitative agreement with the experimental results.

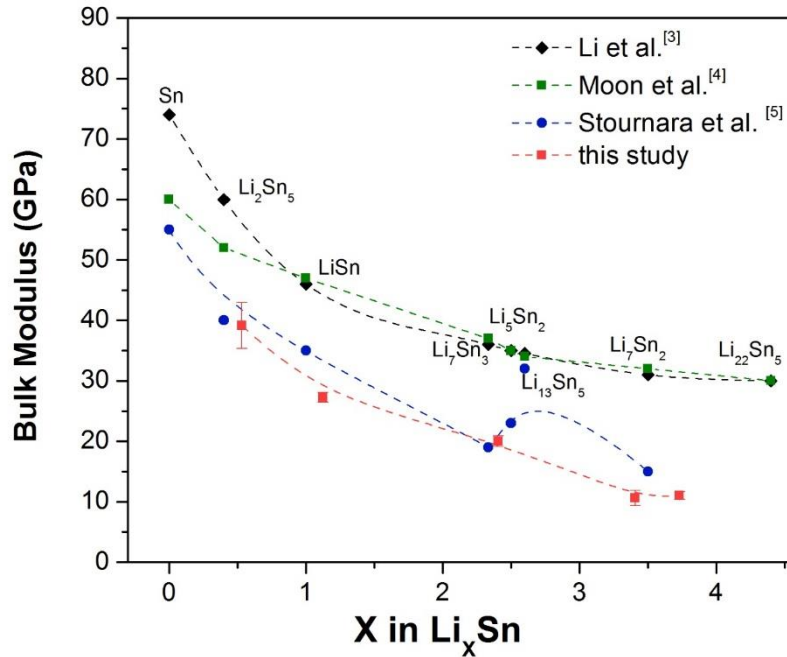


**Figure 6.8.** The comparison of the bulk moduli obtained in this work and the values reported in the literature using DFT calculations.

#### 6.2.4 Yield stress of Sn film anodes

In addition, the stress values at the end of the potentiostatic lithiation (i.e., the plateau stress in Fig. 6.5e) obtained from samples at different SOC<sub>s</sub> are presented in Fig. 6.9.

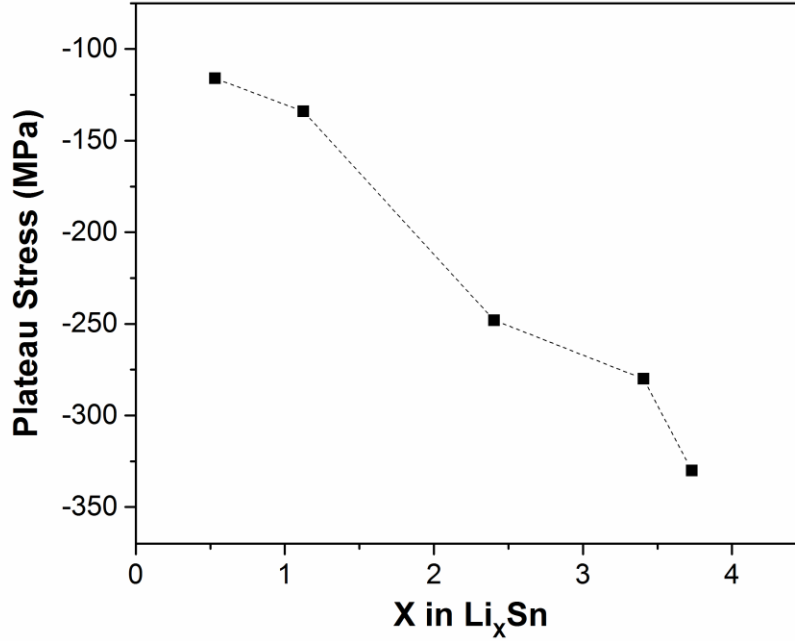


**Figure 6.9.** The stress in the lithiated samples at different states of charge obtained at the end of state (i) of electrochemical experiment.

Since the film is at the state of yield and the current density is close to zero for a long period of time, the plateau stress is the low strain-rate flow stress and can be approximated as the rate-independent yield stress of the film at that SOC. Note that the compressive yield stress increases steadily from  $\sim 120$  MPa to  $\sim 330$  MPa as the Li concentration increases. For comparison, the yield stress of pure Sn in thin film form is  $\sim 10$ - $20$  MPa.<sup>11, 16</sup> It is worth noting that the yield stress of  $\sim 120$  MPa measured for  $\text{Li}_2\text{Sn}_5$  phase in this investigation is much higher than ( $\sim 29$  MPa) reported in previous chapters. In the previous study, the thickness of Sn film was  $\sim 2$   $\mu\text{m}$ , whereas the thickness

of the film in the current study is  $\sim 500$  nm. The yield stress of metal thin films has been known to depend on film thickness and grain size<sup>8</sup>. For many metals, it has been shown that the yield stress increases rapidly once the film thickness range is lower than  $\sim 1 \mu\text{m}$ <sup>8</sup>. Hence, the difference in the film thickness and grain size may account for the difference in the reported yield stress of  $\text{Li}_2\text{Sn}_5$  between the present investigation and the current study. It is interesting to note that the yield stress of Sn anode increases as it transforms into higher Li concentration phases, whereas the elastic modulus decreases. This observation calls for detailed investigations of mechanisms of inelasticity in Li-Sn phases.

### 6.3 Conclusions

In this chapter, we measured the biaxial modulus of Sn thin film anodes at different SOC. A significant softening of biaxial modulus is observed as Sn transforms into higher Li concentration phases. The biaxial modulus decreases from  $\sim 60$  GPa to  $\sim 20$  GPa as Li concentration in Sn anodes increases from  $\text{Li}_{0.5}\text{Sn}$  to  $\text{Li}_{3.7}\text{Sn}$ . The compressive yield stress of lithiated Sn films increase from  $\sim 120$  MPa to  $\sim 330$  MPa for the same change in SOC. These measurements provide useful reference for future computational predictions. Further investigation of mechanisms of plasticity are necessary to understand inelastic deformation in Li-Sn phases.

### References

1. K. Ui, S. Kikuchi, Y. Kadoma, N. Kumagai, and S. Ito, *Journal of Power Sources*, **189** 224–229 (2009).
2. D. H. Nam, R. H. Kim, D. W. Han, and H. Kwon, *Electrochimica Acta*, **66** 126–132 (2012).
3. K. Li, H. Xie, J. Liu, Z. Ma, Y. Zhou, and D. Xue, *Phys. Chem. Chem. Phys.*, **15** 17658 (2013).
4. J. Moon, K. Cho, and M. Cho, *International Journal of Precision Engineering and Manufacturing*, **13**

- (7), 1191-1197 (2012).
5. M. Stournara, P. R. Guduru, and V. Shenoy, *Journal of Power Sources*, **208** 165-169 (2012).
  6. Y. Qi, J. Louis G. Hector, C. James, and K. J. Kim, *Journal of The Electrochemical Society*, **161** (11), F3010-F3018 (2014).
  7. E. Chason, N. Jadhav, W. L. Chan, L. Reinbold, and K. S. Kumar, *Applied Physical Letters*, **92** 171901 (2008).
  8. L. B. Freund and S. Suresh, *Thin Film Materials: Stress, Defect Formation and Surface Evolution*, Cambridge University Press (2003).
  9. L. Y. Beaulieu, S. D. Beattie, T. D. Hatchard, and J. R. Dahn, *Journal of The Electrochemical Society*, **150** (4), A419-A424 (2003).
  10. M. Winter and J. O. Besenhard, *Electrochimica Acta*, **45** 31-50 (1999).
  11. A. Mukhopadhyay, R. Kali, S. Badjate, A. Tokranov, and B. W. Sheldon, *Scripta Materialia*, **92** 47-50 (2014).
  12. V.A. Sethuraman, M. J. Chon, M. Shimshak, N. Van Winkle, and P. R. Guduru, *Electrochemistry Communications*, **12** 1614-1617 (2010).
  13. K. Rhodes, R. Meisner, M. Kirkham, N. Dudney, and C. Daniel, *Journal of The Electrochemical Society*, **159** (3), A294-A299 (2012).
  14. I. A. Courtney and J. R. Dahn, *J. Elect rochem. Soc.*, **144** (6), 2045-2053 (1997).
  15. C.-H. Chen, E. Chason, and P. R. Guduru, *Journal of Electrochemical Society*, **164** (11), E3661-E3670 (2017).
  16. F. Pei and E. Chason, *Journal of Electronic Materials*, **43** (1), 80 (2014).

# Chapter 7.

## Summary

---

### 7.1 Conclusions

In this thesis, we systematically studied the kinetics of phase transformations in Sn anodes and the corresponding evolution of stress and mechanical properties during electrochemical processes. The desired phase transformations were conducted at select potential and the stress evolution in the Sn thin film anodes was acquired *in situ* by monitoring the change in substrate curvature. The evolution of elastic modulus with Li concentration was also characterized from the elastic behavior of the Sn anodes. Cross-section examination and X-ray diffraction (XRD) were performed before and after experiments to identify the phase composition in the samples. The phase boundary propagation was analyzed by the kinetic modeling, which also enabled us to investigate the stress mechanism behind the experimental observations.

The main conclusions of this thesis are:

- The phase transformation of  $\text{Li}_2\text{Sn}_5$  and  $\text{LiSn}$  phases can be controlled by the applied potential in the potentiostatic lithiation. The cases of a single phase boundary (i.e., the  $\text{Sn}/\text{Li}_2\text{Sn}_5$  interface) and two phase boundaries (i.e., the  $\text{Sn}/\text{Li}_2\text{Sn}_5$  and  $\text{Li}_2\text{Sn}_5/\text{LiSn}$  interfaces) are investigated, respectively. In all the studied cases, the phase boundaries propagate relatively homogeneously in the Sn anodes and result in the layered structures found in the cross-sections. Therefore, the stress in the Sn,

$\text{Li}_2\text{Sn}_5$ ,  $\text{LiSn}$  phases and the surface solid electrolyte interphase can be characterized with the 1-D phase kinetic analysis.

- By applying the numerical solution of the kinetic modeling, the stress in the  $\text{Li}_2\text{Sn}_5$  and  $\text{LiSn}$  layers is found at the low strain-rate stress. Whereas, the stress in the Sn layer varies as the result of diffusion of the excess Li. At the initial stage of the phase transformation, the Li concentration evolves dramatically in the Sn layer and leads to a state of high compressive stress. This stress state can be described by the mechanism of rate-dependent plasticity (i.e., viscoplasticity). As phase boundaries propagate, the Li concentration becomes steadier and eases the high compressive stress in the Sn layer. Furthermore, the Li can diffuse in the opposite direction toward the Sn/ $\text{Li}_2\text{Sn}_5$  phase boundary and further relaxes the stress in the Sn layer. In this case, the stress state is governed by the mechanism of elastic unloading. Subsequently, the compressive stress in the Sn anode increases steadily as the lithiated phases form in the anode. The nominal yield stress of Sn is found at -16 MPa, and the low strain-rate stress of  $\text{Li}_2\text{Sn}_5$  and  $\text{LiSn}$  are around -25 MPa and -58 MPa, respectively.
- The phase boundary propagation is found can be estimated from the experimental data. For the case with a single Sn/ $\text{Li}_2\text{Sn}_5$  interface the position of the interface can be approximated from the measured coulombic charge. In addition, the phase propagation can be described by the steady-state linear kinetic model. For the case consisting of the Sn/ $\text{Li}_2\text{Sn}_5$  and  $\text{Li}_2\text{Sn}_5$ / $\text{LiSn}$  interfaces, the phase propagation can be obtained from solving the balance equations of the measured coulombic charge and measured stress-thickness.
- The kinetic analysis indicates that the Li diffusivity in Sn,  $\text{Li}_2\text{Sn}_5$  and  $\text{LiSn}$  phases

are on the order of  $10^{-12}$  cm<sup>2</sup>/s. The reaction rate coefficient of Sn-Li<sub>2</sub>Sn<sub>5</sub> phase transformation  $K_{\alpha\beta}$  is approximately on the order of  $10^{-6}$  cm<sup>4</sup>/mol s, and for Li<sub>2</sub>Sn<sub>5</sub>-LiSn phase transformation  $K_{\beta\gamma}$ , it is approximately on the order of  $10^{-5}$  to  $10^{-6}$  cm<sup>4</sup>/mol s.

- By characterization of the elastic behavior of thin film Sn anode samples, the trend of significant decrease in the elastic modulus is found as Li concentration increases. The result supports the reported predictions of elastic modulus by the density function theory calculation.<sup>1-3</sup>
- The findings in this thesis provide useful information for future research on reliability, mechanical failure, and cell design of Sn and Sn-based electrodes. Furthermore, this system serves as a canonical setup to understand the diffusion with moving phase boundary and mechanical property measurement of thin films.

## 7.2 Future Works

In the course of this thesis, various areas have been identified where further research is needed. Firstly, a comprehensive understanding of the phase kinetics during the delithiation processes is desired. Conducting potentiostatic delithiation or small current density galvanostatic delithiation can provide the ideal experimental condition for modeling analysis of the kinetic mechanism during delithiation. This investigation can lead to further investigation of the stress evolution during delithiation processes and can be applied to optimize the performance of Sn anodes.

Secondly, an extension of the moving boundary modeling to a 2-D configuration will be helpful to account for the variation in material properties caused by polycrystalline materials. Furthermore, the 2-D modeling enables the analysis of various designs of the

electrode.

Thirdly, a fundamental investigation on the kinetic and mechanical properties of Sn-based anodes is preferred. Many researchers have worked on materials such as Sn-oxide materials, and found that Sn is the predominant in the reaction with Li.<sup>4-8</sup> The other elements in the Sn-based anodes react with Li in the very first cycle and the product remains relatively inert in the following cycles, and the product can be uniformly formed in the anodes. The product formed in the first cycle provides spacing to accommodate the large volumetric strain induced by Li-Sn reactions. Thus, the Sn-based anodes tend to have better cyclability and reliability than pure Sn anodes. However, only few literature reports have been focused on the analysis of structural change and material properties, which is required to improve the performance of these materials. The findings of Sn anodes in this thesis provide fundamental analysis of Li-Sn system and may be useful for investigation of the Sn-based anode materials.

## References

1. M. Stournara, P. R. Guduru, and V. Shenoy, *Journal of Power Sources*, **208** 165-169 (2012).
2. J. Moon, K. Cho, and M. Cho, *International Journal of Precision Engineering and Manufacturing*, **13** (7), 1191-1197 (2012).
3. K. Li, H. Xie, J. Liu, Z. Ma, Y. Zhou, and D. Xue, *Phys. Chem. Chem. Phys.*, **15** 17658 (2013).
4. I. A. Courtney and J. R. Dahn, *Journal of The Electrochemical Society*, **144** (6), 2045-2053 (1997).
5. A. D. W. Todd, R. E. Mar, and J. R. Dahn, *J. Electrochem. Soc.*, **153** (10), A1998-A2005 (2006).
6. D. Larcher, L. Y. Beaulieu, D. D. MacNeil, and J. R. Dahn, *Journal of The Electrochemical Society*, **47** (5), 1658-1662 (2000).
7. J. Xie, N. Imanishi, A. Hirano, Y. Takeda, O. Yamamoto, X. B. Zhao, and G. S. Cao, *Solid State Ionics*, **181** 1611-1615 (2010).
8. R. Z. Hu, M. Q. Zeng, and M. Zhu, *Electrochimica Acta*, **54** 2843-2850 (2009).